VRIJE
UNIVERSITEIT
BRUSSEL

Graduation thesis submitted in partial fulfilment of the requirements for the degree of Master in Science: Physics and Astronomy

INVESTIGATION OF THE TIME PATTERNS OF GRB LIGHT CURVES

Else Magnus

June 2023

Promotors: Prof. Dr. Krijn de Vries & Prof. Dr. Nick van Eijndhoven
Supervisor: Rose Stanley
Sciences and Bioengineering Sciences

Abstract

English

With every new discovery comes the quest to understand it, and this was not different for gamma-ray bursts (GRBs). GRBs last extremely short, on cosmic times scales, but show a wealth of time variability in their gamma-ray emission. Properties of this variability may carry information about the process the gamma-rays emerge from. In this thesis, we investigate the gamma-ray light curves of GRBs in Fourier space. We aim to study the power-law behaviour of the average power-density spectrum (PDS) for different samples of GRBs, inspired by previous studies. It was proposed that the slope of the average PDS could be related to $-5/3$, the slope of the Kolmogorov energy spectrum, indicating that the source of the gamma-rays hosts a turbulent medium. Key to probing this slope is a robust method to characterise the power-law behaviour, to determine for example the frequency range in which we decide to fit. Consequently, we develop two procedures and apply these to the different samples of GRBs that we consider. Most of our results are consistent with the Kolmogorov turbulence. We find that the slope of the average PDS of the precursors is inconsistent with $-5/3$. This is additionally true for the noise profiles and all noise-dominated spectra. This suggests that the precursor and prompt emission are not produced by the same process, or in the same environment.

Nederlands

Bij elke nieuwe ontdekking hoort de zoektocht om deze te verklaren. Dit was niet anders voor gammaflitsen (GFn). Gammaflitsen bestaan, astronomisch gezien, slechts voor een hele korte tijdsspanne, maar ze herbergen een wereld aan tijdsvariaties in hun gammastraling. Het is mogelijk dat de eigenschappen van deze variabiliteit informatie bevatten over het proces waarin de gammastralen geproduceerd worden. In deze thesis onderzoeken we de lichtcurves van gammaflitsen in het Fourierdomein. We beogen de analyse van het machtsverband, aanwezig in het gemiddelde vermogendichtheidsspectrum (VDS), voor verschillende groepen van GFn. Het onderzoek is geïnspireerd op eerdere studies, waarin gesuggereerd werd dat de index van het gemiddelde VDS in verband kan gebracht worden met de index $-5/3$. Deze is ook wel gekend als de index van het Kolmogorovspectrum, en zou aangeven dat in de bron van de gammastraling een turbulent proces aanwezig is. We merken echter op dat aan de basis van het karakteriseren van het machtsverband een doortastende methode moet liggen, om bijvoorbeeld het frequentiegebied te bepalen waarin men wil fitten. In deze thesis ontwikkelen we twee methodes om hieraan tegemoet te komen en passen we deze toe op de verschillende groepen van GFn. We vinden voornamelijk resultaten die consistent zijn met de Kolmogorovturbulentie, en kunnen concluderen dat de index van de voorloper-emissie niet consistent is met $-5/3$, net zoals de indices van de ruisprofielen en alle ruisgedomineerde spectra. Dit betekent dat de voorloper en hoofdfase van de gammaflits niet geproduceerd worden in hetzelfde proces of in dezelfde omgeving.

Acknowledgements

Those hundred pages mark the end of the previous five years. Five years of blood, sweat and tears, but also five years of joy, happiness and astonishment. It is a crazy time to be alive, and what a wonderful time did I have.

I want to thank everyone on the road. My friends of all these years, that came, left or stayed, following their own world line. My friends at the side-line, which supported me and believed in me. You all made me more "me", and I am thankful for that. Thankful for the coffees, the ice creams, the noodles and the talks. I want to thank my family, for not understanding what I was doing, but trying to. I want to thank Max, for being my python hero, for listening to my worries and for motivating me, always.

I want to thank Krijn, Nick and Rose, for making me a better scientist during the latest months. For motivating and encouraging me, for making time and always being enthusiast. I want to thank everyone else that gave me advice, supported me, was there when I needed a helping hand with the cluster, with the data or the presentations. Thanks to you all. Because of you, this thesis is what it has become, and I am proud of it.

Contents

Acronyms

ACD Anti-Coincidence Detector

AGN Active Galactic Nucleus

BAT Burst Alert Telescope

BATSE Burst And Transient Source Experiment

BB Bayesian Block

BH Black Hole

CGRO Compton Gamma-Ray Observatory

DFT Discrete Fourier Transform

EM Electromagnetic

GBM Gamma-Ray Burst Monitor

GRB Gamma-Ray Burst

Integral International Gamma-Ray Astrophysics Laboratory

IR Infrared

LAT Large Area Telescope

LIGO Laser Interferometer Gravitational-Wave Observatory

NS Neutron star

PDS Power-Density Spectrum

SN Supernova

SNR Signal-To-Noise Ratio

TTE Time Tagged Event

UHECR Ultra-High-Energetic Cosmic Rays

WR Wolf-Rayet

Chapter 1

General Introduction

When gamma-ray bursts (GRBs) were discovered at the end of the 1960s, it did not shake the world like the man on the Moon did, or the death of Martin Luther King. Their observation was not even noticed immediately, since it took more than five years until the presence of this new, transient, unknown, and unpredictable phenomenon was established. Nevertheless, the field exploded afterwards. From having an unknown origin, and possibly originating from everywhere all at once, now the knowledge they conceal about strong magnetic fields, strong gravity circumstances, the death of stars, nuclear enrichment of the Universe, particle acceleration, cosmology, and other topics connects to and can teach us something about all fields in (astro)physics.

Gamma-ray bursts introduce themselves. They are very short and sudden releases of gamma-rays, which belong to the most energetic part of the electromagnetic (EM) spectrum. For years, they appeared as short as milliseconds or several minutes, and were only visible in the keV to MeV energy range. They occur unpredictably, and do not repeat themselves in the same location. The fast-fading bursts are difficult to capture and locate. It was only in 1997, almost exactly thirty years after the first observation of a GRB, when the first afterglow was discovered; a slowly-fading lower-energy emission component that followed the main burst. Since then, GRBs can be observed for hours, days, months up to years in the radio, millimetre, infrared, optical, ultraviolet, X-ray and gamma-ray wavelengths. They are not only luminous in the EM spectrum, but are also expected to be strong emitters of high-energy neutrinos, high-energy cosmic rays and gravitational waves. With the coincident observation of GW 170817 and GRB 170817A six years ago, the occurrence of gravitational waves together with a GRB was confirmed. This was a major discovery for both fields and was the start of the multi-messenger era, bringing hope for the coming years.

Today, it is believed that there are two large groups of GRBs, with different progenitors and different characteristics. On the one hand, there are the short GRBs, having an average duration of approximately one second and which are, or at least some of them, formed by the merger of two compact objects. On the other hand, there is a group consisting of longer bursts ($\Delta t \sim 30$ seconds), which are mostly found in star-forming

regions and galaxies. They are related to the death of massive stars, especially to a certain class of dying stars, the supernovae (SNe) type Ic. The broad picture, supported by the majority of the astrophysicists, is formulated as follows: both groups are believed to form a compact object with an accretion disc and emit radiation mainly by the formation of relativistic jets. These are long beams of out-flowing matter that extend over light years and travel with a velocity near the speed of light. In these structures, particles are accelerated and reach high energies, which they release in the form of radiation and other messengers. However, the theoretical models of the physical processes in the jets and the accretion disc are still filled with question marks. How are the particles accelerated? Is the central object a black hole, or rather a neutron star or quark star? Is the radiation due to synchrotron processes, or Compton processes? How is the high-energy emission generated?

In this thesis, we hope to answer at least a very small part of these questions. GRBs exhibit very variable gamma-ray light curves. Three main emission periods can be distinguished: the prompt emission (the main burst), the afterglow emission, and a short and dim flash of gamma-rays preceding the prompt emission - the precursor - which is only observed in some GRBs. In the following pages, the time variability of the GRB is investigated by considering it in frequency space, i.e. by performing a Fourier transformation on the time series. In particular, we study the power-density spectrum (PDS) of the GRBs, which is the absolute square of the amplitude spectrum of the Fourier transform. This spectrum can be interpreted as the distribution of the power over the frequency range - characteristic frequencies appear stronger and more distinct - and reveals the features of the time series we want to study. By investigating the average PDS of a sample of GRBs, we want to uncover the properties of the underlying process that produces the gamma-ray emission. In this thesis, we will focus on the slope of the average PDS. Previous research reported an explicit slope of $-5/3$, which can be related to turbulent processes occurring in the GRBs, that imprint the light curves. We want to investigate the evolution of the slope over different energy bands, and over the different phases of the light curve. We want to study whether the slope is inherent to the main burst, or can be seen in the precursor as well. We will discuss if it depends on energy, and appears in both bright and dim bursts, long and short bursts. The presence or absence of this slope in GRB spectra might tell us something about the processes from which the gamma-rays originate, and as such constrain existing and new models.

In **Chapter 2**, we sketch the history of GRBs, from their discovery in 1967 until the present days, and how they play an important role in the field of multi-messenger astronomy. We review their observational properties and how this leads to theoretical models as the fireball or electromagnetic models, or hypotheses about their progenitors. We end with a discussion of the Kolmogorov turbulence, to which the $-5/3$ slope is often related.

Next, we briefly go over the Fourier transformation in **Chapter 3**. A toy model is presented to explain the characteristics of the Fourier transform. We want to understand

how we can relate certain features in the frequency domain back to elements in the time domain. The Fermi Gamma-Ray Space Telescope, from which we use the data, is introduced in **Chapter 4**, together with the details about the different steps we took to calculate the average PDS of the different samples. We modified an existing procedure to characterise the background in our light curves, corrected the light curves on redshift and normalised them, and estimated the errors on the individual and average spectra. This chapter contains the fully reproducible method that we applied to obtain the results that are presented in **Chapter 5**. For some GRBs, the background method was not adequate. We manually modified the background fit. Those GRBs are listed in **Appendix A**.

In **Chapter 5**, we try to understand what happens for different samples of GRBs. We search a way to only select qualitative light curves which are not noise dominated. We compare observer frame (see **Appendix B**) against source frame, and distinguish different samples based on peak rate, photon energy and duration. We also have the opportunity to separate the different emission periods and study the average PDS of the precursor and prompt emission individually, which has never been done before. At last, we study the noise profile of the light curves. We discuss the different results in depth and provide the reader with a conclusion in **Chapter 6**. We shortly summarise what we would like to investigate further in the future, but lies beyond the scope of this thesis.

Contributions of the author. This paragraph lists the most important contributions that I have made individually to this project. For more information, I refer the reader to the text.

- In Chapter 3, I included a toy model to investigate the features of the Fourier transform.

- In Chapter 4, I modified the background characterisation method that was developed by Coppin et al. (2020), since their method did not work for the data used in this thesis. We processed the data from raw single photon counts to workable light curves, by redshift correcting, subtracting the background level and normalising. We computed the average PDS and included the error calculation.

- In Chapter 5, we developed the χ^2-method, that we have applied in this thesis for the first time. I constructed the different GRB samples, based on the different parameters, myself.

Chapter 2

Gamma-Ray Bursts

In this chapter, an overview of the state-of-the-art in the field of gamma-ray bursts is given. Their discovery and observational history in Section 2.1 gives the onset for the discussion of the characteristics and properties of GRBs in Section 2.2. An important part of the GRB research is the investigation of the origin and the emission mechanisms of GRBs. What kind of objects produce such destructive and energetic phenomena? Which role plays the central engine? What happens to the photons before they reach us? These have been central questions for many years and are still not entirely answered, as outlined in Sections 2.3, 2.4 and 2.5. Furthermore, as GRBs are remarkably luminous in the EM spectrum, it is expected that they are sources of other messengers as well. In Section 2.6, it is explained why we scan the sky for coincident observations of neutrino signals, cosmic rays and gravitational waves. To conclude, this chapter ends with an interesting property of GRBs, which was the motivation for conducting the research performed in this thesis. The average power density spectrum of GRBs follows a power-law with slope $b \sim -5/3$, alike the index of the Kolmogorov spectrum in fluid dynamics, hinting at the fact that the observed spectra might reflect characteristics of a turbulent environment. Therefore, the notion of the Kolmogorov turbulence is described in Section 2.7.

2.1 Historical Overview

In June 1973, a paper in the Astrophysical Journal headlined the first observations of gamma-ray bursts [1]. It concerned 16 short photon bursts, detected between July 1969 and July 1972 by the American Vela satellites [2], which were launched in order to monitor the compliance of the Partial Nuclear Test Ban Treaty between the United States, the United Kingdom and the Soviet-Union. The detectors recorded photon bursts with energies between 0.2 and 1.5 MeV, and a duration of less than a second up to several tens of seconds. The time structure was irregular; some spectra showed no peaks, while other spectra had a very distinct structure. Six of those measurements were confirmed as events by another gamma-ray detector on the IMP-6 satellite (NASA) [3,4]. However, it turned out that the first observation of a GRB already dated back to 1967, on July
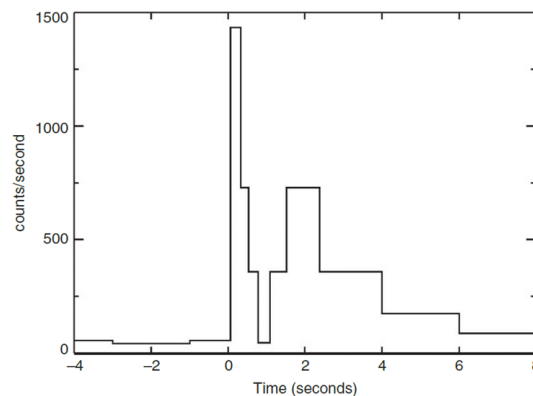
Figure 2.1: Light curve of the first observed gamma-ray burst, detected on 2 July 1967 by the Vela IVa satellite [5].

2nd. Two asymmetric brief peaks and a rapid time structure that, existing for about 10 seconds (see Figure 2.1), did not match any known event, indicating the presence of an unfamiliar gamma-ray source [5].

The rather late discovery of GRBs was due to the fact that the energetic rays cannot penetrate our atmosphere. Against the background of the Cold War, the first satellites with gamma-ray and X-ray detectors were brought into space by the U.S. Air Force in 1963 to probe nuclear tests [6]. No evidence for those tests was observed (besides maybe the so-called Vela incident in 1979 [7]), but the mission marks the start of the interesting observational and theoretical search towards the origin of GRB flashes. In the next thirty years, around 500 GRBs were detected with several gamma-ray detectors (including detectors on the French-Soviet Venera satellite and the Japanese Ginga satellite). However, the bad angular resolution made it very difficult to locate those bursts and to search for their sources or counterparts in different wavelength bands [5,8]. Fortunately, that did not keep theorists from thinking. This is beautifully illustrated by the more than 100 theoretical models that were proposed in the first twenty years to explain the origin of GRBs [9]. Malvin Ruderman, who had read and reviewed most of them, encapsulated in 1975 the theoretical status by the following words:

> "The only feature that all but one (and perhaps all) of the very many proposed models have in common is that they will not be the explanation of γ-ray bursts." (Ruderman, 1975, p. 179) [10]

In 1991, the Compton Gamma-Ray Observatory (CGRO) was launched by NASA. The satellite contained the famous Burst And Transient Source Experiment (BATSE) detector, sensitive to emission in the 20 keV to 2 MeV energy range. CGRO was designated to search for GRBs and did so; during its lifetime, BATSE recorded more than 2700 bursts and established some important facts about GRBs. It confirmed the already long

suspected isotropic distribution of GRBs, identified two categories of GRBs, long and short bursts, and showed that GRB light curves have a non-thermal spectrum [6, 8, 11].

However, the distance measurements provided by BATSE were still not accurate enough to identify the host galaxies and had often error boxes of multiple angular degrees. Typically, such large regions comprise many possible optical sources. That changed when the Italian-Dutch BeppoSAX satellite, equipped with an X-ray detector, was brought into play in 1996. The X-ray detector had a localisation resolution of the order of one arcminute [6]. Since the X-ray sky is not that populated, it became possible to match GRBs with their X-ray afterglows. Subsequently, follow-up spectroscopic searches in other wavelength bands detected optical or radio counterparts [8], which opened the possibility to infer the redshift via spectral analysis, resulting in more accurate distance determinations.

On 28 February 1997, the first optical afterglow was observed for GRB 970228[1], after successful γ-ray and X-ray measurements by BeppoSAX, revealing an extended object, its host galaxy [12]. The redshift could not be determined, but a second burst on 8 May 1997 was observed in X-ray, optical and radio wavelengths. Based on the shift in the emission lines of the spectrum, a redshift of $z = 0.835$ was determined [13]. This formally and quantitatively established the extragalactic and cosmological origin of GRBs [14].

Currently, several gamma-ray detectors are in operation. The Neil Gehrels Swift Observatory (Swift), launched in 2004, contains the Burst Alert Telescope (BAT), which detects gamma-rays, the X-Ray Telescope (XRT) and the UV-Optical Telescope (UVOT). When BAT is triggered by a possible GRB event, Swift rotates very fast towards the direction of the GRB and points XRT and UVOT at the source. BAT only locates the burst within some arcminutes, but XRT corrects the location with a precision of arcseconds. Owing to the fast cooperation of the different detectors, Swift was able to improve the detection of afterglows in the temporal window and in different energy bands. This resulted in the first afterglow detection of a short GRB [15]. The high-quality observations of the afterglows give a better understanding of the environments of the GRBs and allow for better redshift measurements. In 2009, the satellite detected a GRB with a redshift $z = 9.4$ (GRB 090429B), the farthest ever seen [8, 16, 17].

The Fermi Gamma-Ray Space Telescope (Fermi) was launched in 2008 and contains the Gamma-Ray Burst Monitor (GBM, 8 keV - 40 MeV) and the Large Area Telescope (LAT, 20 MeV - 300 GeV). Together, these detectors are able to record more than 7 orders of magnitude in energy. The mission focuses on the observation of the prompt emission over the various wavelength bands and at high energies [18, 19]. Fermi was the first to detect photons with an energy of more than 100 GeV and observed a thermal component in the further non-thermal GRB spectrum [8, 20].

---

[1]The naming convention for GRBs relies on the UTC date on which they are observed. For example, GRB 970228 is observed on February 28, 1997. When more than one GRB is detected on a single day, the name receives the letter 'A', 'B' and so on, or 'FFF', denoting the fraction of the day (in universal time), to distinguish between different events.

Besides Fermi and Swift, some other satellites are taking data at this very moment: the old Konus-Wind (NASA), Integral for ESA, SuperAGILE of the Italian Space Agency, the Japanese MAXI on the International Space Station (ISS) and the Indian AstroSAT [18]. Besides providing data for GRBs, those satellites observe gamma-rays from pulsars, cosmic rays and supermassive black holes in the centres of galaxies [21].

2.2 Observational Properties

In the previous section, some general features of GRBs were briefly mentioned. We will discuss them now in more detail.

2.2.1 Duration

The duration of a gamma-ray bursts is characterised by the 'T90' parameter: the time period during which 90% of the burst's photon counts above background are observed in a certain energy band (for BATSE and Fermi: 50 - 300 keV). The first and last 5% are disregarded, to avoid that random background fluctuations make the bursts look longer. Similarly, the 'T50' parameter can be defined. Note that those parameters are described in the observer rest frame, and are thus affected by redshift and have to be corrected by a factor $(1 + z)^{-1}$ when considering the intrinsic duration of the burst. The observed duration is detector dependent, although it is more convenient to say that it is energy dependent. It is shown that GRBs typically have a narrower time profile in higher energy bands compared to the spectrum in lower energy bands [22, 23]. Generally, a detector sensitive to lower energies will thus detect a longer burst than a detector sensitive to higher energies [8, 18].

The BATSE experiment showed that the T90 distribution of GRBs has a bimodal structure [24]. This is confirmed by other missions, as for example illustrated in Figure 2.2a for Fermi: two peaks appear around 1.05 s and 29.9 s with a local minimum in between at approximately 2 s [19]. As such, the two classifications are called 'short' (T90 $\leq$ 2 s) and 'long' (T90 $>$ 2 s) bursts. This classification is supported by the observation that long GRBs have typically "soft" photons, while short GRBs have "harder" photons, as can be seen in Figure 2.2b. The hardness ratio (HR) is the ratio between the fluence values of two different wavelength bands. For Fermi and BATSE, the comparison is made between the energy bands of 100-300 keV and 50-100 keV. From Figure 2.2b, it is clear that the average energy of short bursts is higher than the average energy of long bursts. This is why GRBs are often classified in *long/soft* bursts or *short/hard* bursts [8, 24].

2.2.2 Isotropy

Already from early observations of gamma-ray bursts, the extragalactic origin of GRBs was suspected. The isotropic distribution on the sky suggested no correlation with the Galactic plane or centre, but the possibility of a halo of GRBs around the galaxy,
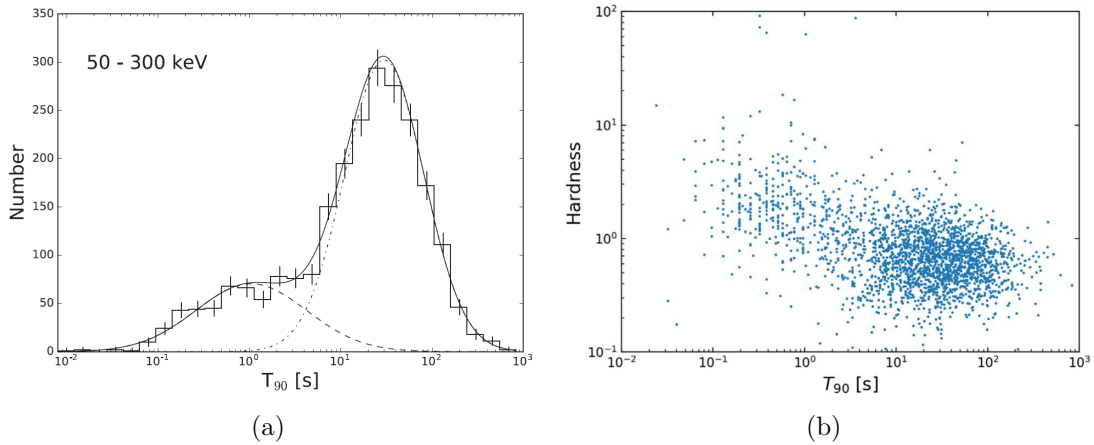
(a)													(b)

Figure 2.2: (a) T90 distribution, computed in the 50 - 300 keV range, of GRBs detected by Fermi during its first ten years of operation (2008 - 2018). The sample consists of 17% short GRBs and 83% long GRBs. (b) Scatter plot of spectral hardness vs. T90 value of the GRBs detected by Fermi during its first ten years of operation (2008 - 2018). An anti-correlation between both parameters can be observed [19].

populated by neutron stars[2], could not yet be entirely excluded. This changed when BATSE detected considerably more GRBs than its predecessors, approximately one per day [26]. As the amount of observed GRBs grew and no anisotropy on the sky was seen, the size of this hypothetical halo also had to grow, pushing the Galactic neutron star model to its limits. Ultimately, it could not explain the observations any longer. Any correlation with the Galaxy was excluded [5]. When BeppoSAX was launched and the redshifts and distances became accessible with better precision, it turned out that GRBs were not only extragalactic, but also cosmological [6, 27].

Another hint of the extragalactic origin came from the fluence distribution of the GRBs. The fluence S of a radiating object at some distance r is given by the time integrated isotropic energy E_{iso} in Euclidean space:

$$S(r) = E_{iso}/4\pi r^2 \propto r^{-2} \tag{2.1}$$

Recalling that the number of sources in a spherical volume is constant assuming a uniform distribution, $n_0 = N/(4/3)\pi r^3$, we find that the number of sources with a fluence higher than the detector threshold S_t is given by:

$$N(> S_t) \propto S^{-3/2}. \tag{2.2}$$

This behaviour was recovered in the data, but shows a deviation at low fluences. A shallower slope is indeed expected below the threshold fluence, but the discrepancy

---

[2]In the 1980s, the Galactic neutron star models were very popular, involving high-velocity neutron stars in the halo that could produce burst-like events [25].

occurred at fluences significantly higher than the threshold. This can be assigned to the effect of the expansion of the Universe, since the cosmological redshift affects the wavelength, and consequently the observed energy of the photons. Additionally, the assumption of Euclidean space breaks down. Only the bursts located at those high redshifts feel the consequences of the expansion, therefore proving their extragalactic nature [5, 8].

2.2.3   Energy and Spectra

Assuming GRBs emit their radiation isotropically, typical energy outputs of these objects cover the range between $E_{iso} = 4\pi r^2 S \sim 10^{46} - 10^{47}$ J, where S is the fluence, the total observed energy per unit area. This corresponds to isotropic luminosities of $L_{iso} \sim 10^{44} - 10^{46}$ J/s for an average GRB duration of the order of 20 s. This can be compared to the luminosity of the Sun, $L_\odot \sim 3 \cdot 10^{26}$ J, or the luminosity of our galaxy, $L_G \sim 10^{37}$ J. GRBs even outshine the most energetic Active Galactic Nuclei (AGNs) by a factor of 10^3, which makes them the most luminous and powerful transient phenomena in the Universe since the Big Bang (in the EM spectrum)[3]. Note that it is generally accepted that GRBs have jets with opening angles between 1° and 20°, beaming the energy in two opposite directions. In this case, the total emitted energy is smaller than the isotropic energy, of the order of 10^{44} J. This is similar to the energy output of a supernova, which naturally become progenitor candidates for GRBs [8, 28, 29].

Sharing their enormous energy outputs, the gamma-ray light curves, which represent the time evolution of the photon counts or flux, differ nevertheless in a great extent. Some are spiky, some are smooth, others have multiple peaks, others have only one. Some examples of light curves are shown in Figure 2.3. They all agree in their rapid variability on very small timescales, down to sub-second scales and of the order of a few milliseconds. The trigger in the left panel (trigger 332) of Figure 2.3 shows how several small variations are superimposed on a slower varying component [6, 8, 18].

Instead of binning the photon count in time, one can also consider the photon count per energy bin. It is shown that this curve can be described by the empirical Band function, which connects two power law functions at a break frequency with energy E_0 [30]:

$$\frac{dN}{dE} = \begin{cases} A \left[\frac{E}{100\text{keV}} \right]^\alpha \exp\left(-\frac{E}{E_0} \right) & E < (\alpha - \beta)E_0 \\ A \left[\frac{(\alpha-\beta)E_0}{100\text{keV}} \right]^{\alpha-\beta} \exp(\beta - \alpha) \left(\frac{E}{100\text{keV}} \right)^\beta & E \geq (\alpha - \beta)E_0 \end{cases} \quad (2.3)$$

Here, A is a normalisation constant and α and β are the low- and high-energetic indices of the power-law, with typical values $(\alpha, \beta) = $ (-1, -2) [31]. The form of the Band function indicates that the spectrum is non-thermal. A thermal spectrum, that arises from a gas

---

[3]GRBs outshine the AGNs during the short time span that they are present. An AGN emits radiation during millions of years, resulting in a larger total energy output than a GRB. Therefore, it is important to distinguish between 'transient' (GRBs) and 'stationary' sources (AGNs).
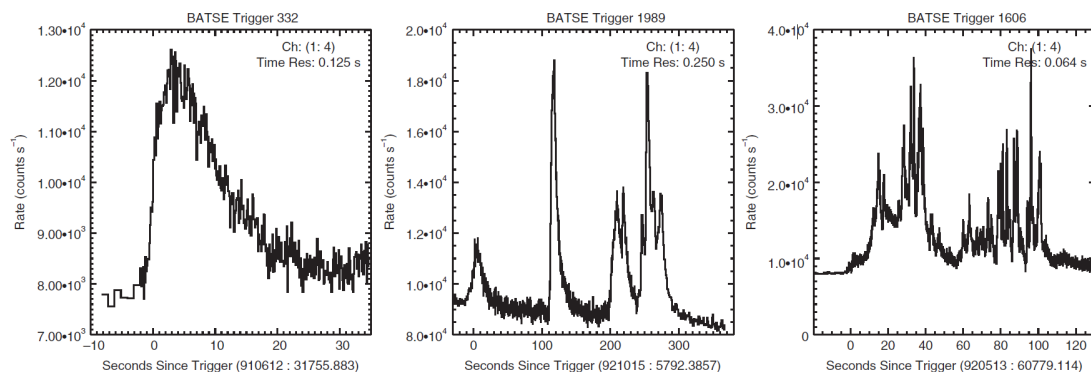
Figure 2.3: Three examples of GRB light curves, recorded by the BATSE detector. Large differences can exist between different light curves. Trigger 332 (left) shows very clearly the sub-second variability on a slowly varying profile [8].

in thermal equilibrium, describes an exponentially decreasing number of photons with energy, as described by Max Planck in 1901 [32]. The amount of photons in a gamma-ray burst however falls off following a power-law, which is explained by particle acceleration in shocks or magnetic fields [8]. The Band function describes the majority of the GRB spectra very well, but there is not yet a theoretical model for the appearance of the spectral function [8].

Often, the energy of the GRB photons peaks between hundreds of keV up to the MeV scale, allowing them to be visible as gamma-rays. Sometimes the signal is so weak that the peak of the spectrum is only seen as X-ray emission. Such GRBs are called *X-ray flashes*. At the high-energy side of the energy peak, there is a long tail towards the GeV scale, with a small amount of GRBs with energies greater than 10 GeV, as detected by Fermi [8, 28, 33].

Observationally, the GRB light curve can be divided in three episodes, as briefly outlined below [8, 28, 34]. The emission mechanisms for the prompt and afterglow phases will be discussed in more detail in Section 2.3:

- Prompt phase: This is the main part of the burst, the brief and energetic flash of gamma-ray emission, outshining its entire host galaxy. The burst can last a few milliseconds up to hundreds of seconds and peaks typically in the MeV range. The emission process of the prompt emission is still a puzzle, but it is thought that the energy is generated in the internal shocks of the collimated ejected plasma.

- Afterglow: The prompt emission is followed by so-called afterglows, which encompass emission in lower-energy bands, often visible for days, weeks or even months after the burst. It appears in all wavelength bands and decays following a power-law. Since the temporal behaviour of the prompt and afterglow episodes is so dissimilar, it is believed that both phases originate from two different processes in

the GRB. It is generally accepted that the afterglow emission originates from the external shock mechanism, where the ejecta collide with the circumburst medium.

- Precursor phase: Some GRBs have a short gamma-ray outburst before the prompt emission. This phase is typically well separated from the main burst, but is weaker in amplitude. Depending on the definition or criteria used to define this precursor, precursors are detected in 3% to 20% of the cases [35]. Their origin is not yet established, but they might be generated during the transition of the ejecta from optically thick to optically thin.

2.3 Theoretical Models of GRBs

The processes that are responsible for the release of the GRB emission still remain unclear. How is the energy from the central engine converted into radiation, how is the jet launched, where is the prompt emission and afterglow emission produced? The most popular theories to explain the characteristics of GRBs are the ultra-relativistic fireball model, associated with shocks, and the electromagnetic model. They differentiate in the amount of energy they dispose in the magnetic fields or matter particles [8, 29].

Compactness Problem

As explained before, the smallest variations in a GRB light curve are of the order of $\delta t \sim 10$ ms. Often, this scale is used to estimate the size of the source D, since variations smaller than $c \cdot \delta t$ would be smeared out by propagation delays within the source. This indicates that $D \sim c\delta t \sim 3 \cdot 10^6$ m. An energy output of $E_{iso} \sim 10^{44}$ J, emitted over a time span of only several seconds and in such a small volume, implies that the photons have enough energy ($E > 2m_e c^2$) and density to undergo pair production, i.e. $\gamma\gamma \rightarrow e^+ e^-$. This means that, due to the constant interactions between photons and electron-positron pairs, the radiation cannot escape the source and photons with energy above $E = 2m_e c^2 \sim 1$ MeV are suppressed. The source is optically thick, as shown below, and thermal radiation is produced. However, observations show that GRBs produce photons with $E > 1$ MeV and have a non-thermal spectrum, according to the Band function of Eq. 2.3. This is called the *compactness problem* [6, 28, 29].

We can roughly estimate the optical depth τ for pair production as $\tau_{\gamma\gamma} \sim \sigma_T n_\gamma D$, where σ_T is the Thomson cross-section, n_γ is the photon number density and D is the size of the source. The number density can be approximated by $n_\gamma \sim E_{iso}/(E_\gamma \cdot D^3)$. Not all photons have sufficient energy to produce electron-positron pairs, so we denote the effective number density as $f \cdot n_\gamma$, with $f < 1$. If we take the isotropic energy $E_{iso} \sim 10^{44}$ J and the average observed photon energy $E_\gamma \sim 1$ MeV, and assume that $\sim 20\%$ of the photons undergo pair production, we are left with:

$$\tau_{\gamma\gamma} \sim 10^{15},$$

which is much larger than 1, and thus the source is extremely optically thick [6, 18]. The problem can be solved by considering a source that is moving relativistic towards the observer. Imagine a source that is moving towards us with a velocity v. It emits two signals with a time difference Δt_e (in the source reference frame). When the source emits its second pulse, it has already propagated a distance $v\Delta t_e$ towards the observer. The observer records a time difference between the first and the second pulse:

$$\Delta t_{obs} = \frac{c\Delta t_e - v\Delta t_e}{c} = \Delta t_e \cdot \left(\frac{c-v}{c}\right) \tag{2.4}$$

One can rewrite the velocity correction factor in terms of the Lorentz factor $\Gamma = 1/\sqrt{1-\beta^2}$ with $\beta = v/c$, if we assume a high relativistic source $\Gamma \gg 1$:

$$\Delta t_{obs} = \frac{1}{2\Gamma^2} \cdot \Delta t_e \tag{2.5}$$

As such, the source size D in the moving frame becomes a factor $2\Gamma^2$ larger than in the reference frame in which the source was at rest, $c\Delta t_e = (2\Gamma^2) \cdot c\Delta t_{obs}$, and the energy is reduced: $E_e = \Gamma^{-1}E_{obs}$, since $\lambda_{obs} = \Gamma\lambda_e$. In this way, the pair-production rate and optical depth decrease significantly. It can be shown that the optical depth drops below unity if $\Gamma \gtrsim 100$ [18, 28, 29].

Fireball Model

The generic model to explain the prompt and afterglow emission of a GRB starts with a stellar mass object, which undergoes a very erratic, catastrophic event. A large amount of energy is produced and released in two opposite jets in the form of several shells, which are analogous to 'fireballs'; large amounts of energy in a small volume in space. The outflow consists of photons, matter (hadrons, electrons, positrons) and magnetic fields. At first instance, the outflow is optically thick due to the high pair-production rate, since the high temperature causes thermal equilibrium between the photons, electrons and positrons. The internal pressure pushes the shells outwards, and thermal energy is adiabatically transformed into kinetic energy. The outflow expands relativistically, with the Lorentz factor $\Gamma \propto r$, where r is the distance from the origin of the jet. It cools down and the pair-production rate drops until no electron-positron pairs are produced any longer. This only happens at large distances from the central engine, $r \sim 10^4 - 10^5$ km. When the maximum Lorentz factor is reached, i.e. when most of the thermal energy is converted into bulk kinetic energy, the outflow reaches a constant speed. As it continues propagating outwards, the internal shock formation (see below) reduces the average Lorentz factor and the outer shell starts gaining mass by gathering material from the circumburst medium. The shell starts decelerating, typically at $r \sim 10^{11} - 10^{12}$ km, and eventually fades away [6, 8, 18].

The various shells differ in masses and travel at different relativistic speeds, hence they will have different Lorentz factors Γ. Faster propagating shells can catch up with slower shells, generating internal shocks, which convert the kinetic energy into radiation, and

forming one shell. The shocks support particle acceleration processes, in which the electrons can participate, radiating synchrotron emission and inverse Compton-radiation[4] or one of the two, to discard their energy again. This process shows the right characteristics to explain the prompt emission of GRBs [6, 18, 29].

When the outflow encounters the surrounding circumburst medium, new shocks are created, which will again be a source of particle acceleration. Forward shocks will accelerate electrons, of which the synchrotron emission explains the afterglow observations very well. Some electrons might participate in inverse Compton processes or synchrotron self-Compton processes[5], scattering photons to higher energies. In some cases, a reverse shock is launched, which re-accelerates the electrons of the shell and produces a strong optical, infrared (IR) and/or radio burst. This is indeed observed in some GRBs as an "optical flash" and radio flare (GRB 990123, GRB 021211). These optical and radio photons can interact with the protons, accelerated to high energies in these reverse shocks, through photo-meson interactions (discussed in Section 2.6). It is believed that these interactions produce high-energetic neutrinos [37, 38]. As the outflow loses more and more energy by the synchrotron emission of the particles, it starts to slow down and the peak of the emission shifts from the high-energy bands (soft γ-rays and X-rays) to lower ones (visible light and radio waves). The burst fades away, as expected for afterglow emission [5, 6, 18, 29]. An artistic view on the shock formation is shown in Figure 2.4 [39].

Electromagnetic Model

The electromagnetic model starts from the same ingredients as the fireball model, but states that the present magnetic fields play a more important role, whereas the fireball model is a matter-dominated model. Again, the central engine is a compact object with an accretion disc, but in this case, it should be rapidly spinning, such that the magnetic field lines wrap around the rotation axis in the azimuthal direction and the outflow is trapped within the field lines. When the central engine subsequently shuts off, the magnetic structure is decoupled and is ejected into the interstellar medium. In the ejecta, the electrons are accelerated and produce synchrotron radiation. This can happen through, as opposed to the shock formation in the fireball model, current instabilities which cause dissipation of the magnetic energy into heat, bulk motion of the plasma and high-energy particles [6, 8, 29, 40, 41].

---

[4]Synchrotron emission is EM radiation, produced by relativistic electrons in a magnetic field, subject to the Lorentz force. The inverse-Compton process includes the scattering of relativistic electrons and low-energy photons, where the photons receive energy from the electrons [8].

[5]Synchrotron self-Compton interaction is the production of synchrotron photons by relativistic electrons, after which the same electrons upscatter their own synchrotron photons to higher energies [8, 36].
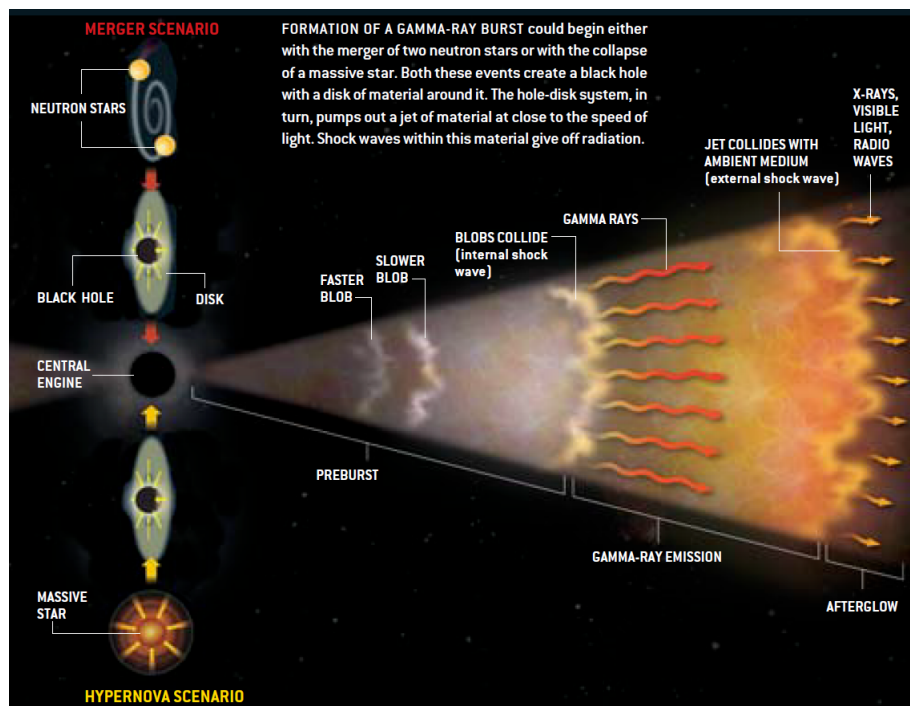
Figure 2.4: Artistic illustration of the fireball model. On the left, the central engine (a black hole with an accretion disc) is either formed out the collapse of a massive star or a binary merger. On the right, the jet structure with the internal and external shocks is shown, together with the different types of radiation that are released [39].

2.4   Jet Mechanisms

It can be argued that the outflow is not spherical, but collimated into two jets back to back. However, direct evidence of jets cannot be observed, since, in contrast to phenomena such as AGNs, images of GRBs are often unresolved, not supporting a direct study of the outflow structure [5]. Nevertheless, some indirect arguments are present:

- Energy: The isotropic energy of the gamma-ray radiation in GRBs can reach such high values, that it approaches or even exceeds the rest mass of the Sun, $M_\odot c^2$. This conflicts with the hypothesis that GRBs arise from stellar mass progenitors. If the radiation is beamed in two jets, the energy output is reduced by several orders of magnitude. This is supported by long-term radio observations. After several months or years, the burst is visible in radio wavelengths, where it radiates isotropically. Estimating the total energy at those late times, reveals energy outputs around 10^{44} J, consistent with collimated emission in jets [29].

- Achromatic steepening: The afterglow emission of some GRBs shows a sudden break in the photon flux, occurring in all wavelength bands simultaneously (= achromatic), as is illustrated in Figure 2.5. The break can be explained by the appearance of jets, and is a combination of two effects:

  Relativistic beaming. In the rest frame of the relativistic shell, the emission is radiated isotropically, while in the rest frame of the observer, the emission is beamed along the direction the shell is moving in and arrives under an angle $\tan \theta_b = \Gamma^{-1}(c/v)$, which can be approximated by $\theta_b \sim \Gamma^{-1}$ [29].

  Jet opening angle. When we assume that the matter is not emitted isotropically, but in jets, an observer only receives the radiation when the jet points towards her. Jets in the case of GRBs typically have an opening angle $\theta_j \sim 1° - 10°$ [6].

  During the acceleration phase of the outflow, as discussed in Section 2.3, the Lorentz factor Γ increases with the distance r. Hence, θ_b becomes smaller and $\theta_b \ll \theta_j$. An observer cannot judge whether the outflow is collimated or isotropic. However, in the deceleration phase, Γ decreases and θ_b increases. At some instance, $\theta_b \gtrsim \theta_j$ and the photon flux decreases suddenly faster, since light starts to fall outside the cone that is visible for the observer. This is observed in some GRBs, as shown in Figure 2.5. In addition, so-called 'orphan afterglows' are observed; optical and radio afterglows without the main gamma-ray prompt emission. The existence of jets predicts such lonely afterglows, since the observer receives light from the extending jet only when the angle of the observer w.r.t. the jet axis θ_{obs} is smaller than θ_j, but the prompt emission was radiated when $\theta_{obs} > \theta_j$. However, the identification of the orphan afterglows is complex, since other transient phenomena can often not be ruled out completely as the source of the emission [5, 6, 18, 28].

If GRBs have beamed emission, this implies that the satellites orbiting Earth only detect the GRBs that are directed towards us. From the present beaming angles, it can be
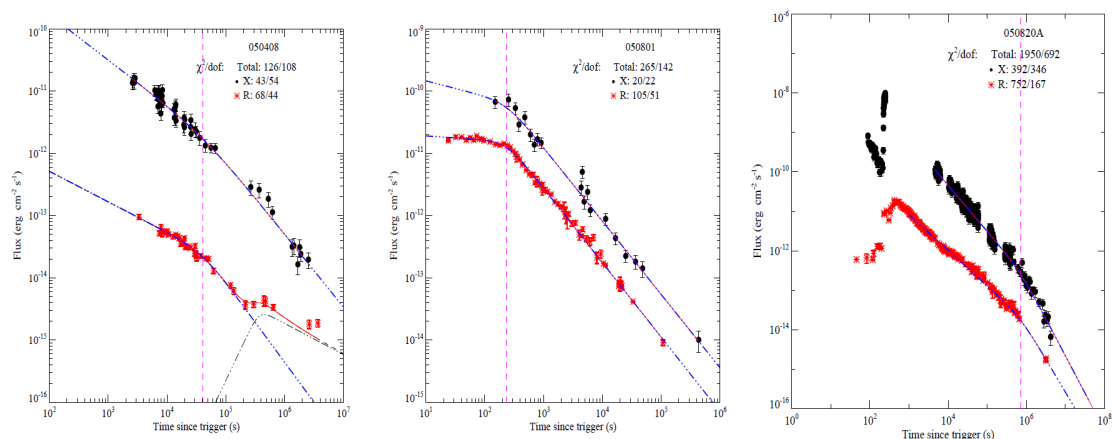
Figure 2.5: Observed X-ray (black) and optical (red) light curves of three different GRBs. The dashed purple line denotes the time of the achromatic break. The dotted-dashed lines are the best fits to the light curves, which are not relevant here [42].

estimated that there should be $\sim 100-1000$ GRBs occurring each day in the Universe [6]. Two processes are likely to provide the energy for these jets: neutrino-antineutrino annihilation and the magnetic jet model.

Neutrino-antineutrino annihilation. At a radius sufficiently close to the black hole and a temperature sufficiently high, electron and positron capture processes take place: $e^- + p \rightarrow n + \nu_e$ and $e^+ + n \rightarrow p + \bar{\nu}_e$. These neutrinos are the only particles that can escape the disc and take energy with them. When neutrino-antineutrino pairs annihilate above the disc, they produce photons and electron-positron pairs, and along with some hadrons (resulting from quark-antiquark pair production), they form a hot "fireball" [8].

Magnetic jet model. The orbiting matter around the black hole carries a magnetic field. When open magnetic field lines are present that thread the black hole while they are also connected to matter particles, they can wind up due to the rotation of the central object. They get twisted and exert a torque on the black hole, causing it to slow down. The energy of the rotation is then used to eject material along the rotation axis [8, 43].

2.5 Progenitors

Various models exist to explain the characteristics of the emission of GRBs, but what kind of astrophysical objects precede the GRB? According to the observations, the progenitor system should have the following features:

- Energy: The progenitor should be able to cause an explosive event in which an energy output of $\sim 10^{44}$ J is produced, but not instantaneously (over a duration of tens of seconds).

- Variability: The smallest variability in the light curves is of the order of milliseconds, which implies that the source is not larger than several 10^3 km, as discussed in Section 2.3.

- Collimation: The emission is beamed into two collimated back-to-back relativistic jets. The progenitor system should be able to launch a jet.

Due to the size, the large energies involved and the relativistic outflow, it is natural to invoke compact objects, such as neutron stars and black holes. To explain the prolonged duration of the energy output and the jet formation, a model with an accretion disc, which feeds the black hole and the jets, is proposed [8,29]. When over the years it became clear that there are two major groups of GRBs, long/soft and short/hard GRBs, it was suggested that they could have different progenitors. A big step forward in this search was the detection of the afterglow emission in 1997. Not only was it possible to locate the bursts with improved accuracy on the sky, but we were also able to investigate the GRB environment and search for additional features and imprints that could tell us more about the origin of the GRBs, e.g. supernova signatures in the spectra of GRBs or spectral lines in the emission of host galaxies. A connection between long GRBs and star-formation regions became clear, while short GRBs emerged 'everywhere', in galaxies with low and high star formation rate, or not connected to any galaxy [5,44].

In this section, the most accepted models for GRB progenitors are described: the collapsar model for long GRBs and the compact binary model for short GRBs [6].

2.5.1   Long GRBs: Collapsar Model

Observationally, long GRBs are related to host galaxies with a high star-formation rate and are found in the vicinity of star-forming regions. This suggests that long GRBs might arise from the death of young, massive stars. This theory is strengthened by the connection between some long GRBs and supernova Type Ic (SNe Ic). As stated by the collapsar model, the progenitor of the long GRB is a massive star that collapses gravitationally at the end of its lifetime, forming a neutron star (NS) or black hole (BH). This star should be massive, $M > 30M_{\odot}$, and rapidly rotating, such that a jet and an accretion disc can be formed. Since the SNe Ic do not have any hydrogen or helium absorption lines in their spectra, the star should have lost its outer hydrogen and helium shells. A prime candidate is a Wolf-Rayet (WR) star, which is a hot, evolved star with initial masses of more than $20M_{\odot}$. They have strong stellar winds, causing mass loss rates of $\sim 10^{-5}$ $M_{\odot}$ yr^{-1}, by which the star is shedding off its outer layers [6,8,18].

When the core of the star becomes unstable and the degenerate electron or neutron gas can no longer deliver enough pressure to resist the gravitational force, the star collapses into a rapidly spinning neutron star or black hole. The material of the stellar envelope in the equatorial plane has a high angular momentum and forms an accretion disc around the compact object. The matter in the direction of the rotation axis does not rotate and falls directly on the surface, where it leaves behind a low-density funnel and creates a
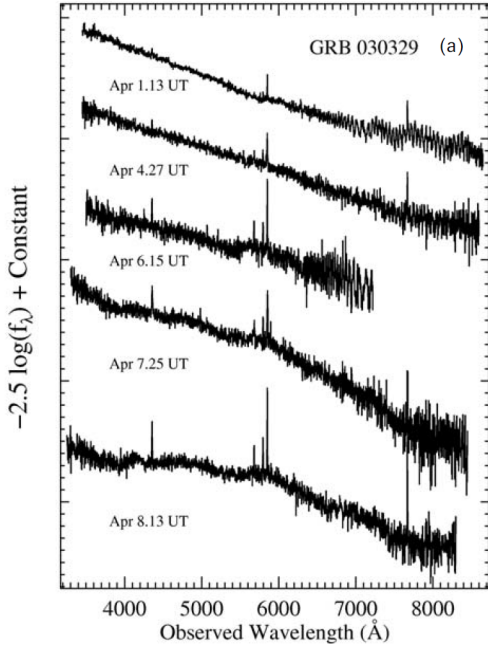
Figure 2.6: Evolution of the optical afterglow of GRB 030329 that was detected in coincidence with SN 2003dh. The first light curve was recorded 2.64 days after the burst (April 1.13 UT), the last light curve was taken 9.64 days after the burst (April 8.13 UT). It is clear how the power-law spectrum changes into a light curve which consists of a bump and broader emission lines, characteristic for a SN [29].

shock wave. This mass distribution allows for a jet to emerge along the rotation axis, that will eventually be detected as a GRB (if collimated in the direction of Earth). This entire process only takes about 10 seconds, while the accretion on the surface may take tens of seconds. This implicates that the core-collapse of a WR star can only produce long GRBs [5, 28, 29].

Observational Evidence

The first detection of a GRB in coincidence with an SN Ic happened in 1998, but gave only weak proof for the connection between both phenomena. GRB 980425 was a dim GRB and had no optical afterglow [45]. Nevertheless, five years later, GRB 030329 and SN 2003 established the link. The GRB was a luminous burst and had a very bright afterglow. After several days, the afterglow emission started to display more and more SN features. A bump appeared in the power-law spectrum. After subtracting the afterglow emission, the SN spectrum could be isolated [5, 46].

Only for a small fraction of long GRBs, a coincidence with a supernova is detected. Nevertheless, it is widely accepted that long GRBs are linked to the death of massive stars, since they populate regions with intense star formation [6]. Alternative models to explain long GRBs are mergers of binary systems with a helium star and neutron star or black hole, with white dwarfs, carbon-oxygen cores, et cetera. Often they do explain some special GRBs with anomalous features. To e.g. explain the ultra-long GRBs with $T_{90} > 10^3$ s, blue supergiants are proposed as progenitor, since a system with a WR star as progenitor is unlikely to power the central engine for more than 15 minutes [8, 18].

2.5.2 Short GRBs: Compact Binary Merger Model

Short GRBs are believed to originate from the merger of a compact binary system. Compact binary systems can consist of white dwarfs, neutron stars or black holes, but only two are suspected to be possible candidates, since we need a black hole/accretion disc system: NS-NS and BH-NS [28].

The merger starts with the in-spiral phase, during which the orbital separation between the objects and the period decrease, caused by the emission of gravitational waves. This phase can be of the order of several Myr up to some Gyr. This process was demonstrated by the Hulse-Taylor pulsar (PSR 1913+16), consisting of two neutron stars [47]. When the objects arrive within a few times their radii, they tidally distort each other and long spiral arms are created, carrying the excess angular momentum. The objects collide and fuse together, and collapse into one object, a black hole. The stellar debris, that is not ejected in the interstellar medium, forms an accretion disc around the black hole and will feed the central engine and the jet structures that arise [6, 28].

Observational Evidence

Short GRBs do not show a connection with particular regions or galaxies. They are found in elliptical galaxies, in star-forming regions and at significant off-sets from nearby galaxies. All those observations support the compact binary merger model. The in-spiral phase can proceed very fast, not giving much time to the binary to propagate away from the birthplace. Similarly, there are binaries which arise from ancient star populations. When both compact objects result from a supernova explosion, the system might have experienced substantial kicks due to those explosions or the mass losses, and is pushed away from the host galaxy [6, 44]. However, the most important piece of evidence is the simultaneous observation of gravitational waves and GRB emission. In 2017, the LIGO/VIRGO Collaboration detected the GW 170817 event, which was associated with the short GRB 170817A detected by Fermi and Integral, as will be discussed in Section 2.6 [8].

2.6 Multi-Messenger Astronomy

Besides being the most luminous transient objects in the Universe, GRBs are believed to emit also non-electromagnetic signals. Three other messengers that are possibly produced by GRBs are high-energy neutrinos, ultra-high-energetic cosmic rays (UHECRs) and gravitational waves.

Neutrinos and UHECRs

It is assumed that electrons and positrons are accelerated to high energies in the relativistic outflow of the jets. As such, they can produce the observed prompt and afterglow radiation. At the same sites where those electrons reach high energies, protons could

be accelerated up to energies $E \gtrsim 10^{20}$ eV. This can take place at several stages, e.g. during the internal and external shocks, or in the accretion disc or flow onto the central object. High-energy protons interact with photons and produce pions through a Δ^+ resonance, provided that the energy of the initial proton and photons is sufficiently high to create the Δ^+ baryon (uud) with mass $M_{\Delta^+} \simeq 1.23$ GeV. The pions decay and produce neutrinos, amongst other leptons and photons:

$$p + \gamma \rightarrow \Delta^+ \rightarrow \begin{cases} n + \pi^+ \rightarrow n + \mu^+ + \nu_\mu \rightarrow n + e^+ + \nu_e + \bar{\nu}_\mu + \nu_\mu, \\ p + \pi^0 \rightarrow p + \gamma + \gamma. \end{cases}$$

From the kinematic condition, $E_p \cdot E_\gamma \gtrsim 1.6 \cdot 10^{17}$ eV^2, one derives that the interaction happens for a typical optical photon when $E_p \gtrsim 10^{16}$ eV. Since the protons can reach higher energies in GRBs, this is not a stringent condition. It is expected that neutrinos with a broad energy range are produced, up to 10^{19} eV, originating from different regions in the GRB mechanism. However, no neutrino signal has yet been observed in coincidence with a GRB observation [8, 48].

Assuming that protons are accelerated, it is expected that GRBs also produce UHECRs. Cosmic rays are charged particles, consisting of protons and nuclei up to iron, that arrive at Earth and interact with the atmosphere. Their energy spectrum shows a power-law with spectral index of about -2.6 and covers more than 11 orders of magnitude in energy. UHECRs are the cosmic rays with the highest energies, $E > 10^{18}$ eV. It is suspected that around this energy a shift happens and the observed cosmic rays start to have extragalactic origins. They can only be produced in the most energetic phenomena, such as AGNs and GRBs. However, the absence of any neutrino observations in coincidence with GRBs puts strong constraints on the models that propose GRBs as dominant UHECR sources [5, 8, 48].

Gravitational Waves

As was discussed in Section 2.5, the leading model for the origin of short GRBs is a compact binary system, which merges and collapses into a black hole. This can be either a NS-NS system or a NS-BH model. A BH-BH model is less likely, since a system with a neutron star provides material to form an accretion disc around the black hole, which is generally assumed to provide energy for the jet formation. Compact binary systems are acknowledged as sources of gravitational waves, and thus it is legitimate to anticipate on gravitational wave signals in coincidence with a short GRB [8, 28].

The first gravitational wave signal that was detected together with a GRB signal arrived on August 17, 2017 and was observed by the Advanced LIGO (Laser Interferometer Gravitational-Wave Observatory) and Virgo detectors [49, 50]. Approximately 1.7 s later, Fermi and Integral (INTErnational Gamma-Ray Astrophysics Laboratory) reported about GRB 170817A [51–53]. It is indeed expected that the electromagnetic
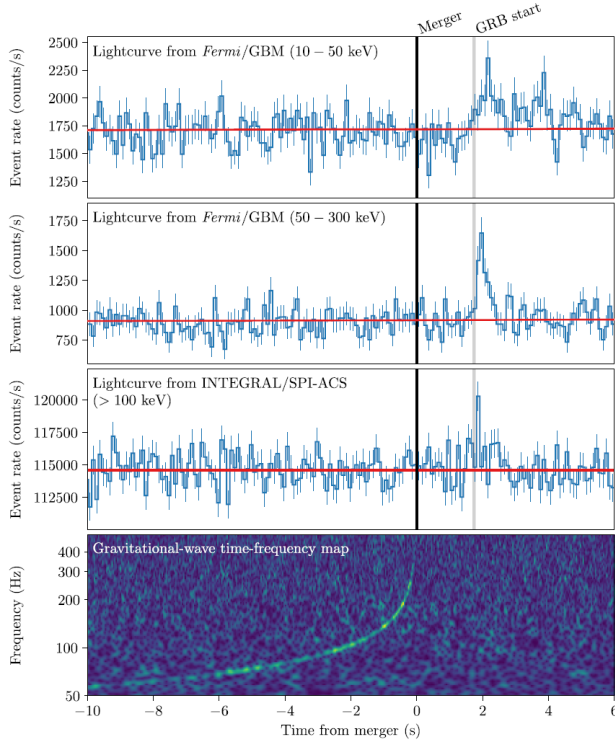
Figure 2.7: Multi-messenger detection of the binary neutron star merger in NGC 4993, detected as GRB 170817A by the γ-ray detectors GBM (Fermi) and SPI-ACS (Integral) and as GW 170817 by the interferometers of LIGO and Virgo. *Top three panels:* Light curves of Fermi/GBM in two energy bands (NaI detectors 1, 2 and 5) and of INTEGRAL/SPI-ACS in the highest energy band of GRB 170817A. *Bottom panel:* Combined time-frequency map of LIGO-Hanford and LIGO-Livingstone data of the gravitational wave event GW170817. Time zero is the trigger time of GW 170817 [49].

signal is delayed by a few seconds, since the central engine and jet launch are formed within several seconds after the merger. GW signals and EM signals are expected to travel at the same speeds. The signals of the different detectors are shown in Figure 2.7. This was a short GRB with T90 $\sim$ 2 s [49]. The LIGO interferometers pinpointed a region of 28 deg^2 as the origin of the source. A follow-up electromagnetic search revealed an optical signal $\sim$ 11 hours after the merger [54]. Signals in X-ray, radio, ultraviolet and infrared were also detected. Neutrino and cosmic-ray observatories also searched for an excess, but did not report on successful results [55]. The galaxy NGC 4993 was identified as host galaxy. From the gravitational wave signal, it was derived that the system consisted of two neutron stars, which collapsed into a compact object of $\sim$ 2.8 $M_\odot$, probably a black hole [55].

The event is one of the closest GRBs known (together with GRB 980425), at a distance of $\sim$ 40 Mpc, but was extremely weak. It is believed that the jet was not pointed towards us and we only received a fraction of the true energy output [49]. Therefore, the afterglow emission of the GRB was not detected. The emission in all wavelength bands originated from the kilonova explosion that followed the burst [56, 57]. During the merger, part of the material of the neutron star is ejected into the interstellar medium. This consists of neutrons and elements up to iron. In the ejecta, neutron capture processes (r-processes) take place, during which neutrons are absorbed before they can decay into protons. Unstable, heavier elements are created, which rapidly decay with a release of photons. These photons cannot escape due to the large density and opacity of the ejecta, and

are again absorbed until they are converted into thermal energy, which appears in all wavelengths but peaks in the optical and infrared bands [8].

The simultaneous detection of GRB 170817A and GW 170817 was a milestone for both messenger fields. GW 170817 was the first NS-NS binary merger, and the first GW event for which an electromagnetic counterpart was observed. On the other hand, GRB 170817A was the first GRB event that was observed through gravitational waves, immediately confirming that, at least some, short GRBs are born in the merger of two neutron stars [49, 55].

2.7 Kolmogorov Turbulence

As discussed in Section 2.2.3, the time spectra of GRBs differ a lot between each other and show variability on scales of milliseconds up to seconds. Often, the spectra are transformed to frequency space through Fourier transforms to extract information about periodicity, of which the typical frequencies would appear as clear peaks in the Fourier spectrum. A characterisation of the variability would constrain models that try to explain the radiation mechanisms of the gamma-ray emission, of which is still little known. Unfortunately, no periodicity is observed for GRB light curves [8].

Nonetheless, in 1998, Beloborodov, Stern and Svensson showed that their sample of long and bright BATSE GRBs exhibited an average power density spectrum that followed a power-law function with exponent $\alpha = -5/3 \sim -1.67$, as is shown in Figure 2.8 [58]. This was later confirmed for other samples of GRBs and in other energy bands as well [59–62]. A power-law distribution is a spectrum that is characterised by a straight line in log-log space and is thus of the form: $p(x) = C \cdot x^{-\alpha}$, where α and C are constants. It is the representation of a scale-free system, i.e. the system satisfies the following condition, for any constant b:

$$p(bx) = g(b) \cdot p(x). \tag{2.6}$$

At any value for x, the spectrum only changes by a multiplicative factor [63]. Since the slope of the power-law function is equal to $-5/3$, the connection with the Kolmogorov theory or the Kolmogorov spectrum of velocity fluctuations in turbulent media was suggested [58]. To explain this, a short introduction to fluid dynamics is necessary.

Turbulent Flows

The dynamics of a fluid are given by a set of non-linear partial differential equations, called the Navier-Stokes equations, and describe the evolution of the parameters of the flow (velocity, pressure, temperature and density), as a function of position and time. There is no general solution to the equations, but typically two regimes are distinguished: laminar flows and turbulent flows. Laminar flows (or 'stable' flows) are ordered and layered. Their evolution can be predicted and they are not sensitive to small variations
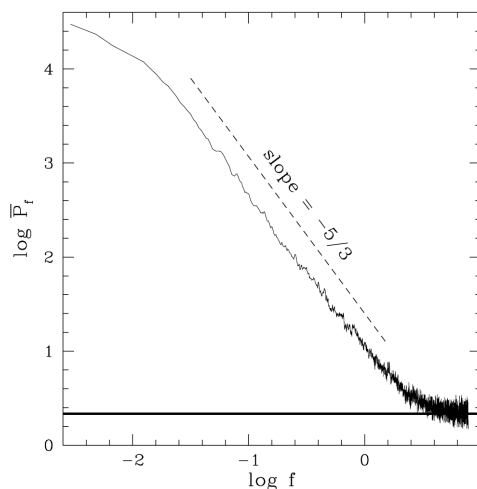
Figure 2.8: Average PDS for the sample of long ($T90 > 20$ s) and bright (count rates
> 250 counts per 64 ms bin) GRBs that were observed in the 50 - 300 keV energy
band by BATSE. The x axis reflects the frequency spectrum obtained from the Fourier
transformed time series. The dotted line has a slope of -5/3 for comparison. The solid
horizontal line shows the averaged normalised Poisson level of the sample, illustrating
that the Poisson fluctuations become dominant at high frequencies, $f \simeq 1$ Hz [58].

in the initial or boundary conditions. Turbulent flows (or 'unstable' flows) however are
chaotic, disordered and are susceptible to small variations. After a short while, they
start to fluctuate and become totally unpredictable [64].

Nevertheless, from the simpler Burgers equation,

$$\frac{\partial u}{\partial t} + u\frac{\partial u}{\partial x} = \nu\frac{\partial^2 u}{\partial x^2}, \tag{2.7}$$

the behaviour of the turbulent flow can be understood. Here, ν is the viscosity of the
fluid and u is the velocity. The second term on the left is the non-linear destabilising
advection term. The term on the right is the friction term, which will have a stabilising
role. Turbulent flows appear in vortex-like structures, which are called 'eddies', and
appear in different sizes. The size of an eddy is often seen as the scale over which the
velocity in a flow varies substantially, and can be as large as the region in which the
flow takes place. It is found that there are again two subregimes in the turbulent flow,
defined by the Reynolds number, which is the ratio between the non-linearity and the
friction. For small Reynolds numbers, friction dominates over the non-linearity and the
solution is found 'stable'. This happens at very small scales, much smaller than the
dimension of the eddy. This is called the microstructure. For large Reynolds numbers,
the non-linearity is much larger than the friction. This happens at scales of the order of
the dimension of the eddy, which is considered as the macrostructure [64–66].

Kolmogorov's relation states that the macrostates, and thus the largest eddies, contain
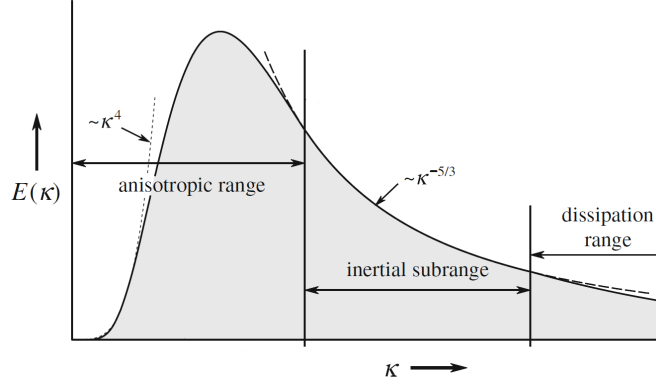
Figure 2.9: The Kolmogorov energy spectrum, where the anisotropic range refers to the large eddies, containing the bulk of the energy. The dissipation range corresponds to the small eddies and has a more complex scaling relation. The inertial subrange displays the $\sim \kappa^{-5/3}$ and represents the energy cascade [64].

most of the energy of the flow. They receive their energy from the instabilities that are created in the flow, but become unstable and break up into smaller structures, until the eddies are sufficiently small to become stable and dissipate their energy as heat by friction processes. This process is called the 'energy cascade'. It is found that this process defines in a large extent the Kolmogorov energy spectrum. In the intermediate region, between large eddies with large amounts of energies, and small eddies with small amounts of energy due to their dissipative nature, the energy spectrum follows the power-law:

$$E(k) \propto \epsilon^{2/3} k^{-5/3}. \tag{2.8}$$

Here, $E(k)$ is the kinetic energy per unit mass fluid, ϵ is the dissipated energy and k is the wave number $k \sim 1/l$, where l corresponds to the length scale of the turbulent motion. The spectrum is shown in Figure 2.9. Large k values correspond to small eddies, while small k values correspond to large eddies. The dissipated energy ϵ denotes the continuous energy flux between the eddies of different scales [65, 66].

The wave number k is proportional to the frequency f, and we know that the energy in function of frequency can be defined by the Fourier transform. This connects the Kolmogorov spectrum with the (average) PDS of the GRBs. Their shared index suggests that turbulence plays a role in the emission process of GRBs. Incorporating the power-law puts new constraints on theoretical models. The observed PDS can for example be obtained by the propagation of the relativistic jet through the stellar envelope of the progenitor, or it appears for certain values of parameters involved in the internal shock model. It can arise from turbulence in the accretion disc or can be related to the progenitor [62]. These are only some examples and it can be concluded that a better understanding of the power-law behaviour for different samples of GRBs and in different energy bands may strengthen and extend these constraints. This is exactly the goal of the research described in this thesis.

Chapter 3

Fourier Transforms

In this thesis, we aim to deepen our understanding of the power-law behaviour of the average power density spectrum. Therefore, we need to set up the framework to transform the time spectra to frequency space. We make use of the Fourier transformation, which is the subject of this chapter. In Section 3.1, we shortly revisit the mathematical construction of the continuous and discrete Fourier transform, after which we set up a toy model in Section 3.2 to systematically investigate the characteristics that we may expect when studying the Fourier transformed time series of our GRBs.

3.1 Mathematical Overview

The Fourier transform is named after the French mathematician and physicist Jean Baptiste Joseph Fourier. As the scientific adviser of Napoleon Bonaparte, he was interested in heat propagation and formulated the well-known diffusion equation or heat equation [67]. This is a partial differential equation, and while he was looking for solutions to this equation, he claimed that any continuous periodic function can be decomposed into a well-chosen sum of sine and cosine waves. Another physicist of that time, Joseph Louis Lagrange, stumbled upon that statement and rejected it. He declared that this decomposition was incorrect for continuous signals with corners, i.e. square waves. As Lagrange was the reviewer of his paper, Fourier never published it. Only many years later, it became clear that a summation of sinusoids could indeed not reconstruct a continuous signal with a corner. However, the constructed signal approaches the original signal very well, until they differed with 'zero energy', i.e. something we know today as the Wilbraham-Gibbs phenomenon [68,69]. Thus, it seems that both were right in that time [70,71]. Today, the Fourier analysis is an essential tool in digital signal processing and data analysis and has applications in almost all scientific fields [72].

A piecewise continuous function $f(t)$ can be written as the infinite sum of an orthonormal set of basis functions $B_n(t)$ multiplied with coefficients c_n [72]:

$$f(t) = \sum_{n=0}^{+\infty} c_n B_n(t). \tag{3.1}$$

The complex Fourier series adopts trigonometric functions as basis functions, which can be written in an exponential form by the Euler equation: $e^{int} = \cos(nt) + i\sin(nt)$, periodic outside the range $[-\pi, +\pi]$. If we assume that the function $f(t)$ has an arbitrary period $2T$, we have:

$$f(t) = \sum_{n=-\infty}^{+\infty} c_n \, e^{\pi int/T}. \tag{3.2}$$

Since the different basis functions are orthonormal, the general form for the coefficients can be found by multiplying both sides of the equation with $e^{-\pi imt/T}$ and integrating over one period, i.e. from $-T$ to $+T$:

$$\int_{-T}^{T} f(t) \, e^{-\pi imt/T} \, dt = \sum_{n=-\infty}^{+\infty} c_n \int_{-T}^{T} e^{\pi i(n-m)t/T} \, dt. \tag{3.3}$$

The left-hand side vanishes, except for the case $m = n$. Then we find for the coefficients the following expression:

$$c_n = \frac{1}{2T} \int_{-T}^{T} f(t) \, e^{-\pi int/T} \, dt. \tag{3.4}$$

We can use this expression to derive the Fourier Transform pair from the complex Fourier series. If we rewrite c_n in Eq. 3.4 as $c_n = F_n/2T$, where F_n is simply

$$F_n = \int_{-T}^{T} f(t) \, e^{-\pi int/T} \, dt, \tag{3.5}$$

then $f(t)$ becomes:

$$f(t) = \frac{1}{2T} \sum_{n=-\infty}^{+\infty} F_n \, e^{\pi int/T}. \tag{3.6}$$

If we define the 'frequency' $\omega_n = n\pi/T = n\Delta w_n$:

$$f(t) = \frac{1}{2\pi} \sum_{n=-\infty}^{+\infty} F_n \, \Delta\omega_n \, e^{i\omega_n t}, \tag{3.7}$$

$$F_n = \int_{-T}^{T} f(t) \, e^{-i\omega_n t} \, dt. \tag{3.8}$$

Taking the limit $T \to \infty$:

$$f(t) = \frac{1}{2\pi} \int_{-\infty}^{+\infty} F(\omega)\, e^{i\omega t}\, d\omega, \tag{3.9}$$

$$F(\omega) = \int_{-\infty}^{+\infty} f(t)\, e^{-i\omega t}\, dt. \tag{3.10}$$

$F(\omega)$ is called the Fourier transform of the function $f(t)$, while $f(t)$ is the inverse Fourier transform of $F(\omega)$. Together, they form the Fourier transform pair. The discrete Fourier transform (DFT) pair is derived easily from Eqs. 3.5 and 3.6 by considering a uniform sampling of the function $f(t)$ with sampling interval Δt. Then $f_m = f(t_m)$ with $m = 0, 1, ..., N-1$. Defining t_m as $t_m = m\Delta t$ and $N = T/\Delta T$, we arrive at:

$$f_m = \frac{1}{N} \sum_{n=0}^{N/2} F_n\, e^{2\pi i n m/N}, \tag{3.11}$$

$$F_n = \sum_{m=0}^{N-1} f_m\, e^{-2\pi i n m/N}. \tag{3.12}$$

Note that the normalisation factor $1/N$ varies in the literature. The normalisation above is called the 'backward' normalisation. Instead, one can choose to add the $1/N$ factor to Eq. 3.12, i.e. the 'forward' normalisation, or a factor $1/\sqrt{N}$ to both equations, which is the called the 'symmetric' normalisation. In practice, numerical programmes can only handle discrete functions [71]. Therefore, we will focus on the discrete Fourier transform from now on. With the Euler equation, we can decompose Eq. 3.12 into sine and cosine waves:

$$F_n = \sum_{m=0}^{N-1} f_m \left[\cos\left(\frac{2\pi n m}{N}\right) - i \sin\left(\frac{2\pi n m}{N}\right) \right]. \tag{3.13}$$

The Fourier transform F_n is thus a complex function of length N, consisting of a real even part and an odd imaginary part. The component at $n = 0$, F_0, is called the DC component, referring to a constant voltage (or current), since for $n = 0$, $f = 0$. In the 'forward' normalisation, this is equal to the average of the time signal, while in the 'backward' normalisation, F_0 corresponds to the area under the curve. The frequency at $F_{N/2}$ corresponds to the Nyquist frequency, which is half the sampling rate. The Fourier transform is symmetric around zero, with the positive frequencies contained in F_0 to $F_{N/2}$ and the negative frequencies between $F_{N/2}$ and F_{N-1}. The negative frequencies do not contain extra information, and are often disregarded [70–72].

3.2   Toy model

Having considered the framework of the DFT, we want to investigate how different features in the light curves of the GRBs are introduced in the DFT of the signal. Since
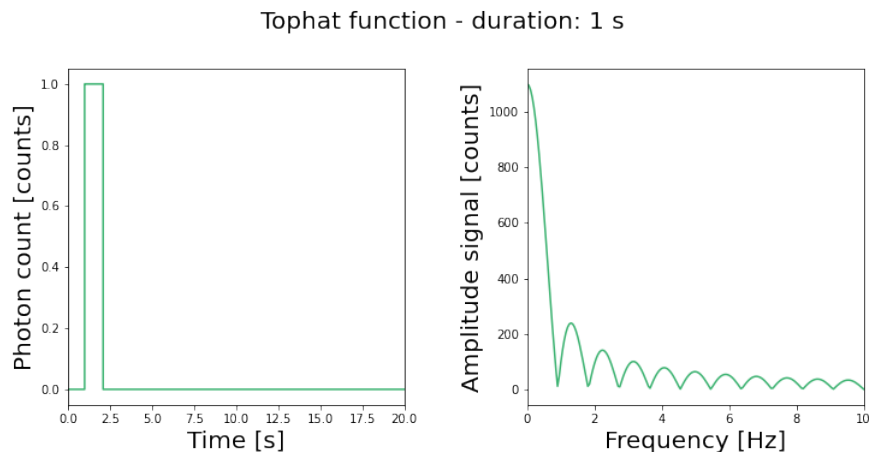
Figure 3.1: *Left:* Top hat function with a duration of 1 s and an amplitude of 1 count. *Right:* The DFT of the top hat function. The horizontal axis is cut off at 10 Hz for better visualisation.

the light curve of the GRB is often binned to have a sufficient amount of counts in one bin, we start with a simple top hat function. Subsequently, we adjust the parameters to understand the effects on the DFT.

We first consider a top hat function with a duration of 1 s and amplitude of 1 count. The DFT is a sinc function, as is shown in Figure 3.1. When we increase the duration of the top hat, to 5 s and 10 s, the amplitude of the DC component of the DFT increases with a factor 5 and 10 respectively, illustrated in Figure 3.2. The subsequent peaks in the DFT increase in amplitude as well. We can conclude that longer signals introduce more power in the lower frequencies. The amplitude spectrum of the DFT displays how strong certain frequencies of the sine and cosine waves are present in the signal. When the signal is stretched, smaller frequency waves are needed to construct the top hat, which in the limit of "infinite stretching" (i.e. a constant signal) only leaves the DC component.

The same exercise can be done for the amplitude. In Figure 3.3, the magnitude of the top hat function is respectively increased with a factor 5 and 10. One can see how the magnitude of the DFT evolves likewise. An amplitude scaling in the time domain corresponds to an amplitude scaling in the frequency domain. Since there is no change in the relative photon arrival times, the frequencies of the DFT stay the same. The same argument explains why there appears to be no difference in the amplitude spectrum of the DFT when the top hat function is shifted in time. This only introduces a phase shift in the sine and cosine waves, but does not alter the frequency or amplitude spectrum.

Next, we can consider double top hat functions. Immediately, it is clear that this increases the complexity extensively. In Figure 3.4, two identical top hats are shown. The
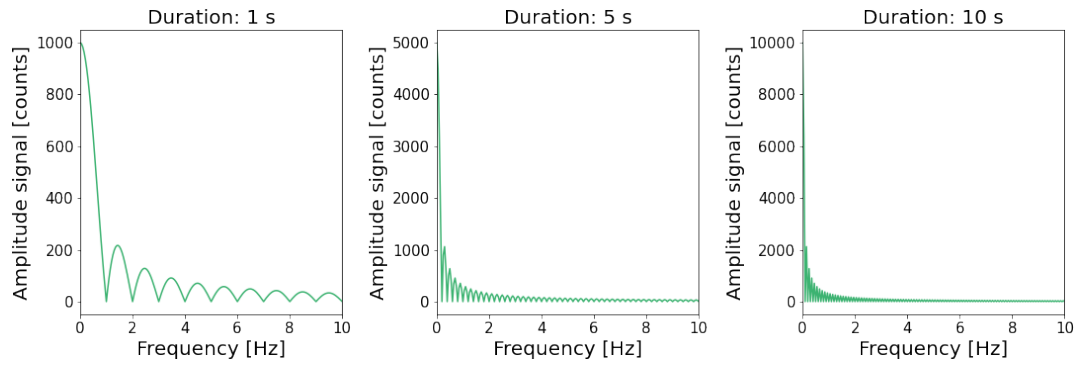
Figure 3.2: *Left:* DFT of top hat function with a duration of 1 s. *Center:* DFT of top hat function with a duration of 5 s. *Right:* DFT of top hat function with a duration of 10 s.
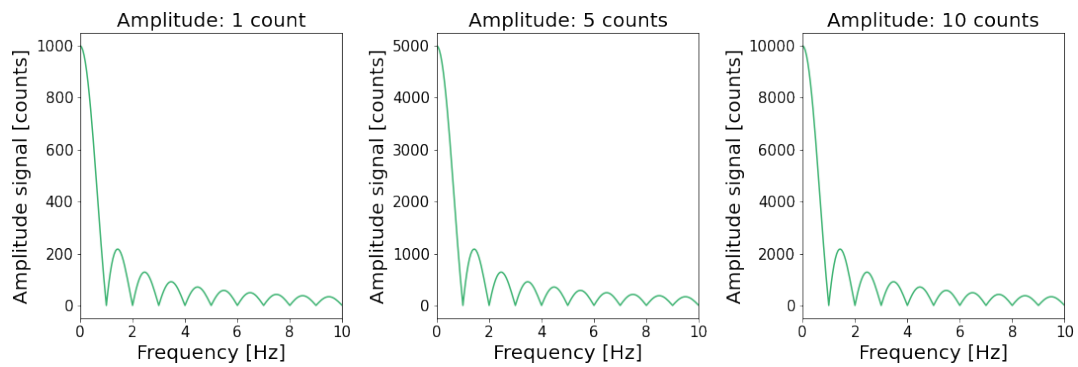

Figure 3.3: *Left:* DFT of top hat function with amplitude of 1 count. *Center:* DFT of top hat function with amplitude of 5 counts. *Right:* DFT of top hat function with amplitude of 10 s.
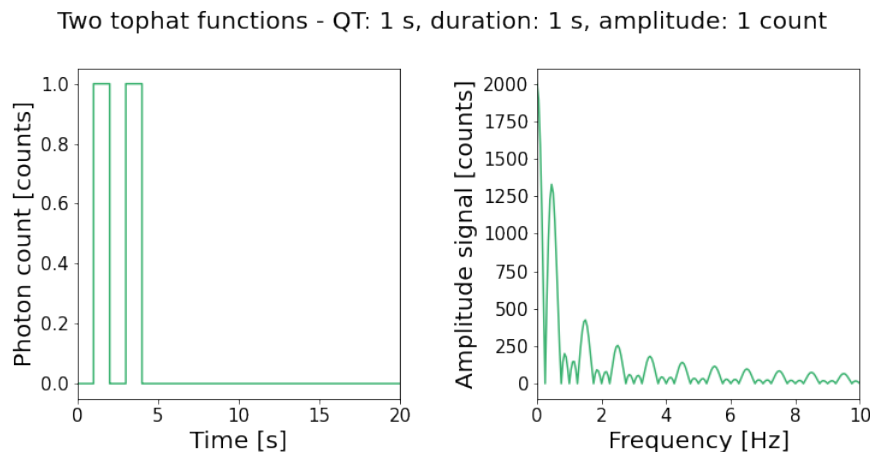
Two tophat functions - QT: 1 s, duration: 1 s, amplitude: 1 count

Figure 3.4: *Left:* Double top hat function. Each pulse has a duration of 1 s and an amplitude of 1 count. The quiescent time lasts 1 s. *Right:* The DFT of the signal.

time between them, called the quiescent time (QT), lasts 1 s. In the DFT, additional peaks appear and the overall amplitude increases. The second pulse is constructed by (co)sine waves which differ by a phase with the original waves, and their summation may not be trivial. The complexity of the signal enhances when parameters as duration and quiescent time are altered, as is illustrated in Figure 3.5. Generally, we find that the power in the lower frequencies again increases, since, if the entire signal would be fitted with one (co)sine wave, the frequency of the wave is lower.

A real GRB signal is an irregular sequence of many bins with various amplitudes. It is not surprising that the DFT will appear very complex. An example is shown in the left panel of Figure 3.6 with the DFT in the middle panel. A signal with an arbitrary time evolution is generated. The resulting DFT does not provide any hints about the time structures that lie at its origin. Since the short time variability within the precursor and prompt emission (which could be represented in this example by the short and long structures in Figure 3.6) is often smaller than the quiescent time, it is expected that the low frequencies correspond to the latter and the higher frequencies might contain features of the former. Simply looking at this example rejects this hypothesis. It is impossible to assign certain peaks in the DFT to features in the time structure.

At last, we notice an important aspect in the calculation of the DFT. We should make sure that the signal is not stretched out over the entire time interval. We calculated the DFT of the theoretical light curve for the time interval [14 s, 29 s], i.e. the time interval of the burst. One can see the result in the right panel of Figure 3.6. The curve contains the global features, but has lost the details and is less smooth. The difference between the middle panel and the right panel is due to the zeros at both sides of the burst. We say that the light curve in the left panel is *zeropadded*. There are two reasons why it is interesting to zeropad the signal. First, the algorithm used to calculate the
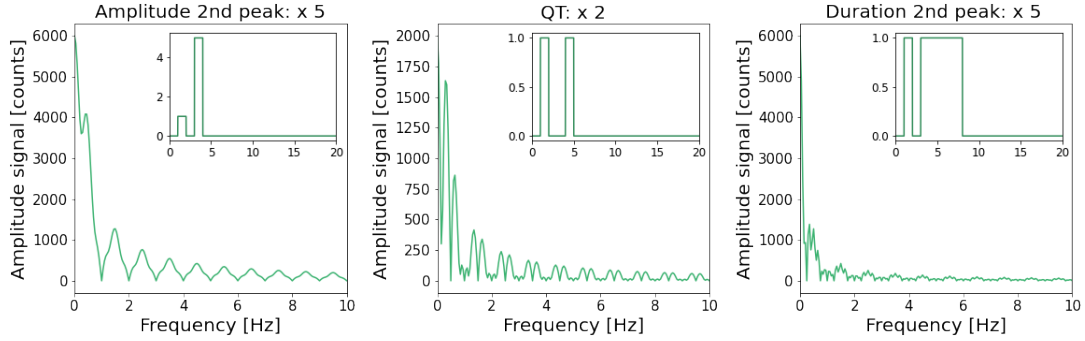
Figure 3.5: *Left:* The DFT of two top hat functions with a QT of 1 s, duration of 1 s and an amplitude of respectively 1 count and 5 counts. *Center:* The DFT of two top hat functions with a QT which is twice as long as in the reference function in 3.4, durations of 1 s and amplitudes of 1 count. *Right:* The DFT of two top hat functions with a QT of 1 s, a duration of respectively 1 s and 5 s and amplitudes of 1 count. The inset panels show the corresponding functions in time domain.
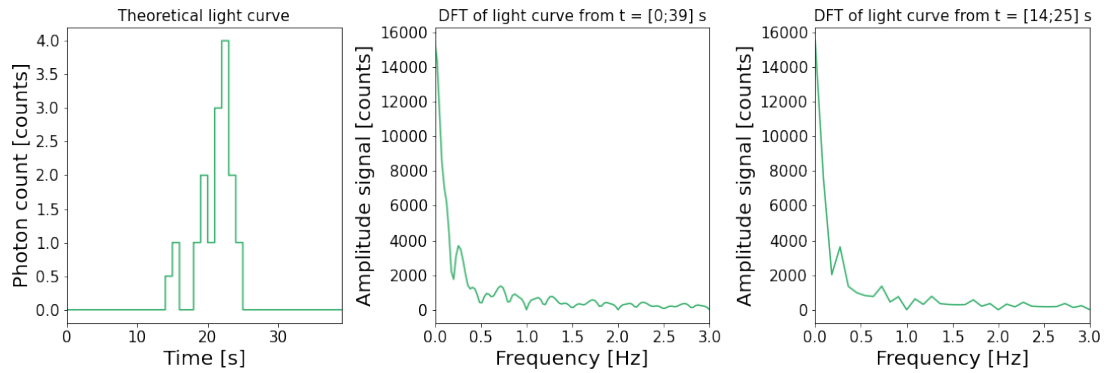
Figure 3.6: *Left:* Light curve of a theoretical GRB. *Center:* DFT of the light curve. We transform the entire time interval, t = [0, 39] s. *Right:* DFT of the light curve. We only transform the time interval t = [14, 25] s.

DFT, the Fast Fourier Transform (FFT), is much faster for input arrays with length equal to a power of two. Adding zeros to the signal until it is sufficiently long, will decrease the computational time of the process in a great extent, but does not add any information to the signal. Secondly, by extending the length of the time array N, we decrease the bin width Δf of the DFT, since $\Delta f \sim 1/N$. That means that we add extra points between the original ones, although without any extra information, and the DFT becomes smoother.

Chapter 4

Analysis of GRB Data

In this chapter, we apply the mathematical toolbox of Chapter 3 to arrive at the average PDS for a certain sample of GRBs. We make use of the time-tagged event (TTE) data of the Fermi Gamma-Ray Space Telescope, which is introduced in Section 4.1, together with a short discussion about its observation mode and possible sources of background photons. Next, in Section 4.2, the entire procedure we followed to calculate the PDS for an individual GRB, is outlined. We start from the TTE data, which are single photon counts, and describe the process of redshift correction, background subtraction and normalisation before calculating the PDS. In Section 4.3, we build further on the individual PDS to infer the average PDS of the entire sample of GRBs. We discuss how we can extract properties of the power-law behaviour of the spectrum, and what the difficulties are in our approaches.

4.1 Fermi Gamma-Ray Space Telescope

The Fermi Gamma-Ray Space Telescope, Fermi in short, is named after Enrico Fermi, Nobel Prize winner in Physics of 1938 for his work in artificial radioactivity and known from e.g. the Fermi acceleration principle, the Fermi-Dirac statistics and the Fermi interaction [73]. The telescope was launched on June 11, 2008, and orbits Earth at a height of ~ 565 km. It contains two instruments, the Gamma-Ray Burst Monitor (GBM) and the Large Area Telescope (LAT). They are shown in Figure 4.1 with their subdetectors. Most of the GRBs are observed by GBM, which detects gamma-rays with energies between 8 keV and 40 MeV within a field-of-view (FOV) of ~ 9.5 sr ($\sim 75\%$ of the full sky). LAT augments the performance of GBM by high-energy observations in the range of 20 MeV to 300 GeV and has a FOV of 2.4 sr ($\sim 19\%$ of the full sky). LAT observes approximately 18 GRBs per year, while GBM sees around 240 GRBs in the same time span. Fermi allows for a study of the gamma-ray emission over an unprecedented range of energy with increased sensitivity. The possibility to detect over seven decades in energy makes Fermi pioneer in observations at high energies by LAT, but bridges also towards observations at low energies by GBM [19, 33, 74, 75].

Figure 4.1: Illustration of the Fermi Gamma-Ray Space Telescope, with its two instruments: the Large Area Telescope (LAT) and the Gamma-Ray Burst Monitor (GBM) and their subdetectors [18].

Fermi's primary instrument is LAT, which is a pair-production telescope, converting high-energy gamma-rays into electron-positron pairs. The telescope is constructed as a 4x4 structure, with 16 identical towers, each containing a tracker and a calorimeter. The entire telescope is covered in a "shield" which is the anti-coincidence detector (ACD). This is used to identify cosmic rays, which hit the telescope continuously and are made up of the same particles that are created by the gamma-rays in the detector. Therefore, when the ACD detects charged particles, it produces a light flash and informs the Data Acquisition System (DAQ) to reject the signal. Since gamma-rays do not carry any charge, they can pass through the shield freely. The ACD removes the charged-particle background with an efficiency of more than 99%.

When a gamma-ray falls into LAT, propagating through the ACD, it interacts with one of the 16 tungsten sheets in the tracker. Here, the gamma-ray is triggered to produce an electron-positron pair. The tracks of the charged particles are used to determine the arrival direction of the gamma-ray. Additionally, their energy is measured in the calorimeter, which can be used to estimate the energy of the original photon. Based on the arrival direction, gamma-rays originating from Earth's atmosphere can be removed as well. Finally, all information is collected by the DAQ, which makes the first distinction between background and signal and selects the signals that should be saved [33, 75, 76].

The complementary GBM instrument is mainly used to detect and locate the observed GRBs. It contains two types of scintillation detectors: 12 sodium iodide (NaI) detectors, sensitive to hard X-rays and low-energetic gamma-rays with energies from 8 keV to 1 MeV, and 2 bismuth germanate (BGO) detectors, sensitive from 200 keV to 40 MeV. The NaI detectors are placed in groups of three at different corners of the spacecraft, while one BGO detector is placed at each side. As such, Fermi observes the entire sky, not occulted by Earth. This is important to detect as much GRBs as possible, since they occur unpredictably and everywhere in the Universe. When an X-ray or gamma-ray enters one of the NaI detectors, it interacts with the sodium iodide material through the photo-electric effect. The decay of excited electrons produces light, which is captured by the connected photomultipliers. Via Pulse Height Analysis (PHA), the energy of the photon is determined [74, 77].

The various NaI and BGO detectors face different directions. The detectors oriented towards a GRB will capture more photons than the ones at the other side of the space-craft. The GBM monitors the counts in each of the detectors and signals a trigger when the counts in two or more detectors exceed a certain threshold value. Requiring that multiple detectors trigger, reduces the number of false counts by non-astrophysical phenomena or statistical fluctuations. By combining the data of various detectors, the location of a burst is determined. A similar process is pursued in the BGO detectors, which will catch more energetic photons. When GBM signals a particular bright GRB, i.e. when the flux exceeds a certain threshold value, an autonomous repoint request (ARR) is sent to the spacecraft flight software. It can be decided to point LAT towards the burst for a longer period of time [19, 74, 76, 78]. In the normal operation mode, the spacecraft slowly changes direction to let LAT scan the entire sky every two orbits (~ 3 hours). This is called the 'sky-survey' mode.

Background Sources

In the sky-survey mode, Fermi slowly but continuously changes direction. When an ARR is issued, the spacecraft repoints soon after the trigger time, which is the most important observation time (i.e. during the burst). This results in variable background rates, which depend on the energy and the orientation of the background sources w.r.t. the individual NaI and BGO detectors [77]. Two light curves of GRBs for which the variability in the background is apparent, are shown in Figure 4.2 [78]. The background in the individual detectors is composed of different sources, which are discussed below.

Cosmic rays. As mentioned before, background photons can originate from the direct interaction between the satellite and cosmic rays, which still pass through the highly efficient ACD cover. This gives however only a minor contribution to the background for $E > 150$ keV [74]. The dominant background source in this energy range is the indirect interaction between cosmic rays and the spacecraft. Fermi is located in a low-Earth orbit and completes its trajectory in 96 minutes. That means that the satellite is still shielded by the magnetic field of Earth, protecting it from low-energy cosmic rays.
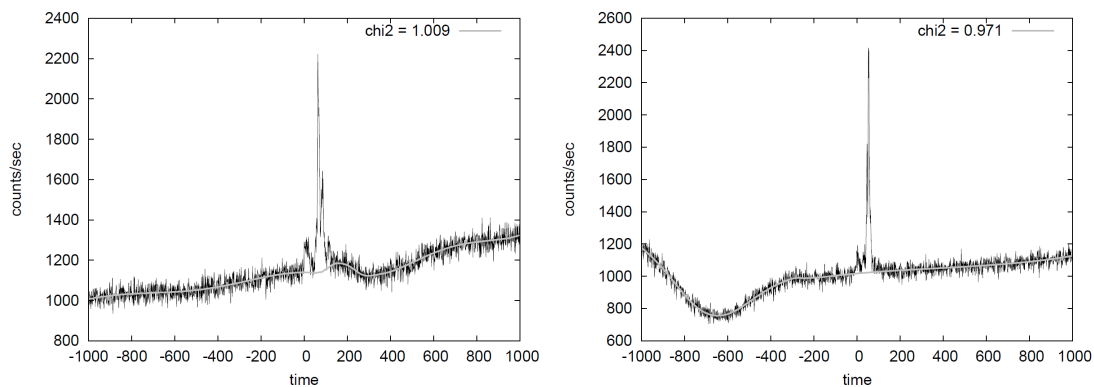
Figure 4.2: Two examples (GRB 090618353 and GRB 090828099) of light curves of GRBs to demonstrate the variable background present in the data. The grey line illustrates the background fit by Szécsi et al. (2013), from which the figures are taken [78].

Nonetheless, this adds a new source of background. When cosmic rays interact with the highest layers of Earth's atmosphere, mainly through pion decay, they produce a cascade of secondary particles. Gamma-rays and X-rays are created, partly being emitted back into space. A continuous diffuse signal develops within the typical energy band of GBM, but since this signal is smoothly changing due to the movement of the satellite, it can be modelled and the secondary gamma-rays are recognised as background [74, 77].

Lightning. Lightning in Earth's atmosphere is believed to be a source of terrestrial gamma-ray flashes. The electric field generated in the thunderstorms can accelerate electrons up to energies of the order of several tens of MeV. When such an energetic electron encounters a nucleus, it is deflected and decelerated, emitting Bremsstrahlung. The emission of one electron is insignificant, but the accumulated effect of many electrons can produce short flashes of gamma-rays, with a duration of the order of micro- up to milliseconds. The duration and the direction of the gamma-rays reveal that these are false signals of GRBs and thus can be identified as background. Lighting might also produce secondary particles which get trapped in the magnetic field lines, form a beam and travel large distances. It is possible that the beam meets the satellite far away from the thundercloud. They produce a signal which resembles gamma-rays from lightning, but appear not necessarily close to a thunderstorm, making it more difficult to recognise the false signal [18, 79].

South-Atlantic Anomaly. Earth's magnetic field contains two regions, called the Van Allen radiation belts [80], in which the charged particles, originating from e.g. solar flares, are trapped. The inner Van Allen belt lies at an altitude of 1000 km and thus safely above the orbit of Fermi. However, in a region above the South Atlantic, called the South-Atlantic Anomaly (SAA), Earth's magnetic field is much weaker. This causes the settling of the inner belt at an altitude of ~ 100 km, now intersecting Fermi's orbit. Therefore, the detectors are turned off during the passage through the SAA to

avoid damage, but charged particles can still interact with the spacecraft material. This produces photons which give counts when the detectors are again activated [74, 77].

Solar System. Other sources of gamma-rays in the Solar System are the Sun and the Moon. Similarly to Earth, cosmic rays interact with the lunar surface and produce gamma-rays [81]. The same process happens in the Sun, although the Sun is shielded by a magnetic field, which decreases the interaction rate. The Sun, however, is a source of solar flares, ejecta of charged particles which carry their own magnetic field and contain accelerated particles, producing gamma-rays. Characteristics such as the location of the flare hint that their origin is not 'GRB-like' and distinguish them from GRBs [76, 82].

Galactic and extragalactic sources. A diffuse Galactic gamma-ray emission exists, coming mainly from the galactic plane and centre. It originates from cosmic rays, electrons and positrons interacting with the interstellar gas, or from local particle acceleration sites [83]. Besides that, individual galactic sources contribute to the background rate, such as accreting binary systems or soft-gamma ray repeaters (SGRs), which are highly magnetised neutrons stars (magnetars), emitting pulses of X-rays and γ-rays but in a repeating manner [19, 84]. Extragalactic sources comprise gamma-rays originating from active galactic nuclei or giant magnetar flares [77, 78].

4.2 Individual GRBs

4.2.1 Data Format

In this thesis, we use the TTE data of the NaI detectors of Fermi-GBM. For each GRB trigger, these files contain the observed photon counts with a time resolution of $2.6\,\mu s$ (accurate up to $< 10\,\mu s$). The energy of the photons is stored in 128 bins, of which the bin width increases pseudo-logarithmically with increasing energy. Each photon count has thus a corresponding index between 0 and 127. Before August 2010, the TTE data contained counts starting 30 s before the trigger time and ending 300 s afterwards. After a software update, this time range was extended to 130 s before and 300 s after the trigger time [74].

Apart from the TTE data, Fermi-GBM releases two other types of data files as well, which contain temporal information about the burst from 1000 s before and until 1000 s after the burst. Continuous spectroscopy (CSPEC) files store the energy in the same 128 bins as the TTE files, but use a broader time binning of 4.096 s. Continuous time (CTIME) data use a smaller bin width of 256 ms, but only offer 8 energy bins [74]. We choose to focus on the TTE data only, since these files contain good temporal and spectral information about the bursts. Since we are mainly interested in the properties of the main burst and precursor, rather than of the afterglow, this is sufficient.

As explained in Section 4.1, each burst is observed by multiple detectors simultaneously. The first detector, in which the photon rate exceeds a certain preset threshold value,

defines the trigger time. However, a GRB must trigger at least two of the twelve NaI detectors to be considered as a real signal. We used the data of the two or three subdetectors, pointing closest to GRB, as they generally contain the strongest signals. In a previous analysis by Coppin et al. (2020) [35], the triggered detectors were identified. In GRB analyses, it is convenient to add the photon counts of the different detectors in order to receive a stronger signal. As such, we find the combined spectrum of the GRB, on which the analysis is performed.

Ultimately, the photon counts are binned in time. We choose a bin width of 5 ms, since this gives a sufficiently small time resolution, while conserving enough photon counts in one bin. Note that the light curves of GRBs are often binned according to the Bayesian Block (BB) procedure, developed by J. Scargle for the analysis of the BATSE light curves [85]. This method allows for a variable time binning, based on Bayesian statistics. A transition from one bin to the next bin signals a significant change in the rate. Hence, the method is able to identify emission zones above background consistently. We choose not to use this method in this thesis, since it resamples the data points, which are then no longer independent or Poisson distributed. Having independent and Poisson distributed data points is an important condition to use the formulas to derive the uncertainties on the PDS, which we would like to do. Therefore, this analysis is performed on the raw data of the GRBs with a fixed time binning.

4.2.2 Redshift Correction

After summing the contributions of the different detectors, we want to correct for the redshift z on the observed time and energy values. In this way, we perform the analysis in the reference frame of the source. Especially in view of the averaging process, it is crucial to treat every GRB equally. GRBs are observed at various distances, and the imprint of the redshift on the light curve depends on the distance the photons have traversed. The time interval Δt_o between the photons is stretched, and the energy E_o is reduced (i.e. the light appears more 'red') compared to the original time interval Δt_e or photon energy E_e with a factor $(1 + z)$ or $(1 + z)^{-1}$ respectively:

$$\frac{\lambda_o}{\lambda_e} = \frac{\nu_e}{\nu_o} = \frac{E_e}{E_o} = 1 + z \qquad\qquad \frac{\Delta t_o}{\Delta t_e} = 1 + z, \qquad (4.1)$$

where λ and ν are the wavelength and frequency of the photons, and the index 'o' denotes the observed parameters and 'e' the parameters of the emitted photons at the source. Transforming the light curves to the GRB reference frame thus results in a narrowing of the time bins. Therefore, the redshift correction is performed before the binning of the photon counts to ensure that the time binning is equal (5 ms) for each GRB. Note that the current redshift distribution of observed GRBs has a maximal value of $z = 9.4$ (GRB 090429B) [17]. Most GRBs have redshifts between $z = 0$ and $z = 6$ [33]. Figure 4.3a shows the binned, redshift-corrected light curve of GRB 151027166.
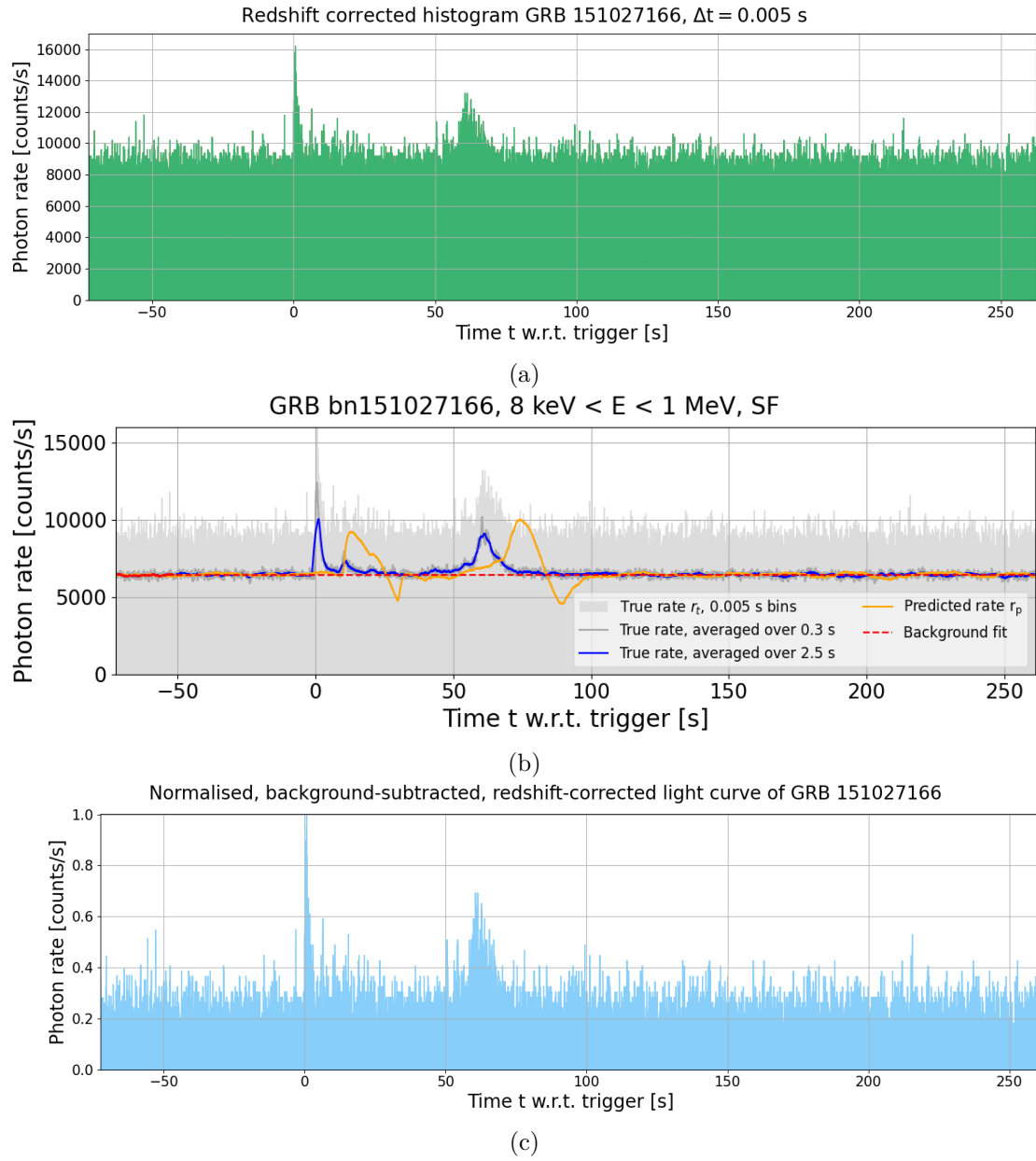
(a)

(b)

(c)

Figure 4.3: (a) Redshift-corrected light curve of GRB 151027166, located at redshift $z = 0.81$. The horizontal axis shows the time w.r.t. the trigger time $t = 0$. The vertical axis gives the photon rate per bin, i.e. the total photon count divided by the bin width. (b) Illustration of the background characterization process, outlined in Section 4.2.3. The light grey histogram shows the redshift-corrected light curve of Figure 4.3a and the dark grey line is the photon rate, averaged over 0.3 s. The blue curve denotes the photon rate $r_{2.5\,s}$, averaged over 2.5 s, and is compared to the predicted rate r_p in yellow to estimate the background rate (red dotted curve). (c) Background-subtracted light curve, normalised by its highest peak.

4.2.3 Background Estimation

The redshift-corrected light curve still contains signal and background. To arrive at a good characterisation of the background rate, we rely on a sequence of steps described in Coppin et al. (2020) [35]. The procedure aims at selecting the time spans in which no increase in gamma-ray emission is seen above background. In other papers, the background rate is often identified by eye. This is however time-consuming for large samples of GRBs and is subjective. A generalised procedure, based on well-defined conditions and criteria, treats all light curves similarly and can be repeated. This results in a consistent background characterisation and allows, by extension, to compare different studies more correctly.

The procedure outlined in Coppin et al. (2020) [35] is founded on an empirical basis; the resulting background rate is close to the one that would be identified by eye. The authors performed their research on TTE data, extended with CTIME data, of Fermi. Since we solely operate with the TTE data in this thesis, our light curves look different. Therefore, we modified the procedure. This was not a trivial process, and mainly proceeded by trial and error. While the original criteria could be interpreted in terms of uncertainty intervals, the new conditions are empirical. In the future, a more in-depth method can be developed. We stress that we pose very strict criteria, since we only want to select regions as background when being 100% certain.

In this section, only our method will be outlined, but the original procedure can be consulted in Appendix B of Coppin et al. (2020) [35]. The main challenge to tag the background rate lies in its variability. As discussed in Section 4.1, the spacecraft continuously changes direction. Background sources move in the line of sight and disappear again. The variable nature of the background induces rises or declines in the photon rate, which are not due to the main burst or afterglow emission. Fortunately, the orbital motion is rather slow and of the order of hours. We can approximate the background rate by a linear interpolation, as long as the time range is not longer than ~ 100 s. No complications are expected, since this is more than three times the average duration of a long burst.

To identify stable regions with an approximate constant photon rate, we compare the predicted rate r_p with the average rate $r_{2.5\,s}$, which is the true rate averaged over a period of 2.5 seconds. The average rate in a point t_0 is computed by considering a symmetric time interval centred on t_0, i.e. $[t_0 - 1.25$ s$, t_0 + 1.25$ s$]$. The predicted rate at time t_0 is estimated by regarding a time interval $[t_0 - 30$ s$, t_0 - 20$ s$]$ and interpolating using a straight line between the end points. The fit is then extrapolated and evaluated at t_0, giving us the value of the predicted rate $r_p(t_0)$ at that moment. To decide whether a point is identified as background or not, it is verified that the average rate and predicted rate do not differ in a large extent, by requiring:

$$r_{2.5\,s}(t_0) < r_p(t_0) + 3 \cdot \sqrt{\frac{|r_p|(t_0)}{2.5\ s}} \ . \tag{4.2}$$
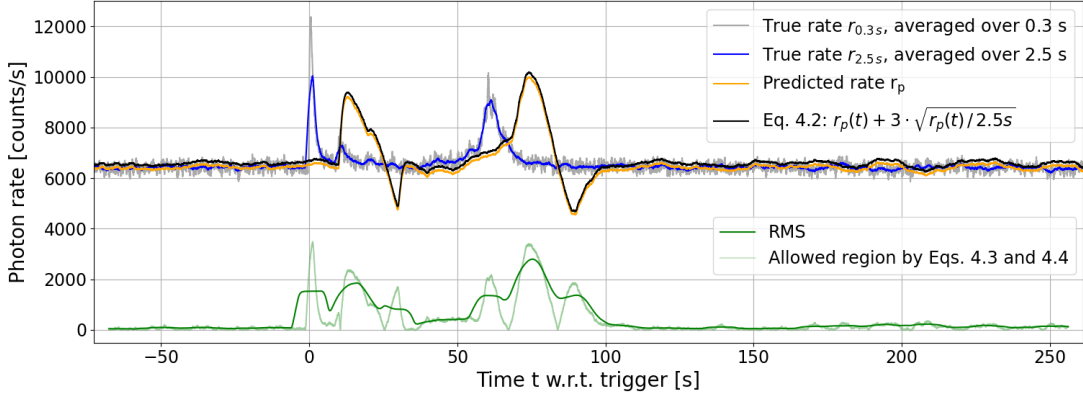
Figure 4.4: Illustration of the conditions used for the background characterisation. The grey line denotes the true rate, averaged over 0.3 s, and the blue line the true rate, averaged over 2.5 s. The yellow line is the predicted rate r_p. The black line gives the upper limit of Eq. 4.2, while the dark green line illustrates the RMS value, which should lie between the boundaries of Eqs. 4.3 and 4.4. See text for more information.

The average rate in a point is thus allowed to exceed the predicted rate by a limited amount. We illustrate this in Figure 4.4 by the black line. If the condition in Eq. 4.2 is fulfilled, the point is seen as background. We proceed 1 s in time and check this again. When we arrive at a point t_s that does not satisfy the condition in Eq. 4.2, we proceed 30 s in time to $t_n = t_s + 30$ s, to jump over the region. The time interval $[t_s - 3$ s, $t_n]$ is subsequently identified as 'non-background'. The three seconds before t_s are included to improve the background fit. At t_n, we check if the RMS of $(r_p - r_{2.5\,s})$, computed over an interval with duration $\Delta t = 10$, symmetric around t_n, satisfies the following equations:

$$\mathrm{RMS}\left[(r_p - r_{2.5\,s})(\Delta t)\right] > (|r_p - r_{2.5\,s}|)(t_n) - 1.4 \cdot \sqrt{\frac{(|r_p - r_{2.5\,s}|)(t_n)}{\Delta t}} \qquad (4.3)$$

and

$$\mathrm{RMS}\left[(r_p - r_{2.5\,s})(\Delta t)\right] < (|r_p - r_{2.5\,s}|)(t_n) + 1.4 \cdot \sqrt{\frac{(|r_p - r_{2.5\,s}|)(t_n)}{\Delta t}} \qquad (4.4)$$

Again, this condition verifies whether the RMS value is included in a small region around $(r_p - r_{2.5\,s})$ in the corresponding point. Note that the RMS is calculated over a time span of 10 seconds, while the other terms are computed in one specific point. In Figure 4.4, it can be observed that the allowed range is incredibly small, so the conditions are often not satisfied. Nevertheless, they are crucial for the background fits of some light curves. When the above conditions are not satisfied, the point is identified as non-background, and we proceed four seconds, after which the conditions in Eq. 4.3 and Eq. 4.4 are again

checked. If, however, the above conditions are true, we include one last criterium. In t_n, the predicted rate should be smaller than the averaged rate, or:

$$r_p\left(t_n\right) < r_{2.5\,s}\left(t_n\right). \tag{4.5}$$

If this is true, t_n is identified as background, and we advance 1 s and repeat the procedure outlined above. If Eq. 4.5 is not satisfied, t_n is labelled as non-background, and we proceed 1 s to check Eqs. 4.3 and 4.4 again. Note that we adopt the objective that everything not identified as signal is background, meaning that everything that is not background, might be signal, but as well can be a statistical fluctuation.

To construct the background fit, we put the background rate equal to the averaged rate $r_{2.5\,s}$ in the background points. In the regions between the background points, we linearly interpolate. This is illustrated in Figure 4.3b. As such, we arrive at a stable estimation of the background for most GRBs. The background rate is subtracted from the true photon rate, i.e. from the grey histogram in Figure 4.3b. In Appendix A, the GRBs are assembled for which the procedure did not produce a perfect background fit. This can be due to a sudden drop or decline in the rate, or intermediate points that are recognized as background while they are clearly part of the burst. When it was undeniable that the process was mistaken, we manually adjusted the fit and determined the background by eye.

4.2.4   Normalisation

Subsequently, the background-subtracted light curves are normalised, such that they all contribute to the average PDS of the sample equally. If not, the features of the brightest bursts will dominate the averaged spectrum. Two types of normalisation are prevalent in the GRB field: normalisation by highest peak and normalisation by total photon count. We choose the former, since that allows us to compare with other research. The result is shown in Figure 4.3c.

4.2.5   PDS Calculation

Finally, the DFT is calculated. This is done numerically by the Fast Fourier Transform (FFT). Since this algorithm works faster when the length of the dataset equals a power of two, we zeropad the light curves up to the closest power of two that encompasses all bursts (usually 2^{33}). We use the 'backward' normalisation, so no extra scaling is introduced when calculating the DFT, as explained in Section 3.1. The PDS is defined as the square of the amplitude spectrum of the DFT. We normalise the PDS according to the Leahy normalisation [86], i.e.

$$P_j = \frac{2}{N}\left|F_j\right|^2, \tag{4.6}$$

where N is the sum of the photon counts in the bins of the time spectrum and F_j are the Fourier amplitudes in the different frequency bins, $j = 0, ..., N/2$. This normalisation
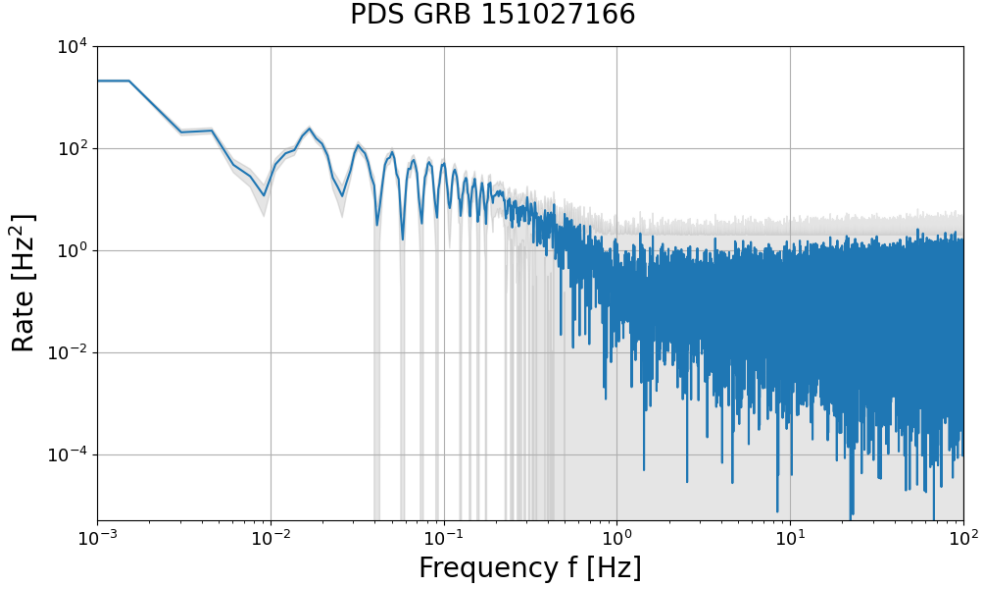
Figure 4.5: Power-density spectrum for GRB 151027166. The grey band shows the 1σ uncertainty band, which appears asymmetric due to the log-log scale.

ensures that we can adopt the formulas for the statistical uncertainties of Guidorzi (2011) [87]. The PDS for GRB 151027166, with uncertainties, is shown in Figure 4.5. Note that the PDS at the lowest frequencies is dominated by the sinc-function, since our time spectrum in temporal space can be approximated by a top hat function for large time windows. For $f \gtrsim 1$ Hz, it is dominated by noise. In between, the features due to the time variability of the burst appear.

Statistical uncertainties. As already mentioned before, to calculate the uncertainties on the individual PDS, we consider the discussion of Guidorzi (2011) [87]. This paper addresses the problem of correctly estimating the uncertainties on the PDS of single-sampled light curves, as in the case of GRBs, for Gaussian and Poisson noise. The general idea is that the observed time series is one sample of the true time series, which is described by a deterministic function but affected by noise. Formulas for the variance on the PDS are derived in the paper. However, for short and transient phenomena as GRBs, only one observed light curve is accessible. The deterministic function is not known a priori. In this case, the equations for the uncertainties on the PDS are approximated by

$$\sigma(P_j) = \begin{cases} 2\sqrt{P_j + 1} & (j < N/2), \\ 2\sqrt{2}\sqrt{P_j + 1} & (j = N/2). \end{cases} \tag{4.7}$$

For an in-depth derivation, we refer to the paper [87]. We note that the TTE data include systematic uncertainties on the time as well, but the transformation of these errors to Fourier space falls outside the scope of this thesis.

4.3 Multiple GRBs

Now, we discuss the procedure to construct the average power-density spectrum. We apply this to the entire sample of GRBs in this section, and repeat this for different subsamples of GRBs in Chapter 5: samples based on the brightness of the peak, photon energy, duration and emission periods.

4.3.1 Average PDS Calculation

The averaging of different individual power-density spectra is not trivial. It includes the strong assumption that the different time spectra of GRBs are the realisations of one, common stochastic process. In other words, one unique process gives rise to the different temporal characteristics that GRBs display. The average PDS exhibits the properties of this general process. Since this is exactly our hypothesis by searching for the Kolmogorov slope and turbulence, which may lie at the origin of the features apparent in GRBs, the averaging process is not an issue. The average power density is calculated per frequency bin and its uncertainties are propagated to the mean value, i.e.

$$\langle \, \mathrm{PDS}\,[f] \, \rangle = \sum_{j=0}^{N-1} \frac{\mathrm{PDS_j}\,[f]}{N} \, , \tag{4.8}$$

$$\sigma(\langle \, \mathrm{PDS}\,[f]\, \rangle) = \sum_{j=0}^{N-1} \frac{1}{N} \sqrt{(\sigma_j\,[f])^2} \, , \tag{4.9}$$

where the sum goes over the individual power-density spectra, and N is the total number of GRBs in the sample. Figure 4.6 shows the individual power-density spectra of the 156 GRBs in our sample. The colour gradient refers to the duration of the bursts. The darkest colour is connected with the longest burst. We do not see any special feature linked to the duration of the burst. We average over the different spectra and arrive at the average PDS in Figure 4.7, with its 1σ error band.

4.3.2 Power-Law Fit

Ultimately, we want to inspect the power-law behaviour of the average power-density spectrum in Figure 4.7. In log-log space, it should be able to approximate the spectrum by a straight line, as discussed in Section 2.7. The range in which the power-law features are present, is limited by the maximal and minimal time variability of the light curve. The maximal time variability is set by the duration of the longest burst. Looking at the bursts with a time window longer than the longest burst, will not reveal any temporal information about that burst, i.e. causing the spectrum to break away from the power-law fit. One can compare it to having an instrument with too low resolution to detect the variability of a parameter. Thus, the frequency that corresponds to the duration of the longest burst will define the cut-off frequency at the lower-frequency end. Similarly, the higher-frequency cut-off is set by the smallest bin width of the time spectrum. In
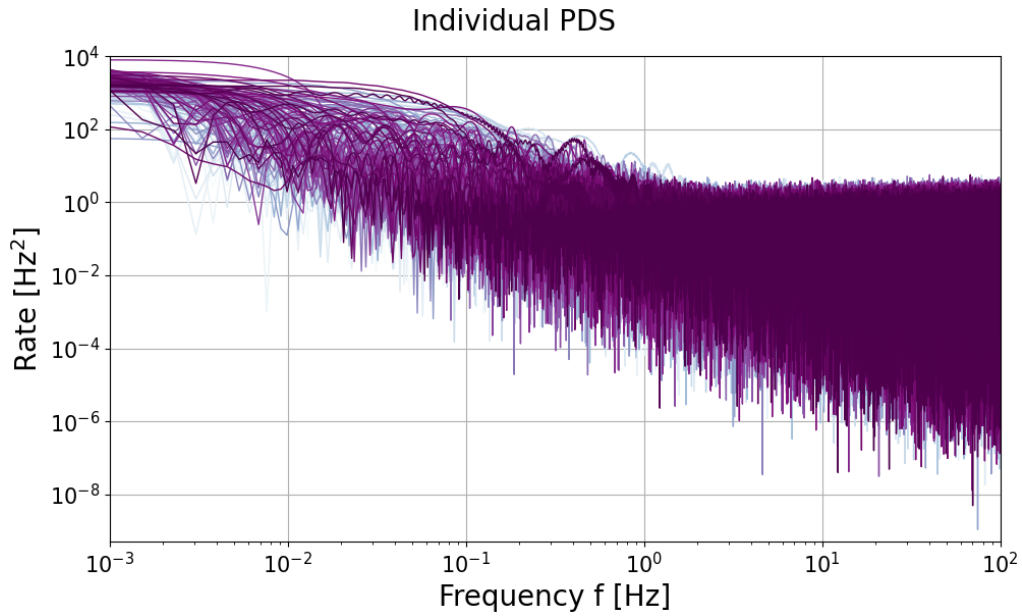
Figure 4.6: The different power-density spectra of all 156 GRBs in our sample. The colour is connected to the duration of the burst, where the darkest colour shows the longest burst and vice versa. The error bands are not shown in this plot for clarity.
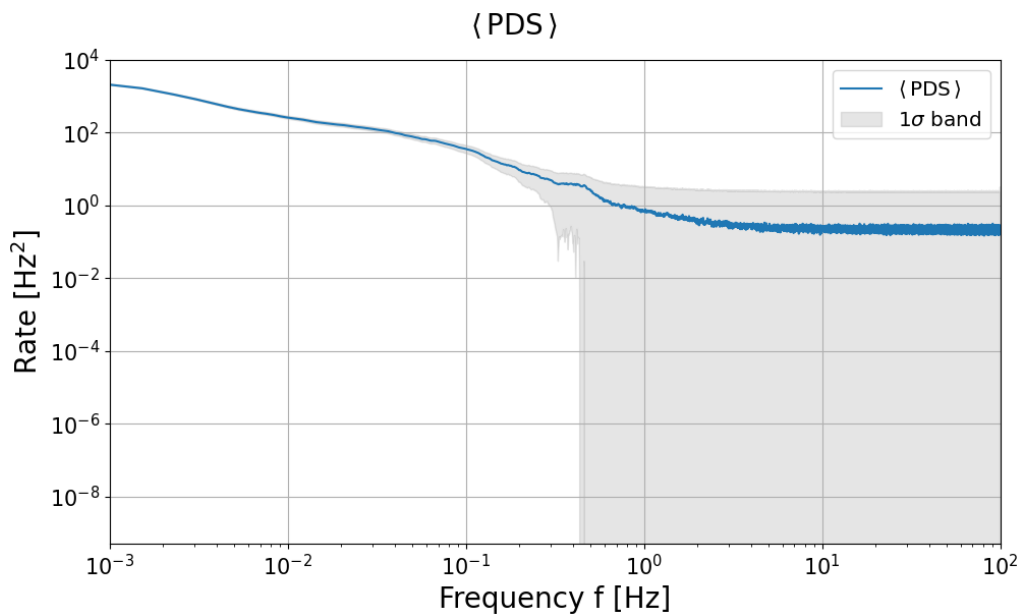

Figure 4.7: The average power-density spectrum of the power-density spectra of the 156 GRBs in our sample, shown in Figure 4.6. The grey band illustrates the 1σ error band, which appears asymmetric due to the log-log scale of the plot.

Table 4.1: Fitting parameters for the power-law fits, $r = a \cdot f^b$, in Figures 4.8 and 4.11 to the average PDS of the entire sample of 156 GRBs. N denotes the number of GRBs involved. The parameter a corresponds to the value for the offset of the straight line, and b to the slope. They carry their statistical uncertainties (σ_a, σ_b) and, if known, systematic uncertainties ($\sigma_{a,r}$, $\sigma_{b,r}$). We provide the goodness-of-fit, χ^2, normalised by the number of degrees of freedom (dof), and the fitting range.

N	$a \pm \sigma_a \pm \sigma_{a,r}$ [Hz]	$b \pm \sigma_b \pm \sigma_{b,r}$ [Hz]	χ^2/dof	$[f_{b,\,low},\, f_{b,\,high}]$
156	0.7669 ± 0.0427	-1.6043 ± 0.0248	2.51	[0.05, 1.00] Hz
156	$0.7673 \pm 0.0462 \pm 0.2270$	$-1.6181 \pm 0.0367 \pm 0.4209$	1.48	[0.10, 4.50] Hz

this case, the bin width is constant and equal to 5 ms. This implies that the spectrum is expected to break away from the power-law around 100 Hz[1]. However, in Figure 4.7, we notice that the spectrum flattens for $f \gtrsim 1$ Hz, which is due to the noise. This means that the spectrum becomes noise dominated on sub-second scales. Since this distorts the power-law fit, as the noise spectrum stays rather constant, we choose to limit the range at the high frequency end to 1 Hz. The longest burst of this sample has an observed T90 value of 828.672 s or 460.3733 s, when redshift corrected. This thus causes a break at 0.0022 Hz. We expect power-law features in the interval [0.002, 1.00] Hz.

The average PDS is modelled by a power-law function of the form

$$r = a \cdot f^b \Leftrightarrow \log(r) = b \cdot \log(f) + \log(a), \tag{4.10}$$

where r corresponds to the rate of the average PDS, f to the frequency, b to the power-law index or the slope of the straight line and $\log(a)$ to the offset value of the fit function. We perform the power-law fit in linear space, and then transform everything to log-log space. The power-law fit is numerically less stable than a linear fit in log-log space, but allows for a proper treatment of the uncertainties. A linear fit in log-log space would force us to give less weight to the lower-frequency end.

Previous studies fitted the power-law by eye [58, 59] or used a broken power-law, where the breaking frequency was left to vary [61, 62]. Mostly, the break occurred between 0.01 Hz and 0.1 Hz. We are interested in the slope of the second part of the broken power-law. To be able to compare with those studies and other papers, we choose to fit our power-law function in the range from 0.05 Hz to 1.00 Hz. The upper limit should protect the fit from being affected by the noise. This is applied to the entire sample of 156 bursts in Figure 4.8, for which the fit parameters are given in the first row of Table 4.1. We arrive at a slope of $b = -1.6043 \pm 0.0248$ Hz.

At first instance, we evaluate the fit, which has a $\chi^2/\mathrm{dof} = 2.51$, as decent, but the fitting range is not physically motivated and thus difficult to advocate. In addition,

---

[1]The Nyquist theorem states that one cannot probe to a higher frequency than half the sampling frequency, $f \leq f_{Nyquist} = f_s/2 = 1/(2T_s)$, without loss of information [72]. Here, $T_s = 5$ ms.
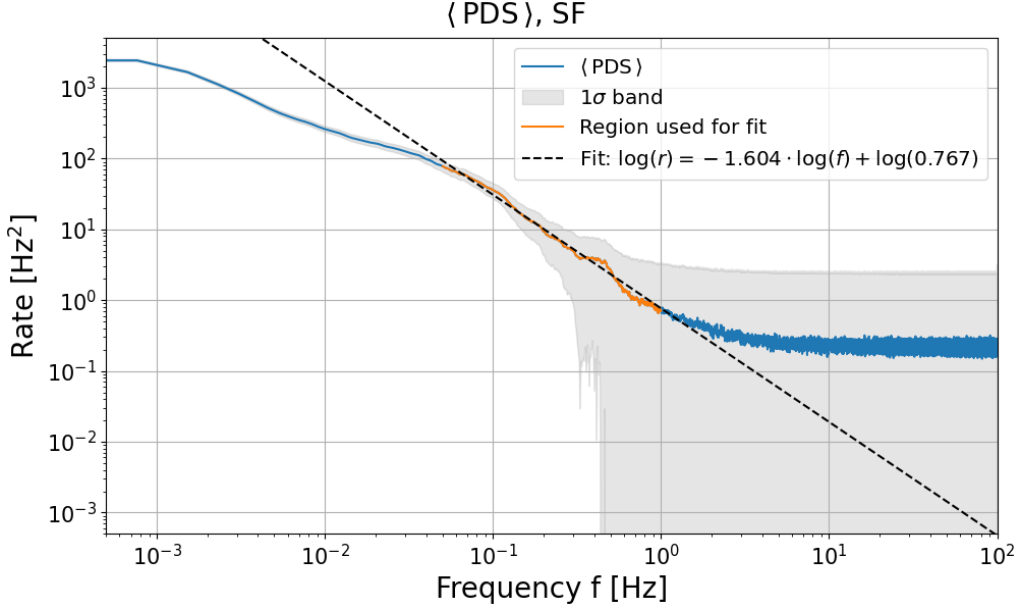
Figure 4.8: The average PDS of the 156 GRBs in our sample, with its 1σ error band. The orange region illustrates the points used for the fit $r = a \cdot f^b$ between 0.05 Hz and 1.00 Hz. The best fit is shown as black dotted line and has fit parameters $a = 0.7669 \pm 0.0427$ Hz and $b = -1.6043 \pm 0.0248$ Hz. More parameters are listed in Table 4.1.

every GRB sample and corresponding average PDS is different. The power-law features and the noise features will appear at varying frequencies. We argue that, within the interval [0.002 Hz, 1.00 Hz], the fitting range can still be extended to lower frequencies. However, this strongly affects the slope of the power-law. Since this is the parameter we are interested in, we prefer robust fitting intervals which arise from physical parameters. As a first attempt, we developed a method, based on the goodness of the fit and the χ^2-statistic, outlined below.

Optimal fit range. The optimal fit range is found by a minimal χ^2-method. As mentioned before, the longest burst and the smallest bin width define the range in which we expect the bursts to exhibit power-law features, and thus at which we expect the average PDS to break away from the fit. We define them as the low-frequency break $f_{b,\,low}$ and high-frequency break $f_{b,\,high}$ respectively. Inspired by the results of the fitting between 0.05 Hz and 1.00 Hz of all GRB subsamples, we see that the power-law appears between 0.01 Hz and 5.00 Hz. This is a very broad range, but is meant to include most of the power-law behaviour. Therefore, we let $f_{b,\,low}$ and $f_{b,\,high}$ take values between 0.01 Hz and 5.00 Hz, and compute for each combination the χ^2-statistic, defined as:

$$\chi^2 = \sum_{i=1}^{n} \frac{(r_{o,\,i} - r_{fit,\,i})^2}{\sigma_i^2}, \tag{4.11}$$

where r_o denotes the observed values of the rate, with uncertainties σ, and r_{fit} the expected values of the rate by the best fit. By varying $f_{b,low}$ and $f_{b,high}$, we arrive at a 2D colour map of $(f_{b,low}, f_{b,high})$ and the corresponding χ^2 value, as shown in Figure 4.9a. Our goal is to arrive at the broadest fitting interval, while still retaining a good fit. A good fit is characterised by $\chi^2/\text{dof} \sim 1$, but we allow some scatter around this value by considering $0.5 \leq \chi^2 \leq 1.5$. We can plot these χ^2-values as a function of $f_{b,low}$ and $f_{b,high}$, of which the plots are shown in Figure 4.9b. Then we search for the combination of the cut-off frequencies, giving us the widest range. In this case, this happens for $[f_{b,low}, f_{b,high}] = [0.10 \text{ Hz}, 4.50 \text{ Hz}]$ with $\chi^2 = 1.49$. In Figure 4.11, we show the best fit for the average PDS of the sample of 156 GRBs in this fitting range. The corresponding values for the fit parameters are listed in Table 4.1.
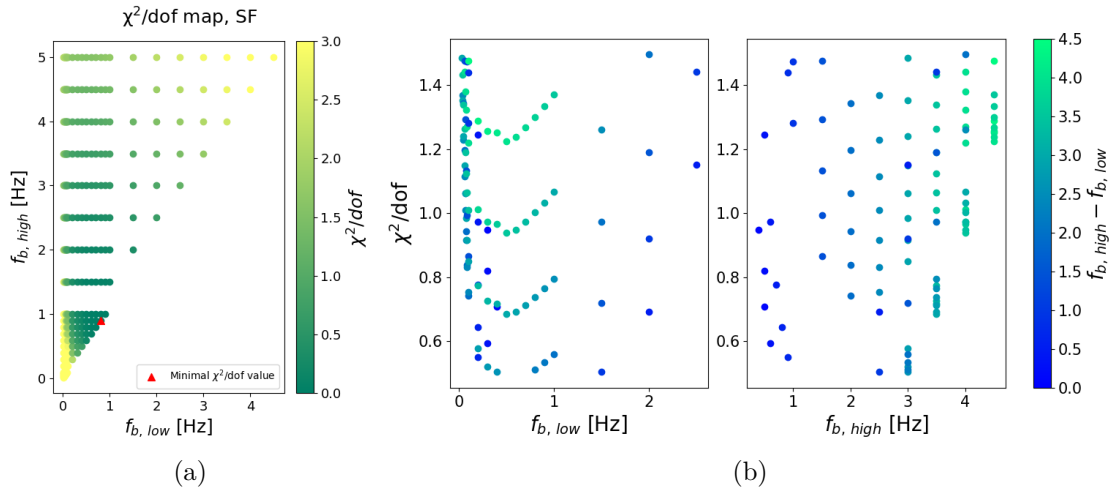

Figure 4.9: (a) 2D colour map of $f_{b,low}$ in function of $f_{b,high}$, with the corresponding χ^2 value denoted in colour. The red triangle pinpoints the minimal χ^2 value. (b) χ^2/dof w.r.t. $f_{b,low}$ and $f_{b,high}$ respectively. The colours now illustrate the length of the fitting interval.

The advantage of this method is that the fit searches the optimal range in which the spectrum is best approximated by a power-law. However, as can be seen in Figure 4.11, some noise is included, which flattens the curve. A solution for this is to lower the upper limit to 1 Hz, as stated before. But for some GRB samples, e.g. the brightest bursts, the noise only appears at 3 or 4 Hz. By limiting $f_{b,high}$ to 1 Hz, one loses important information from higher frequencies, i.e. smaller time scales. Therefore, we continue with an upper limit of 5 Hz. No time was left to investigate the power-law fits for lower upper limits, but this should be persuaded in the future.

Another advantage is that we are able to derive a systematic error for the fit parameters. Different ranges are possible within our constraint of $0.5 \leq \chi^2 \leq 1.5$. Above, we chose to continue with the broadest interval, but each range corresponds to a different set of
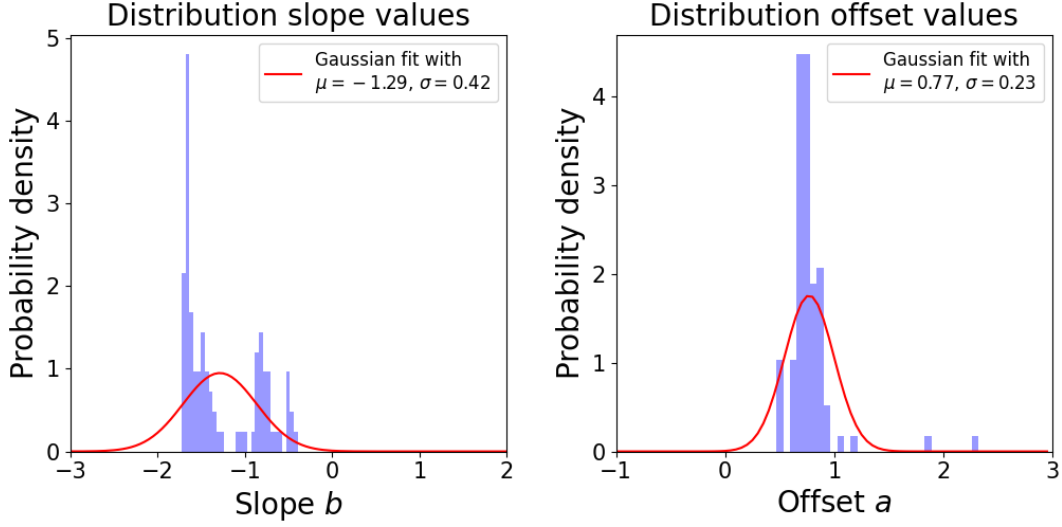
Figure 4.10: *Left*: Distribution of the slope values for different power-law fits with $0.5 \leq \chi^2 \leq 1.5$, which can be fitted with a Gaussian curve with $\mu = -1.29$, $\sigma = 0.42$. *Right:* Distribution of the offset values for different fits with $0.5 \leq \chi^2 \leq 1.5$, which can be fitted with a Gaussian curve with $\mu = -1.77$, $\sigma = 0.23$.

fit parameters. The ultimate slope and offset value strongly depends on the fit range. We believe that this adds to the error on the slope. To quantify this, we consider the distribution of fit parameters and derive the mean value and standard deviation. This is illustrated in Figure 4.10. It provides an additional uncertainty $\sigma_{b,r} = 0.4209$ on the slope, and $\sigma_{a,r} = 0.2270$ on the offset value (where we have put the subscript 'r' for the error due to the fitting range). We note that the errors are large, but this is expected from the many ranges that are allowed for $0.5 \leq \chi^2 \leq 1.5$ (94 possibilities). However, it makes it difficult to interpret the values of the slopes and compare them to other results. Note also the two peaks that appear in the distribution of the slopes. The peak around $b = -0.8$ Hz is mainly composed of slopes originating from fitting intervals which take a lot of noise into account, for example fitting intervals with $f_{b,low} > 0.5$ Hz and $f_{b,high} > 2.5$ Hz. This is another argument to have a closer look at the upper limit of the fitting range, since this also affects the systematic errors. We decide to not include the systematic errors in our discussion in Chapter 5, since they are too large to interpret. We add them, nevertheless, when stating the results in the next chapter.

The main issue of the χ^2-method is that we are again conservative in our choices of the cut-off frequencies. For each GRB sample, we let $f_{b,low}$ and $f_{b,high}$ vary between 0.01 Hz and 5.00 Hz to be able to include the largest part of the power-law behaviour. This is a good choice for the brightest bursts, which are less noise-dominated and where the noise only sets in at ~ 3 Hz, but this is too wide for e.g. the entire sample of GRBs, as discussed above. One option to overrule this is to define, for each GRB sample individually, the values between which $f_{b,low}$ and $f_{b,high}$ are allowed to vary. These boundaries should be
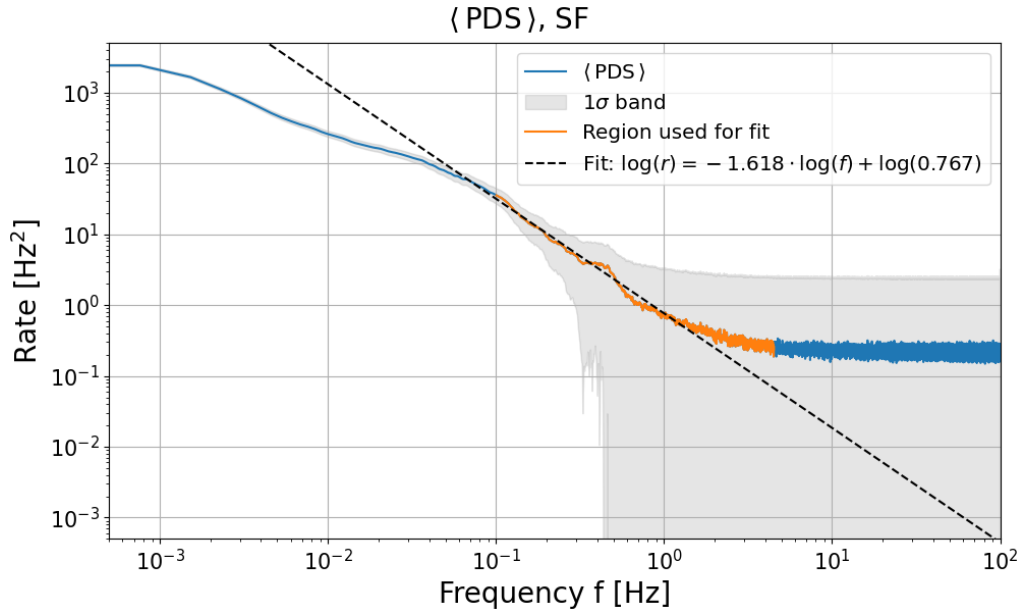
Figure 4.11: The average power-density spectrum of the 156 GRBs in our sample, with its 1σ error band. The orange region illustrates the frequencies between 0.10 Hz and 4.50 Hz, which is the fitting range in which we performed the fit $r = a \cdot f^b$. The best fit is shown as a black dotted line and has fit parameters $b = -1.6181 \pm 0.0367$ Hz and $a = 0.7673 \pm 0.0462$ Hz (see Table 4.1).

defined based on variables inherent to the specific GRB samples. A good possibility is to consider the T90 distribution of all bursts in the sample. One can derive the average value and the 1σ or 2σ interval. Next, the frequencies corresponding to the limits of this interval can be used as fitting range, or as values between which $f_{b,low}$ and $f_{b,high}$ can vary. We believe that, with this method, the systematic errors will significantly decrease and be meaningful. Applying this T90 method would be the next step in this thesis. We started with this analysis, but were not able to finish. Therefore, we did not include this here.

One last feature in the average PDS is the saturation frequency, which appears around $f \sim 0.0008$ Hz. No extra power is gained by looking at the time spectra with time windows larger than $\Delta t \sim 1/0.0008\,\text{Hz} \sim 1250$ s, causing saturation in the spectrum. This is similar to the total zeropadded time array of the bursts, $\Delta t = 1310.72$ s.

Chapter 5

Results

The method to compute the average PDS, described in Chapter 4, is now applied to different samples of GRBs. We start with a short overview of the current developments in the research field in Section 5.1. Subsequently, we describe our sample of GRBs in Section 5.2 to provide some insight in the types of bursts we are investigating. In Section 5.3, we discuss the average PDS of the total sample, after which we divide this sample into different subsamples. We will consider different bursts based on peak rate above background (Section 5.4) and in three different energy bands (Section 5.5). We compare long bursts with short bursts (Section 5.6) and the different episodes of the bursts against each other (Section 5.7). At last, we compare the source frame results with the observer frame results in Section 5.8. The latter are summarised in Appendix B.

5.1 Previous Research

Belobodorov et al. (1998) [58] were the first to notice the power-law behaviour in the average PDS. They investigated long and bright BATSE bursts with peak count rates $C_{peak} > 250$ counts/bin and T90 > 20 s in the 50 - 300 keV energy band. Their sample contained 214 bursts, for which they found a slope $b = -1.67 \pm 0.02$ Hz $\sim -5/3$ Hz in the range 0.02 Hz $< f < 1$ Hz, with a break at 2 Hz. Two years later, they repeated the analysis with a larger sample of bursts. In Belobodorov et al. (2000) [59], they considered 527 BATSE bursts, with T90 > 2 s, $C_{peak} > 100$ counts/bin and a fluence of $\Psi > 32C_{peak}$ in the energy bin 20 keV - 300 keV. They found slopes similar to $-5/3$ Hz, but did not provide uncertainties on their results. Nevertheless, they concluded that the average PDS flattens with increasing energy and steepens for dimmer bursts.

Ryde et al. (2003) [60] reported a slope $b = -1.60 \pm 0.05$ Hz for 10 Integral bursts with T90 > 20 s and a minimal signal significance of 60σ above background. The spectrum broke away from the power-law fit between 1 and 2 Hz. They argued that their bursts belong to the brightest class of bursts in Belobodorov et al. (2000), and explain as such their larger slope. Due to the small sample of bursts, they did not consider their result as significantly deviating.

More recently, Guidorzi et al. (2012) [62] did an extensive investigation of Swift GRB light curves. They considered only long GRBs (T90 > 3 s) and removed bursts with a low SNR by requiring $C_{peak} > 0.1$ counts/s per fully illuminated detector for an equivalent on-axis source. They ended up with 244 GRBs, which they divided in subclasses based on fluence, peak rate, duration and redshift. They studied the average PDS in different energy bands and even corrected in a small sample of bursts for redshift. Owing to their in-depth analyses, they will be our main reference. They find no difference in slope between the source frame and observer frame. They still find that increasing energy corresponds to larger/harder slopes (flatter PDS), and report on slopes consistent with the Kolmogorov turbulence in most cases, although some samples do show slopes as small as ~ -2 Hz. They find no evidence for a cut-off frequency at the high frequency end of the spectrum.

Dichiara et al. (2018) [61] performed the same analysis as Guidorzi et al. (2012) on bursts of BeppoSAX/GRBM and Fermi/GBM, but focussed on light curves in different energy bands. They observed an increase of the slope with increasing energy, confirming previous results, and reported on a clear break between 1 and 2 Hz. The slope of the average PDS broadly agreed with the Kolmogorov slope of $-5/3$ Hz.

5.2 Description of the Sample

Fermi-GBM observed 2705 bursts between 2008 and the end of 2019. However, 21 bursts of this sample do not have TTE data, have gaps in the observations, or have very high background rates [18]. They were removed from the sample in the study of Coppin et al. (2020) [35] and are also excluded from the sample in this thesis. In addition, we limit ourselves to the data of the NaI detectors. Since we focus on the analysis in the source rest frame, we only select GRBs for which the redshift is determined. This reduces the sample to an amount of 156 bursts ($\sim 6.6\%$).

Our sample contains 12 short GRBs ($\sim 7.7\%$) and 144 long GRBs ($\sim 92.3\%$), where we used the conventional selection based on the GRB duration, given by T90 ≤ 2 s for short GRBs and T90 > 2 s for long GRBs. Note that our sample contains more long bursts, since their redshift is more often determined [88]. Nevertheless, even irrespective of redshift, we observe less short than long GRBs. Fermi detected during its first 10 years 17% short bursts and 83% long bursts [19]. It is unclear if this is an observational effect, or has a real, physical origin, due to other effects [89]. The T90 and redshift distributions of our 156 bursts are shown in Figure 5.1. Of the total sample, $\sim 40\%$ are detected at redshifts $z < 1$. Two GRBs are observed at very high distances, $z = 7.5$ (GRB 131202633) and $z = 8.0$ (GRB 090423330).

Recall that we perform the analysis in the source rest frame. Theoretically, we do not expect a large difference between source and observer frame, except for a shift in the location of the frequency range we are interested in (i.e. the frequency range in which we expect power-law signatures). Since time intervals are stretched when photons are
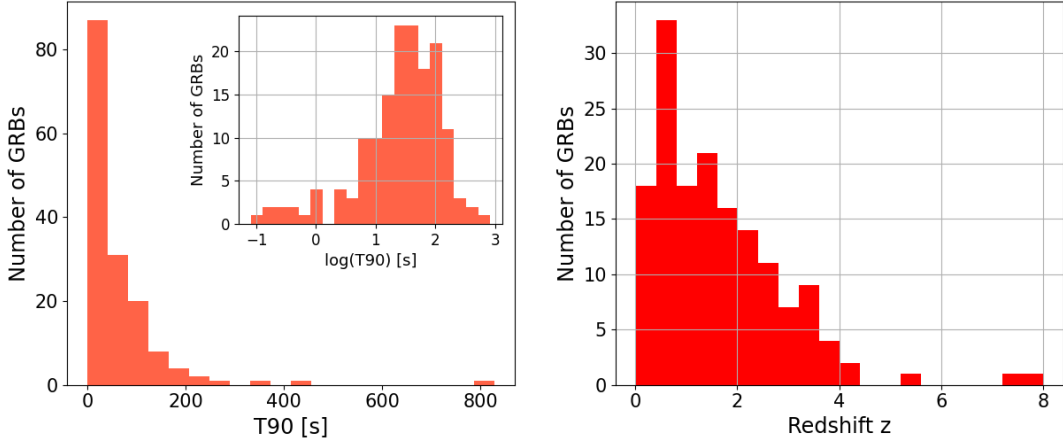
Figure 5.1: T90 distribution (left) and redshift distribution (right) of the total sample of 156 GRBs with known redshift, observed between 2008 and 2019 by Fermi.

redshifted, the interesting region shifts from high frequencies (in the source frame) to lower frequencies (in the observer frame). The effect on the fit parameters is expected to be small. Applying a redshift correction on Eq. 4.10, we find:

$$\log\left(r_e\right) = b \cdot \log\left(f_e\right) + \log\left[a \cdot (1+z)^{(2-b)}\right]. \tag{5.1}$$

Here, r_e and f_e denote the rate and frequency in the source frame. With $\log\left(z+1\right) \sim 0.004 - 0.954$ and $b \sim -1.7$, the largest difference is expected for the offset value, which is not very important for our analysis. We investigate the source and observer frame differences in the following sections.

The total sample of GRBs is discussed in Section 5.3, after which we divide the 156 bursts into different subclasses. We start with a distinction based on peak rate, and proceed with evaluating the sample in different energy bands and for different durations. We end with comparing the different emission periods of the GRB. When investigating source and observer frame, and GRBs in different energy bands, we try to retain the same samples. As such, we purely compare the different characteristics of the sample due to the varying parameters. For subclasses of peak rate and duration, maintaining the same samples is not possible.

5.3   All GRBs

The source frame analysis of the total sample was already briefly discussed in Section 4.3. We considered the total sample of 156 GRBs, without selecting on any parameters. Nevertheless, we notice that some GRBs are highly dominated by noise or even entirely identified as background. Since the detectors were triggered by an excess of photons, there should be a burst present. In these cases, the peak is only visible in certain
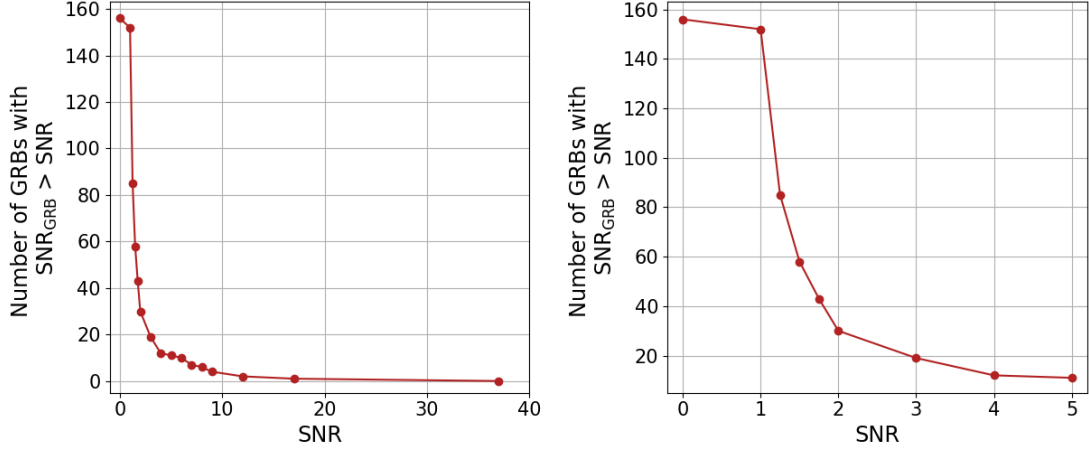
Figure 5.2: *Left*: SNR distribution for the total sample of 156 GRBs, illustrating the number of GRBs that have an SNR larger than the value on the x-axis. *Right*: Zoom-in of the left plot between SNR = 0 and SNR = 5.

energy bands, while it reaches the same photon rate as the background level in the other energy bands, and is thus background dominated. Unfortunately, these bursts include much noise without adding information about the physical features of the gamma-ray emission. As explained in Section 4.3, the noise in the average PDS for the entire sample of 156 GRBs started dominating around 1 Hz and obscured the power-law at higher frequencies. Ideally, we prefer to push this noise towards the highest frequencies. We attempt to exclude noise-dominated GRBs from the sample without losing too many bursts. Therefore, we define the signal-to-noise ratio (SNR), which is described as the average rate $r_{2.5\,s}$ divided by the background level at the peak of the spectrum. We refer to Section 4.2.3 for a visualisation and definition of these variables. We choose to work with the average rate instead of the pure bin counts, to avoid that a fluctuation of one bin defines the SNR of the entire burst, possibly overestimating the true SNR.

In Figure 5.2, the distribution of the GRBs w.r.t. the minimal SNR is shown, with most GRBs enclosed by SNR = 1 and SNR = 2. In order to include as many bursts as possible, while excluding the dimmest ones, we decide to select the bursts with SNR > 1.10. Inspecting the light curves one by one, reveals that most of them have a clear peak, which is not the case for SNR < 1.10. This leaves us with 125 GRBs ($\sim 80\%$). By ensuring that the source and observer frame samples contain the same GRBs, we arrive at a final sample of 124 GRBs.

Fixed interval. At first instance, we perform the fit between 0.05 Hz and 1.00 Hz, as explained in Section 4.3. The result is shown in Figure 5.3 and the fit parameters are listed in the first row of Table 5.1. The fit has $\chi^2/\mathrm{dof} = 2.87$ and a slope of $b = -1.6242 \pm 0.0226$ Hz. We conclude that we have a relatively good fit, with a slope consistent within 2σ with the Kolmogorov turbulence, to which we assign a slope
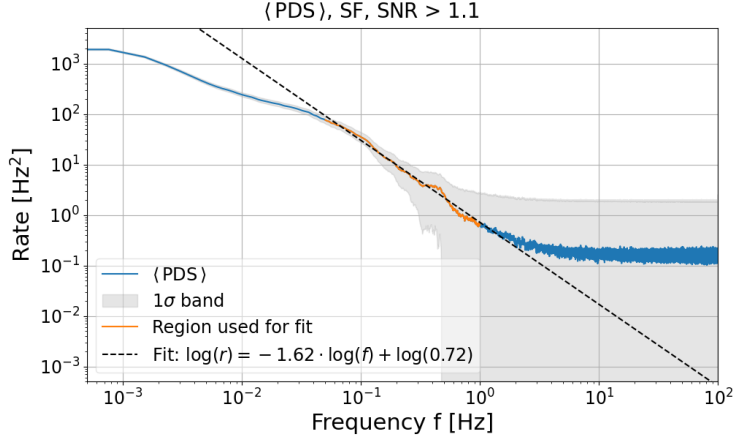
Figure 5.3: Average PDS for 124 GRBs with SNR > 1.10 in the source frame (SF). The dashed line illustrates the best fit between $[f_{b,low}, f_{b,high}] = [0.05$ Hz, 1.00 Hz] (orange region). The corresponding fit parameters are listed in Table 5.1.

of $b \sim -5/3$ Hz. The noise sets in around ~ 2 Hz and is therefore not affecting the power-law fit in a large extent.

Minimal χ^2-method. Subsequently, we search for the optimal fitting range. The χ^2-method will naturally find the best interval, so we are now able to compare the observer and source frame results in a robust way. We indeed expect that the optimal region for the source frame shifts to higher frequencies, compared to the optimal region for the observer frame. We probe the broadest frequency interval for which the fit still has a χ^2/dof value within 0.50 and 1.50. In the redshift corrected case, this interval is given by $[f_{b,low}, f_{b,high}] = [0.10$ Hz, 3.50 Hz]. The best fit has a slope $b = -1.6717 \pm 0.0342 \pm 0.3920$ Hz. The result is shown in Figure 5.4a with the fit parameters listed in Table 5.1. In the observer frame, we find a slope $b = -1.5902 \pm 0.0418 \pm 0.4077$ Hz for $[f_{b,low}, f_{b,high}] = [0.06$ Hz, 3.50 Hz], shown in Figure 5.4b. Only considering the statistical uncertainty, we conclude that this result is consistent with the slope of the source frame within 2σ. The source frame is in perfect agreement with the Kolmogorov slope $b \sim -5/3$ Hz. As predicted, the fitting range of the observer frame is a bit shifted to lower frequencies w.r.t. the fitting range of the source frame. The offset value increases by a factor 2. We note however that in both cases the χ^2-method takes some noise into account to generate the best fits. This 'pulls' the slopes to higher values, resulting in flatter power-laws.

Both slopes have a large error due to the fitting range, which gives us an idea about how much the slope varies for different ranges, while $0.50 \leq \chi^2$/dof ≤ 1.5. Evaluating the fitting range visually, we argue that it includes most of the power-law features. The maximal T90 duration of the source frame sample amounts to 217.90 s, corresponding to a cut-off frequency of 0.005 Hz. However, it feels more natural to state the average T90 duration, since only a small amount of bursts will contribute to those lower frequencies. The average T90 duration is 28.98 Hz, or $f = 0.034$ Hz. In the observer frame, the
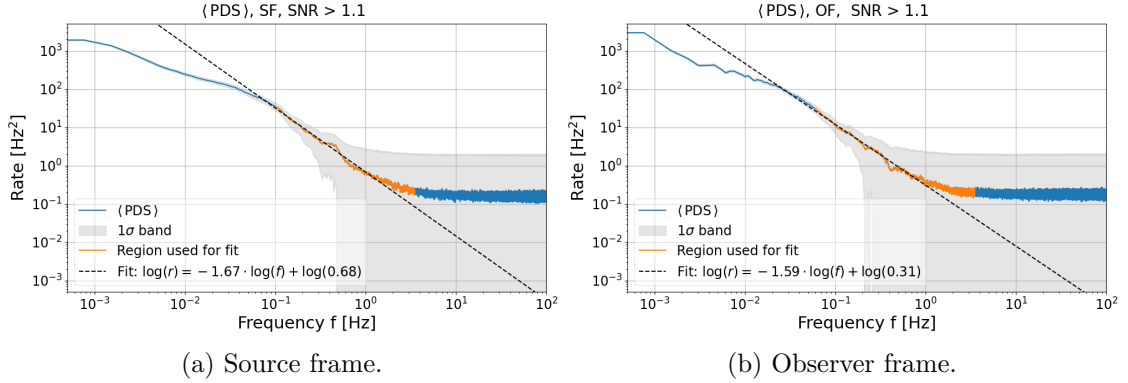
(a) Source frame.

(b) Observer frame.

Figure 5.4: Average PDS for 124 GRBs with SNR > 1.10 in (a) source frame (SF) and (b) observer frame (OF). The dashed line illustrates the best fit between $f_{b,low}$ and $f_{b,high}$ (orange region). See Table 5.1 for the fit parameters.

Table 5.1: Best fit parameters for the power-law fit, $r = a \cdot f^b$, to the average PDS of the sample of 124 GRBs with SNR > 1.10 in source (SF) frame for the fixed interval of $[0.05, 1.00]$ Hz and the optimal interval determined by the χ^2-method. The last row gives the results for the observer frame (OF) with the χ^2-method.

	$a \pm \sigma_a \pm \sigma_{a,r}$ [Hz]	$b + \sigma_b + \sigma_{b,r}$ [Hz]	χ^2/dof	$[f_{b,\,low}, f_{b,\,high}]$
SF	0.7175 ± 0.0361	-1.6242 ± 0.0226	2.87	$[0.05, 1.00]$ Hz
SF	$0.6802 \pm 0.0381 \pm 0.2747$	$-1.6717 \pm 0.0342 \pm 0.3920$	1.47	$[0.10; 3.50]$ Hz
OF	$0.3069 \pm 0.0272 \pm 0.0838$	$-1.5902 \pm 0.0418 \pm 0.4077$	1.45	$[0.06; 3.50]$ Hz

average duration is T90 = 64.19 s, or $f = 0.016$ Hz. The noise naturally puts the limit at the higher frequency end.

Comparing both methods, we conclude that they provide similar results for the slope of the power-law fit. One might argue that the χ^2-method takes quite some noise into account and underestimates the slope, but this is not visible from comparing the numbers solely. In Figure 5.3, it can be seen that the interval $[0.05$ Hz, 1.00 Hz$]$ stretches more to the lower-frequency side and therefore flattens due to the curvature of the average PDS. Both methods are thus not perfect.

5.4 Peak Rate

We know from Figure 5.2 that the majority of the GRBs in our sample has a relatively low peak above background. The number of GRBs falls off rapidly with increasing SNR. In previous studies, the Kolmogorov slope was often recognised in samples of bright GRBs, since they are less noise affected. Multiple studies even observed a power-law behaviour in the PDS of individual bright and long bursts [59, 90, 91]. However, this is generally

Table 5.2: Best fit parameters for the power-law fits, $r = a \cdot f^b$, to the average PDS of all samples, analysed in the source frame in the interval [0.05 Hz, 1.00 Hz]. See text for more information. N is the number of GRBs per sample, and σ_a and σ_b denote the statistical uncertainties on the parameters a and b respectively. The goodness-of-fit is given by χ^2/dof, where dof is the number of degrees of freedom.

Sample	N	$a \pm \sigma_a$ [Hz]	$b \pm \sigma_b$ [Hz]	χ^2/dof
$1.10 < \text{SNR}$	124	0.7175 ± 0.0361	-1.6242 ± 0.0226	2.87
$1.10 < \text{SNR} < 1.25$	29	0.0480 ± 0.0097	-1.0658 ± 0.0992	1.46
$1.25 < \text{SNR} < 2.00$	40	0.1641 ± 0.0128	-1.3835 ± 0.0372	1.12
$2.00 < \text{SNR} < 3.00$	10	0.0564 ± 0.0029	-1.7437 ± 0.0234	8.69
$3.00 < \text{SNR}$	19	0.2200 ± 0.0066	-1.8886 ± 0.0135	7.76
$E < 66\,\text{keV}$	60	0.1472 ± 0.0137	-1.5233 ± 0.0407	1.16
$66\,\text{keV} < E < 366\,\text{keV}$	60	0.2599 ± 0.0152	-1.6763 ± 0.0260	2.27
$366\,\text{keV} < E$	60	0.4636 ± 0.0197	-1.6378 ± 0.0193	3.55
T90 > 2 s	124	0.7102 ± 0.0356	-1.6280 ± 0.0225	2.89
T90 $\leq$ 2 s	11	0.0329 ± 0.0067	-0.2337 ± 0.1544	10.66
Precursor	22	0.4889 ± 0.0622	-0.9046 ± 0.0759	2.07
Prompt emission	20	0.1597 ± 0.0177	-1.7899 ± 0.0508	5.28
Noise	147	0.1632 ± 0.3231	-0.8437 ± 1.1054	0.06

not possible, since the light curves are too noisy. A consistent picture about how the slope varies with peak rate does not yet exist. No significant evolution is expected, since all GRBs are assumed to hold the same physical radiation mechanism. However, Belobodorov et al. (2000) reported on a steepening of the spectrum for dimmer bursts, while Guidorzi et al. (2012) observed no significant differences between dim and bright bursts. Here, we choose to divide the sample into different subsamples based on the SNR and compare the values of the slopes. We distinguish four samples: $1.10 < \text{SNR} < 1.25$ (29 bursts), $1.25 < \text{SNR} < 2.00$ (40 bursts), $2.00 < \text{SNR} < 3.00$ (10 bursts) and $3.00 < \text{SNR}$ (19 bursts). All GRBs belong to one of the categories, so the subsamples differ in their content. The results are shown in Figure 5.5, with on the left the figures corresponding to the fit range [0.05 Hz, 1.00 Hz], and on the right figures associated with the optimal fit based on the χ^2-method. The fit parameters are respectively included in Tables 5.2 and 5.3. For the results of the observer frame, we redirect the reader to Appendix B.

Fixed interval. Fitting between 0.05 Hz and 1.00 Hz for each sample, gives us a decrease of the slope (steepening of the power-law) with increasing SNR. The dimmest bursts are mainly noise dominated in this region and give a slope of $b = -1.0658 \pm 0.0992$ Hz. The second sample is only affected by the noise from $f > 0.6$ Hz on, and gives a power-law with index $b = -1.3835 \pm 0.0372$ Hz. The next sample can be said to be noise-free between 0.05 Hz and 1.00 Hz and gives a slope of $b = -1.7437 \pm 0.0234$ Hz.

Table 5.3: Best fit parameters for the power-law fits, $r = a \cdot f^b$, to the average PDS of all samples, analysed in the source frame, with the fitting interval determined by the χ^2-method. See text for more information. In the second and third column, σ_a and σ_b denote the statistical uncertainties on the parameters a and b respectively, and $\sigma_{a,r}$ and $\sigma_{b,r}$ the error due to the fitting range. The goodness-of-fit is given by χ^2/dof, where dof is the number of degrees of freedom. In the last column, the fitting interval is indicated.

Sample	$a \pm \sigma_a \pm \sigma_{a,r}$ [Hz]	$b + \sigma_b + \sigma_{b,r}$ [Hz]	χ^2/dof	$[f_{b,low}, f_{b,high}]$ Hz
$1.10 <$ SNR	$0.6802 \pm 0.0381 \pm 0.2747$	$-1.6717 \pm 0.0342 \pm 0.3920$	1.47	[0.10; 3.50] Hz
$1.10 <$ SNR < 1.25	$0.0441 \pm 0.0086 \pm 0.0199$	$-1.1203 \pm 0.0880 \pm 0.5607$	1.49	[0.04; 1.00] Hz
$1.25 <$ SNR < 2.00	$0.1764 \pm 0.0118 \pm 0.0420$	$-1.3336 \pm 0.0273 \pm 0.2946$	1.38	[0.03; 1.00] Hz
$2.00 <$ SNR < 3.00	$0.0602 \pm 0.0098 \pm 0.0495$	$-1.5686 \pm 0.1379 \pm 0.7143$	1.13	[0.20; 0.60] Hz
$3.00 <$ SNR	$0.1744 \pm 0.0135 \pm 0.0768$	$-2.2128 \pm 0.0892 \pm 1.1360$	1.22	[0.30; 0.90] Hz
$E < 66$ keV	$0.1658 \pm 0.0130 \pm 0.0177$	$-1.4559 \pm 0.0325 \pm 0.5723$	1.42	[0.04; 1.50] Hz
66 keV $< E < 366$ keV	$0.2951 \pm 0.0230 \pm 0.4519$	$-1.4927 \pm 0.0725 \pm 0.5502$	1.42	[0.20; 2.00] Hz
366 keV $< E$	$0.4708 \pm 0.0257 \pm 0.4941$	$-1.5512 \pm 0.0516 \pm 0.4603$	1.30	[0.20; 2.00] Hz
T90 > 2 s	$0.7367 \pm 0.0437 \pm 0.2727$	$-1.5551 \pm 0.0554 \pm 0.3912$	1.26	[0.20; 3.50] Hz
T90 ≤ 2 s	$0.0095 \pm 0.0045 \pm 0.6486$	$-0.8883 \pm 0.1739 \pm 0.0104$	1.47	[0.02; 0.40] Hz
Precursor	$0.4545 \pm 0.0807 \pm 0.0514$	$-1.0067 \pm 0.1878 \pm 0.1855$	0.95	[0.20; 1.00] Hz
Prompt emission	$0.2200 \pm 0.0379 \pm 0.5916$	$-1.4270 \pm 0.1618 \pm 0.6471$	1.40	[0.20; 1.00] Hz
Noise	$0.2935 \pm 0.1768 \pm 0.1100$	$-0.4404 \pm 0.5117 \pm 1.1607$	1.41	[0.05; 4.50] Hz

This is consistent with the Kolmogorov turbulence within $\sim 3\sigma$. The brightest bursts give a slope of $b = -1.8886 \pm 0.0135$ Hz. They reach smaller slopes than the Kolmogorov turbulence, which is apparent, since that means that there is a process "beyond" the turbulence, in which gamma-rays can originate. The spectrum is far outside the noise region, and the fit may even be flattened by the curvature at the lower-frequency side.

Minimal χ^2-method. The results for the minimal χ^2-method give the same decreasing behaviour of the slope with increasing SNR. For the two dimmest samples, the method arrives at approximately the same fitting interval and thus the same slopes: $b = -1.1203 \pm 0.0880 \pm 0.5607$ Hz for $1.10 < \mathrm{SNR} < 1.25$ and $b = -1.3336 \pm 0.0273 \pm 0.2946$ Hz for $1.25 < \mathrm{SNR} < 2.00$. However, for the brighter samples, the χ^2-method chooses smaller intervals, giving different slopes: $b = -1.5686 \pm 0.1379 \pm 0.7143$ Hz for $2.00 < \mathrm{SNR} < 3.00$ and $b = 2.2128 \pm 0.0892 \pm 1.1360$ Hz for $3.00 < \mathrm{SNR}$. Again, we find for the third sample a slope consistent with the Kolmogorov slope, and for the brightest bursts, a slope that goes beyond that.

Hence, we find a significant steepening of the power-law for brighter bursts, in contrary to what is found by Belobodorov et al. (2000) and Guidorzi et al. (2012). While the slope for the dimmest bursts still can be affected by noise, and even in a lower extent for the sample with $1.25 < \mathrm{SNR} < 2.00$, this cannot be said for the brighter bursts.

We conclude that there might be intermediate bright bursts with slopes around $-5/3$ Hz, but there are also brighter bursts which show steeper power-laws with slopes ~ -2.00 Hz, and weaker bursts which exhibit slopes of ~ -1.30 Hz. The turbulence is not visible for those bursts. Whether the large slopes of the dim bursts are purely due to the noise, is difficult to deduce. A hypothesis for the steep power-laws of the strong bursts, might be that those are bursts that are pointed towards us. These typically appear stronger and can explain the absence of the turbulence features, since one cannot see the structures of the jet when looking straight into the cone. This is similar to looking right into the light of a torch; the observer only sees the bright light. The lamp is solely visible when watching from the side.

Another conclusion could be that there is no Kolmogorov turbulence present, but rather a process that produces a frequency spectrum with f^{-2}, since the power-law seems to steepen towards a slope of ~ -2 Hz. Similar slopes were reported by Guidorzi et al. (2012) for several samples (long bursts, bright and energetic bursts). However, they find many slopes $b < -1.80$ Hz, e.g. even when they analyse their entire sample of GRBs (note that they selected on bright and long bursts from the start). It is difficult to deduce if their small slopes are not the result of a different approach (i.e. fitting a broken power-law instead of a single power-law) or a choice of sample, rather than being of physical origin.

(a) $1.10 < \text{SNR} < 1.25$ (fixed interval).

(b) $1.10 < \text{SNR} < 1.25$ (χ^2-method).

(c) $1.25 < \text{SNR} < 2.00$ (fixed interval).

(d) $1.25 < \text{SNR} < 2.00$ (χ^2-method).

(e) $2.00 < \text{SNR} < 3.00$ (fixed interval).

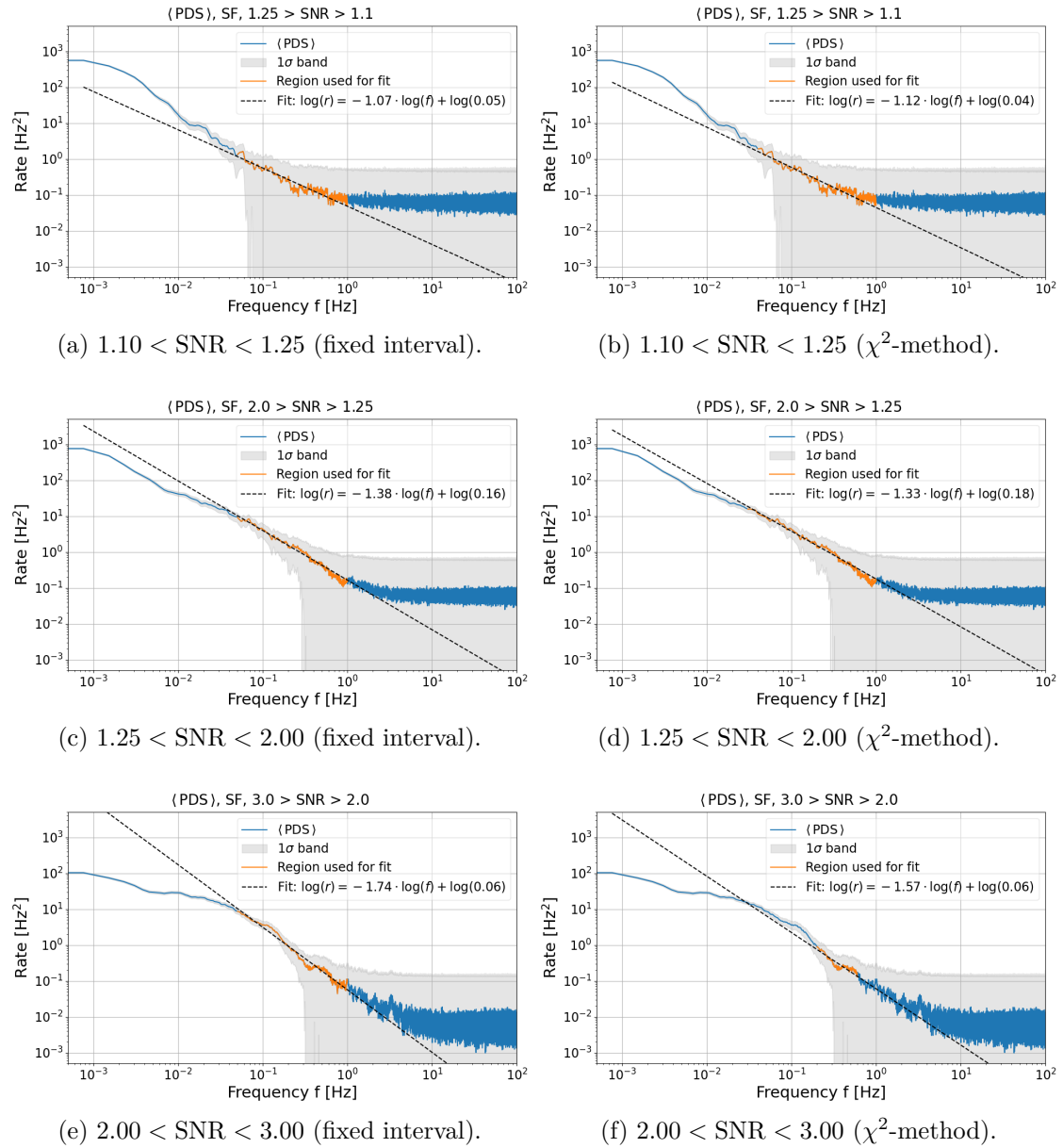(f) $2.00 < \text{SNR} < 3.00$ (χ^2-method).

Figure 5.5: Average PDS for GRBs with different peak rates: (a, b) $1.10 < \text{SNR} < 1.25$ (29 bursts), (c, d) $1.25 < \text{SNR} < 2.00$ (40 bursts), (e, f) $2.00 < \text{SNR} < 3.00$ (10 bursts), (g, h) $3.00 < \text{SNR}$ (19 bursts) for the fixed interval (left) and χ^2-method (right). The orange region illustrate the range for which the fit is computed (between $f_{b,low}$ and $f_{b,high}$). For the best fitting parameters, see Tables 5.2 and 5.3. Figure continues on the next page.

(g) $3.00 < \mathrm{SNR}$ (fixed interval).　　　(h) $3.00 < \mathrm{SNR}$ (χ^2-method).
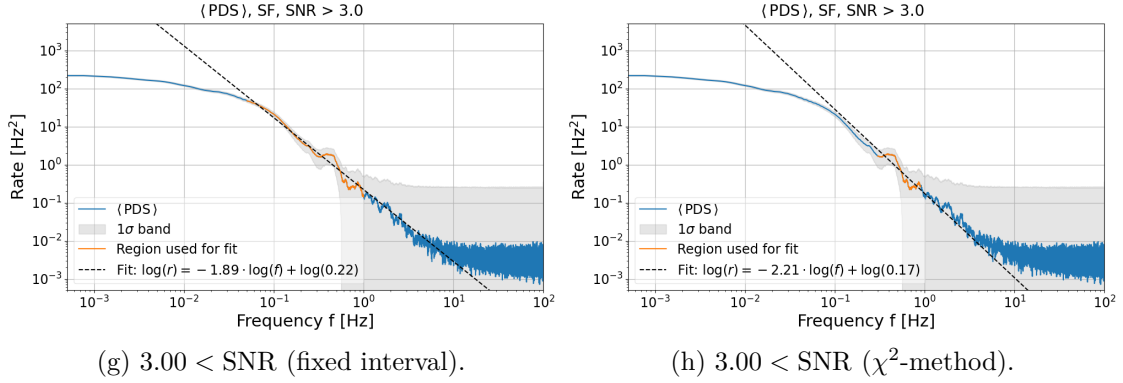
Figure 5.5: Continuation of figure on previous page.

5.5　Energy Bands

Of all properties of the power-law, the evolution of the slope with energy has been investigated the most. It is not easy to intuitively predict certain behaviour. In general, the light curves of GRBs appear narrower in higher energy bands, and broader for lower energy bands [22, 23]. Thus, the outlook of the light curves and their PDS changes accordingly, together with the slopes. Belobodorov et al. (2000), Guidorzi et al. (2012) and Dichiara et al. (2018) noticed all a flatter slope for increasing energy, while they studied the behaviour for different telescopes and different energy bands. Belobodorov et al. (2000) explains this by arguing that the power at lower frequencies decreases for higher energies, since the average duration of the bursts decreases as well (long time durations correspond to lower frequencies). Therefore, the power-law will exhibit a flatter slope.

In this thesis, we distinguish three energy bands in accordance with Guidorzi et al. (2012): $E < 66$ keV, 66 keV $< E < 366$ keV and 366 keV $< E$, where we also required $\mathrm{SNR} > 1.10$. Since we prefer the same bursts in all samples that we compare, and we will do the analysis in the observer frame as well (see Appendix B), the amount of bursts in the three energy bands equals 60 GRBs. The figures of the average spectra can be found in Figure 5.6, while the fit parameters are listed in Tables 5.2 and 5.3.

Fixed interval. For [0.05 Hz, 1.00 Hz], we arrive at the following slopes for the different samples. For the lowest energy band, we find a slope of $b = -1.5233 \pm 0.0407$ Hz. For the middle band, this decreases towards $b = -1.6763 \pm 0.0260$ Hz, after which this again increases for the highest energies and gives $b = -1.6378 \pm 0.0193$ Hz. We thus have an alternating behaviour for increasing energy, which is not trivial and not alike the flattening behaviour of previous studies. The average PDS of the lowest energy band is still somewhat noise affected for $f \gtrsim 0.6$ Hz, which flattens the power-law. This is not a problem for the other energy bands.

(a) $E < 66$ keV (fixed interval).

(b) $E < 66$ keV (χ^2-method).

(c) 66 keV $< E <$ 366 keV (fixed interval).

(d) 66 keV $< E <$ 366 keV (χ^2-method).

(e) $E > 366$ keV (fixed interval).

(f) $E > 366$ keV (χ^2-method).
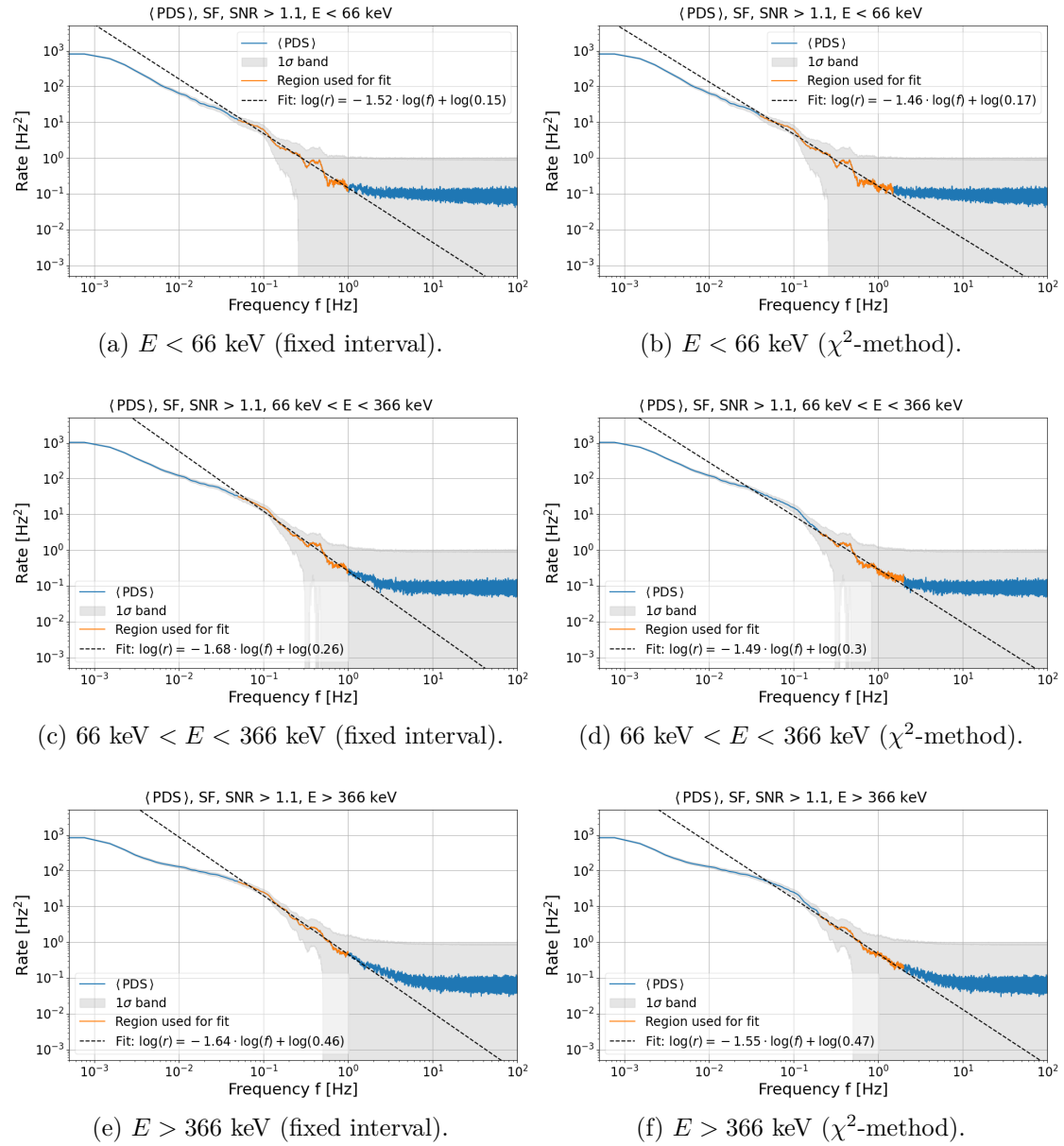
Figure 5.6: Average PDS of 60 GRBs for (a, b) $E < 66$ keV, (c, d) 66 keV $< E <$ 366 keV and (e, f) $E > 366$ keV, with on the left the results for the fixed interval of [0.05 Hz, 1.00 Hz] and on the right the results for the χ^2-method. See Tables 5.2 and 5.3 for the corresponding fitting parameters.

Minimal χ^2-method. For $E < 66$ keV, we find a slope $b = -1.4559 \pm 0.0325 \pm 0.5723$ Hz and for 66 keV $< E <$ 366 keV, $b = -1.4927 \pm 0.0725 \pm 0.5502$ Hz. For the highest energy band, we have $b = -1.5512 \pm 0.0516 \pm 0.4603$ Hz. We thus find a steepening of the power-law towards higher energies, but this is insignificant. This is inconsistent with previous studies.

We summarised all results in Figure 5.7. All previous studies showed an increase of the slope, or equally a flattening of the power-law, with increasing energy. Our results of the source frame tend to have the opposite behaviour. We note that the main difference between us and the previous papers includes the redshift correction. For completeness, we add our results in observer frame as well in Figure 5.7. For more details about these average spectra and the fits, we refer to Appendix B. For the observer frame, we arrive at a slope $b = -1.6834 \pm 0.0384 \pm 0.4601$ Hz for $E < 66$ keV, a slope $b = -1.3195 \pm 0.0841 \pm 0.2780$ Hz for 66 keV $< E <$ 366 keV and $b = -0.8807 \pm 0.0664 \pm 0.4814$ Hz for $E > 366$ keV. The latter result is strongly noise dominated, and as a consequence gives such a large slope. But even when this slope would be in line with the others, we report on a significant flattening of the power-law between the different energy bands, more resembling the behaviour that is seen in the other studies.

It is still interesting that we observe such a large difference between the observer and source frame. With the redshift correction, the time intervals are compressed, resulting in higher frequencies. The energy of the photons is also shifted to higher energies (see Eq. 4.1). That means that photons jump from a lower energy band to a higher energy band. The middle energy band receives photons from the lowest band, and loses photons to the highest band. However, the energy pass band of the Fermi detector only ranges between 8 keV and 1 MeV. That means that photons with an observer frame energy lower than < 8 keV but a source frame energy > 8 keV are not observed. We cannot include them in our source frame analysis of $E < 66$ keV. In the highest energy band, the effect is slightly different. Observed photons increase in energy after correcting for redshift, but still remain in the same band (we only consider three energy bands). In addition, this band receives photons from the middle band that have source frame energy > 366 keV. That means that this band stretches over a much larger energy range than in the observer frame (beyond 1 MeV). And again, there might be (low redshift[1]) photons that were not detected by Fermi in the observer frame, since they had $E > 1$ MeV. But, since the energy band of $E > 366$ keV now extends beyond 1 MeV in the source frame, they should be included in the light curve that we consider in the source frame.

In conclusion, we are never able to reconstruct the source frame time spectra perfectly. There is a loss of photons; photons that are not observed in the observer frame by Fermi, but would be present in the same energy bands at the source. This effect is the largest

---

[1]This applies to low-redshift photons, since they only receive a small extra factor on their energy when correcting for redshift. Photons with a high redshift can have an observer frame energy ~ 1.5 MeV, but increase so much in energy that they still do not fall into the "new" boundaries of the source frame energy band.
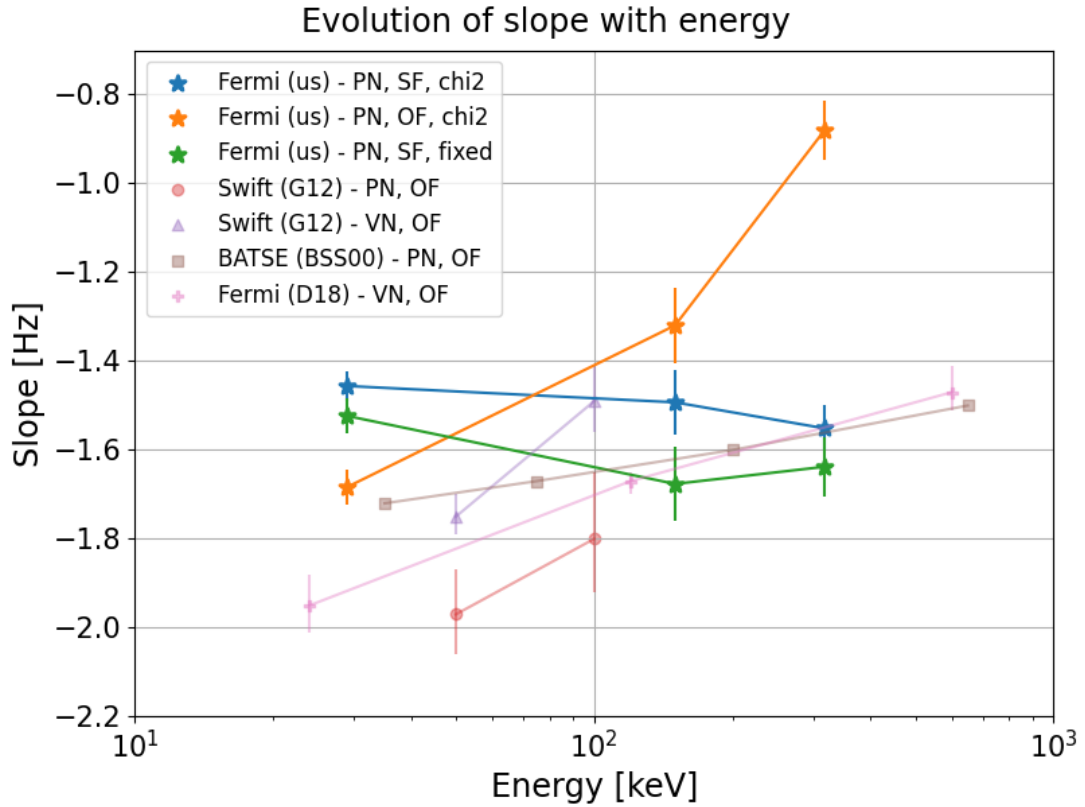
Figure 5.7: The slope of the power-law fit in different energy bands. The orange, blue and green curves state our results, in observer frame (OF) and source frame (SF) for the χ^2-method and in SF for the fixed interval respectively. The circles refer to the peak-normalised (PN) results of Guidorzi et al. (2012), and the triangles to their variance normalised (VN) results. The BATSE results come from Belobodorov et al. (2000) and the Fermi-GBM results are found by Dichiara et al. (2018).

at the outer energy bands, but for high redshifts (and thus for photons receiving large corrections on the energy) this also plays a role for the middle energy band. This is how we explain the deviating results between observer and source frame.
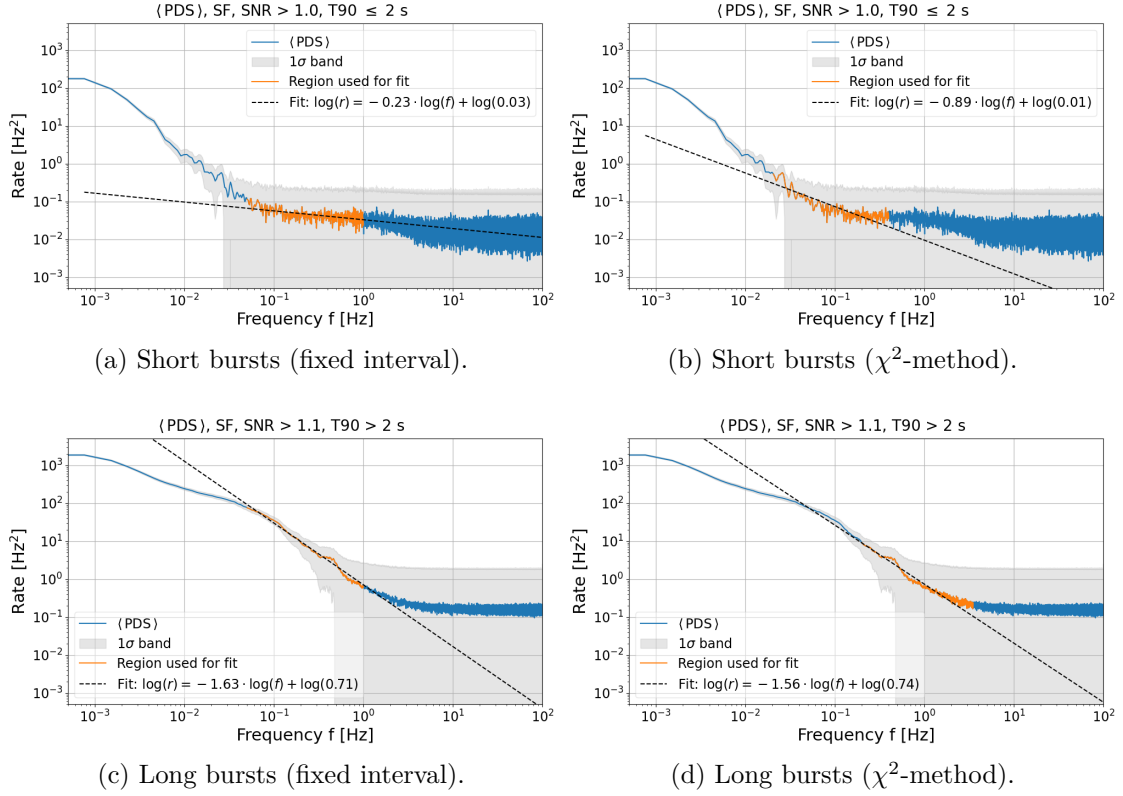
(a) Short bursts (fixed interval).

(b) Short bursts (χ^2-method).

(c) Long bursts (fixed interval).

(d) Long bursts (χ^2-method).

Figure 5.8: Average PDS of (a) 11 short bursts with SNR > 1.00 and T90 ≤ 2 s and (b) 124 long bursts with SNR > 1.10 and T90 > 2 s. See Tables 5.2 and 5.3 for the best fitting parameters.

5.6 Duration

The distinction between long and short bursts happens based on their observed T90 value. It is convenient to define short bursts as GRBs with T90 ≤ 2 s, and long bursts as GRBs with T90 > 2 s. Previous studies only considered long bursts, since they are less noise dominated and more often observed. We see that it is very difficult to find a qualitative sample of short bursts ourselves. Typically, we use the criterium SNR > 1.10, but this is only satisfied for 2 short bursts. Therefore, we will state the result here for SNR > 1.00, which gives 11 bursts in total. For long bursts, we still use SNR > 1.10 and are left with 124 bursts. The average PDS for both samples is shown in Figure 5.8. Their fitting parameters are summarised in Tables 5.2 and 5.3.

Fixed interval. The spectrum of the short bursts is totally noise dominated for $f > 0.05$ Hz. This is clearly reflected in the resulting slope of the power-law fit: $b = -0.2337 \pm 0.1544$ Hz. As can be seen in Figure 5.8a, we are only fitting noise. For the long bursts, the spectrum is not affected by noise in the fitting range, and the fit provides us with a slope $b = -1.6280 \pm 0.0225$ Hz. This is consistent with the Kolmogorov slope within 2σ.

Minimal χ^2-method. Analogous to the fit in the fixed interval, the χ^2-method does not succeed in choosing a region outside the noise for the short bursts. Therefore, our fit is again noise dominated and has a slope $b = -0.8883 \pm 0.1739 \pm 0.6486$ Hz. The long bursts however are again fitted by a power-law consistent with the Kolmogorov slope: $b = -1.5551 \pm 0.0554 \pm 0.3912$ Hz. The fitting region now includes some noise around 2 Hz. This explains the larger slope, compared to the method above.

Both methods give similar results. As could be expected from the fact that only two bursts had SNR > 1.10, the power-law features for short bursts completely disappear in the noise. Therefore, the slope is overestimated and gives no information about the bursts themselves. Only at frequencies $f < 0.1$ Hz, we can recognise some power-law features. To be able to draw a conclusion, we should extend the sample of bright, short bursts in the future, or find a way to remove the noise from the PDS. We tried to cut the light curve and only include the burst itself, but this was not successful. The spectra of the long bursts give satisfying results, which point towards a confirmation of the Kolmogorov turbulence.

5.7 Emission Periods

At last, we have a look at the different emission periods of the light curves of GRBs. The entire burst consists of three periods: the prompt emission, the precursor emission and the afterglow emission. The latter is most apparent in lower energy bands, and difficult to distinguish from the background rate in the gamma-ray emission. Therefore, we only focus on the precursor and the prompt emission, and investigate the noise profile as well. Never before, it was investigated how the different phases of a GRB behave in the frequency spectrum. Thanks to a previous study of the precursor emission of GRBs in Coppin et al. (2020) [35], we have the data to perform this analysis.

In Coppin et al. (2020), they incorporated a Bayesian Block (BB) method to recognise significant increases in the rate of the light curves. As such, it was possible to distinguish between different emission periods. In the entire sample, 24 precursors were identified for 22 GRBs with known redshift. Two GRBs had two precursors. However, one of those bursts could not be used for our analysis, since both precursors fell outside the TTE data (but are present in the CTIME data). One prompt phase had SNR < 1.10 and was therefore excluded. Our final sample consists of 22 precursors and 20 prompt phases. The results are shown in Figure 5.9, with the corresponding fit parameters listed in Tables 5.2 and 5.3.

Precursor. In the range [0.10 Hz, 1.00 Hz], the average precursor PDS exhibits a very beautiful power-law, entirely noise-free. The fixed interval [0.05 Hz, 1.00 Hz] extends a bit more to the lower frequency side, but still grabs the power-law very well. It attributes a slope of $b = -0.9046 \pm 0.0759$ Hz to it. The χ^2-method chooses the range [0.20 Hz, 1.00 Hz], and perfectly probes the associated slope $b = -1.0067 \pm 0.1878 \pm 0.1855$ Hz. There is almost no variation of the spectrum around the straight line. Both slopes are

(a) Precursor (fixed interval).

(b) Precursor (χ^2-method).

(c) Prompt emission (fixed interval).

(d) Prompt emission (χ^2-method).

(e) Noise (fixed interval)
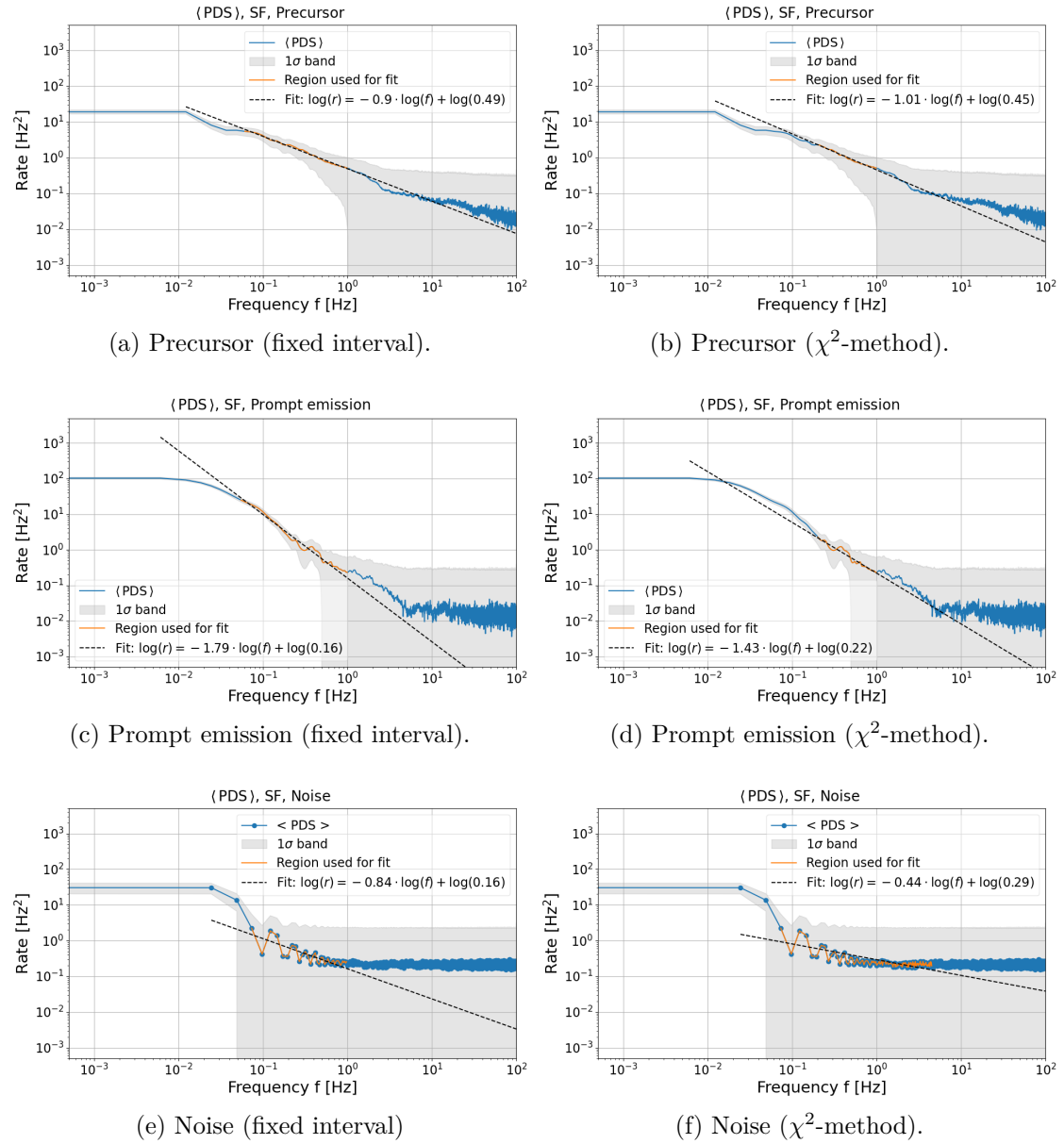
(f) Noise (χ^2-method).

Figure 5.9: Average PDS of (a, b) 22 precursors and (c, d) 20 main bursts, identified by P. Coppin in [35], and (e, f) 148 noise profiles. On the left, the results are displayed of the fit in the fixed interval [0.05 Hz, 1.00 Hz], and on the right, the results of the χ^2-method are included. See Table 5.2 and Table 5.3 for the fit parameters.

inconsistent with the Kolmogorov slope. For the fixed interval, this is with $\sim 10\sigma$, but the χ^2-method has a larger uncertainty and has a deviating result of $> 3\sigma$.

Prompt emission. The average PDS of the prompt emission is in the range [0.05 Hz, 1.00 Hz] fitted by the power-law with slope $b = -1.7899 \pm 0.0508$ Hz. In the range [0.20 Hz, 1.00 Hz], the best fit has an index $b = -1.4270 \pm 0.1618 \pm 0.6471$ Hz. Both slopes are consistent with the Kolmogorov slope within 2σ and with each other.

Noise. The noise profile of the bursts is investigated by taking the last 30 seconds of each burst, requiring that no statistical significant increase of the photon rate occurs. We assume that in these time windows, only noise is present. The average PDS exhibits sinc-behaviour, as is expected for a zeropadded tophat function (see Chapter 3). The power-law fits in both methods the curvature of the sinc function, rather than the features due to the noise. Those are expected at the highest frequencies, since the noise dominates at the smallest time scales. For [0.05 Hz, 1.00 Hz], we find a slope $b = -0.8437 \pm 1.1054$ Hz. The χ^2-method considers [0.05 Hz, 4.50 Hz] and finds $b = -0.4404 \pm 0.5117 \pm 1.1607$ Hz. Nevertheless, the slope is underestimated for both methods. We believe that a realistic fit region would include $f > 3.00$ Hz. We conclude that the noise profiles do not hold any power-law features consistent with $-5/3$ Hz. Note that the average PDS of the short bursts is consistent with the slope of the noise, and was indeed noise dominated.

We conclude that the observations hold the very strong indication that the precursor emission is not produced by the Kolmogorov turbulence, which can still be the case for the prompt emission. An even stronger argument is that the precursor and prompt emission are then produced by a different mechanism, or the same mechanism but in a different environment (e.g. denser). It is not yet established where the precursor finds its origin. Leading models are the transition from optically thick to optically thin phase [92], or a pre-burst of the main burst [93]. The latter would already be excluded by this observation. Further investigations in this power-law behaviour of the precursor and prompt emission might reveal the answer of one of the biggest mysteries of GRBs.

5.8 Source vs. Observer Frame

In Table 5.4, we list the resulting slopes for all source and observer frame samples next to each other. The fits of the observer frame are displayed in Appendix B. We conclude that most observer and source frame results are consistent with each other within one or two standard deviations. This is indeed what is expected, as discussed in Section 5.2. We report on two samples that show deviating results. For $E < 66$ keV, we have a difference of $> 3\sigma$, and the source frame result of the $E > 366$ keV sample differs with more than 5σ interval with the observer frame result. Not surprisingly, these are the different energy band samples. In Section 5.5, we explained that the light spectra of the GRBs change when considering different energy bands, and that we have a loss of photons, falling outside the energy pass band of the detectors. That means that we

Sample	Source frame b [Hz]	Observer frame b [Hz]
$1.10 <$ SNR	$-1.6717 \pm 0.0342 \pm 0.3920$	$-1.5902 \pm 0.0418 \pm 0.4077$
$1.10 <$ SNR < 1.25	$-1.1203 \pm 0.0880 \pm 0.5607$	$-1.1800 \pm 0.1053 \pm 0.5613$
$1.25 <$ SNR < 2.00	$-1.3336 \pm 0.0273 \pm 0.2946$	$-1.2879 \pm 0.0382 \pm 0.4332$
$2.00 <$ SNR < 3.00	$-1.5686 \pm 0.1379 \pm 0.7143$	$-1.6981 \pm 0.0989 \pm 0.2724$
$3.00 <$ SNR	$-2.2128 \pm 0.0892 \pm 1.1360$	$-1.9559 \pm 0.0895 \pm 1.1975$
$E < 66\,\mathrm{keV}$	$-1.4559 \pm 0.0325 \pm 0.5723$	$-1.6834 \pm 0.0384 \pm 0.4601$
$66\,\mathrm{keV} < E < 366\,\mathrm{keV}$	$-1.4927 \pm 0.0725 \pm 0.5502$	$-1.3195 \pm 0.0841 \pm 0.2780$
$366\,\mathrm{keV} < E$	$-1.5512 \pm 0.0516 \pm 0.4603$	$-0.8807 \pm 0.0664 \pm 0.4814$
T90 > 2 s	$-1.5551 \pm 0.0554 \pm 0.3912$	$-1.5998 \pm 0.0418 \pm 0.4124$
T90 < 2 s	$-0.8883 \pm 0.1739 \pm 0.0104$	$-0.8336 \pm 0.1401 \pm 0.5455$
Precursor	$-1.0067 \pm 0.1878 \pm 0.1855$	$-1.1326 \pm 0.1494 \pm 0.3026$
Prompt emission	$-1.4270 \pm 0.1618 \pm 0.6471$	$-1.2657 \pm 0.1749 \pm 0.4231$
Noise	$-0.4404 \pm 0.5117 \pm 1.1607$	$-0.7816 \pm 0.4429 \pm 1.2708$

Table 5.4: Slopes for the observer frame and source frame samples next to each other.

have "incomplete" light curves in the outer bands in the source frame, which is not the case for the observer frame. We see the largest effect for the outer energy bands.

Chapter 6

Conclusion and Outlook

Gamma-ray bursts are the most energetic and luminous transient phenomena in our Universe. We detect approximately 1 GRB, from the 100 up to 1000 events that are estimated to happen every day. Many questions about the processes in GRBs remain unanswered, since they do not last longer than a couple of minutes, happen unexpectedly and do not repeat themselves. The general accepted model is that, from the core-collapse of a massive star or the merger of two compact objects, a black hole forms. It is fed by an accretion disc and pumps out two collimated jets back to back, with material that travels close to the speed of light. We believe that the energetic radiation we receive originates from the jets, where shock formation and particle acceleration processes take place, producing photons with energies spanning the entire EM spectrum, and possibly neutrinos and cosmic rays as well, although they are not (yet) confirmed.

To obtain information about GRBs, we attempt to extract properties from the gamma-ray emission we observe. In this thesis, we aimed at investigating the slope of the average power-density spectrum of a sample of GRBs. Previous studies reported a peculiar slope of $-5/3$ Hz, which is the characteristic slope of the Kolmogorov spectrum. This spectrum describes the energy distribution over "eddies" with different scales in fully turbulent media. Recognising this slope in the light spectra of GRBs, might indicate that a turbulent process is present in the GRB, producing gamma-rays. This turbulence manifests itself in the gamma-rays that we observe, millions of light years away from their birthplace. Our goal was to study this power-law behaviour in different samples of GRBs and search for this Kolmogorov slope.

We considered GRBs detected by Fermi-GBM in the years between 2008 and 2019. We used TTE data, which are single photon counts. We generated the light curves, corrected for redshift, and developed a method to characterise the background in the different time spectra. We normalised them, such that each GRB contributes equally to the average PDS. Next, we calculated the individual power-density spectra with statistical uncertainties. We averaged over the entire sample of GRBs, and arrived at the average PDS.

The next step was to characterise the power-law behaviour. We recognised that the power-law was only apparent in a certain range of frequencies, and should be fitted within this interval. As a first attempt, we chose a fixed fitting range between 0.05 Hz and 1.00 Hz. This region was inspired by previous studies, but did not rely on physical parameters and was difficult to justify. In addition, each sample of GRBs is characterised by a different time variability, and thus the power-law does not appear at the same frequencies. Consequently, we preferred a more robust method to derive the fitting range. We developed a minimal χ^2-method. Here, the broadest interval between 0.01 Hz and 5.00 Hz was selected, while $0.50 < \chi^2/\text{dof} < 1.50$. The boundaries of 0.01 Hz and 5.00 Hz were chosen to include the power-law behaviour maximally for all samples. This method has the advantage that it allows to derive a systematic error on the fit parameters, from the distribution of the slopes and offsets that result from the various ranges with $0.50 < \chi^2/\text{dof} < 1.50$. This makes it possible to account for the choice of fit interval, since the slope strongly depends on the region in which is fitted.

But, this method has its own shortcomings. The upper limit of 5 Hz often allowed to include much noise at $f > 1.00$ Hz, resulting in an overestimation of the slope of the power-law. This was not easy to solve; the frequency at which the noise sets in, varies for different GRB samples. It is not possible to regard one range that works for all. Therefore, we already reflected on another, more consistent method to define the fitting range. One could analyse the GRB duration of the sample, and derive the 1σ or 2σ interval. This interval can be used as a fixed interval or as an interval in which the χ^2-method can find the optimal range. This should be opted in the future.

We divided the total sample of 156 GRBs in different subsamples. To distinguish between bright and weak bursts, we considered four samples with increasing SNR. We investigated bursts in three energy bands, and compared short bursts with long bursts. At last, for the first time, the different emission periods of the GRB - precursor, prompt emission and noise - were discussed. We investigated all source frame samples within the fixed fitting range [0.05 Hz, 1.00 Hz] and within the optimal fitting range, found by the χ^2-method. We extended our analysis by also applying the χ^2-method to the observer frame samples as well. We find that the observer and source frame results do not differ significantly, as expected. Some samples gave deviating results, but this was due to other effects. The differences between the fixed interval and χ^2-method are also not significant, except for the sample SNR > 3.00. Here, the power-law was fitted in different ranges for both methods, resulting in different slopes.

Although both methods give consistent results, the slopes of the fixed fitting range appear to be more consistent with the Kolmogorov slope. For most samples, we find a slope consistent with $b \sim -5/3$ Hz. This is e.g. the case for bright GRBs with $2.00 < \text{SNR} < 3.00$, and GRBs with $E > 66$ keV, long GRBs and the prompt emission. The precursor, the noise and all noise-dominated bursts are not consistent with the Kolmogorov turbulence. We find that the power-law steepens for increasing SNR, even towards slopes of ~ -2 Hz. A significant steepening or flattening with energy is not found, in contrary to previous

studies and our results in the observer frame. We assign this to a loss of photons in the outer energy bands. An important result is that the precursor emission is not consistent with the Kolmogorov turbulence, while this could still be the case for the prompt emission. This indicates that the precursor and prompt emission do not originate from the same process, or do not occur in the same environment, modifying their time variability. This is a very strong statement, recalling that the origin of the precursors is still unknown. Further investigations with more precursors should strengthen this observation. It would as well be interesting to extend the sample of short and bright bursts. Since those time spectra are almost always noise dominated, no results are available for this sample yet in any study. Spectra of short GRBs, however, hold important information about the production of gamma-rays in compact binary mergers. At last, we find that the noise profile does not hold a power-law spectrum with index $-5/3$. That means that the noise cannot be responsible for the observed power-law behaviour, and the latter is thus inherent to the burst itself.

In general, we find a consistency with the Kolmogorov turbulence in most cases, but we are careful with this conclusion. The slope of the average PDS depends strongly on the fitting range. Before drawing any conclusions, one should thoroughly think about the optimal fitting range and where to expect the power-law features. This is what we tried to quantify in this thesis, in more detail than in previous papers, although our analysis is not yet finished. Further, especially the samples of short GRBs and precursors should be extended. Those are often noise dominated, so parallel to that, one should think about a good method to exclude the noise from the PDS. The BB method of Coppin et al. (2020) can play an important role here, since it is able to recognise significant increases in the rate. The emission zones can be cut out of the further noise-dominated light spectrum and be analysed separately.

In addition, we see a broad range of slopes, which exceed or do not reach the slope of $b \sim -5/3$ Hz. We believe that not all features can be assigned to the noise. And why do some samples show steeper power-laws? A hypothesis might be that the strongest GRBs are pointing towards us, which means that we are looking right into the cone of the jet, being unable to observe the turbulence features. To decide whether this is an option, the first step should be to check if this is indeed the case for the GRBs that we consider in this thesis.
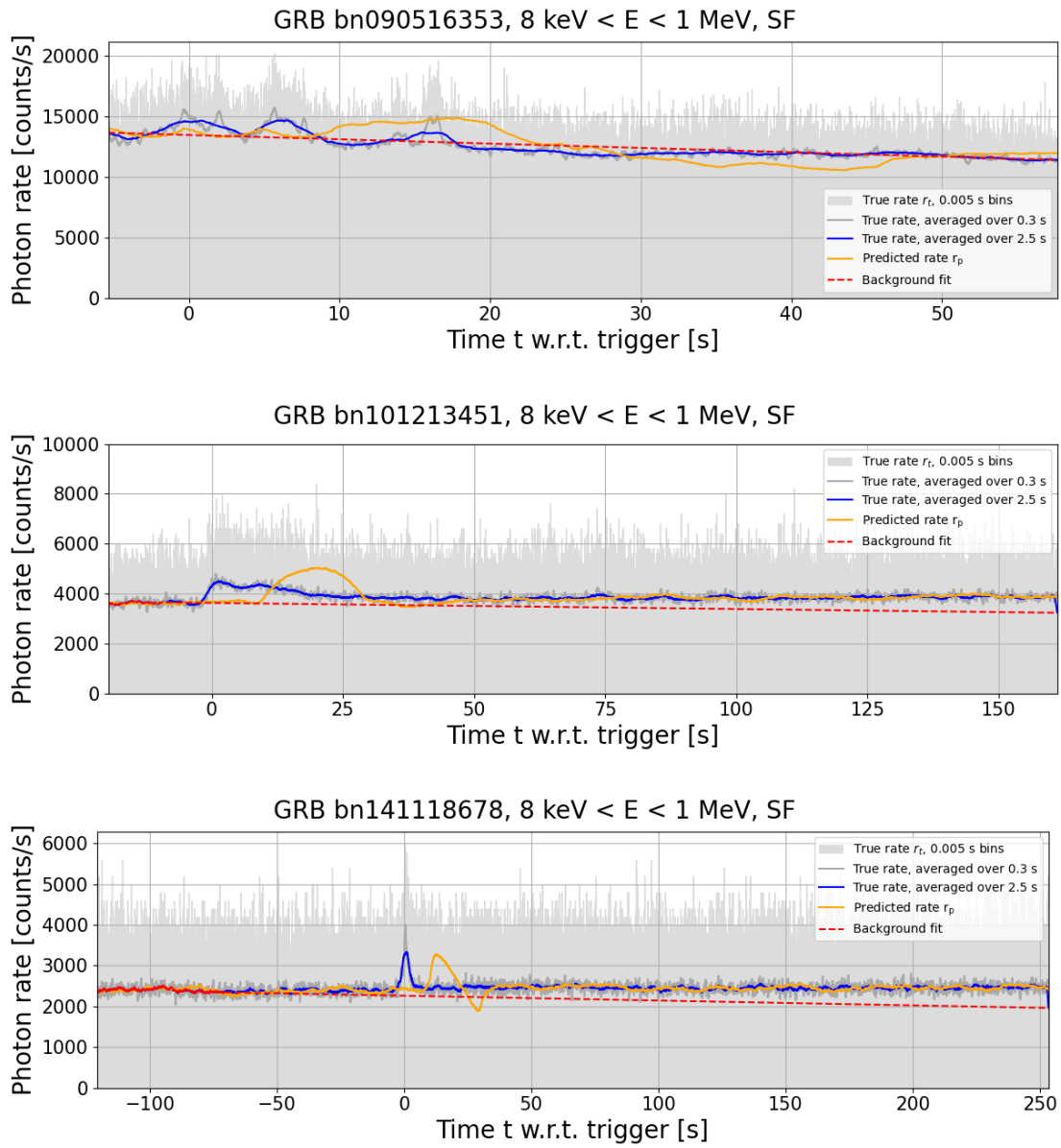
Appendix A

Modified GRBs

For some bursts, the general method for the characterisation of the background (see Section 4.2.3) was not adequate. In those cases, we had to manually modify the background estimation. The final result is determined by eye, but is always inspired by the fit that was proposed by the procedure.

The sample of modified GRBs is in all cases smaller than 10% of the total sample. In Table A.1, all GRBs with a divergent background estimation are listed. Since the outlook of the light curves changes with energy, we made a distinction between the samples of GRBs in different energy bands. The same argument applies to the difference between observer frame (OF) and source frame (SF). To give some examples of bad background characterisations, the OF light curves of the GRBs with energies between 8 keV and 1 MeV are shown in Figure A.1.

Table A.1: All GRBs for which the background fit was manually modified. The first column denotes the reference frame of the GRB, observer frame (OF, not redshift corrected) or source frame (SF, redshift corrected), and the second column provides the energy band in which the background estimation was necessary.

Frame	Energy band	GRB name
SF	8 keV - 1 MeV	GRB 090516353
OF, SF	8 keV - 1 MeV	GRB 101213451
OF	8 keV - 1 MeV	GRB 120907017
OF	8 keV - 1 MeV	GRB 140423356
OF	8 keV - 1 MeV	GRB 140808038
OF, SF	8 keV - 1 MeV	GRB 141118678
OF, SF	8 keV - 1 MeV	GRB 141221338
OF	8 keV - 1 MeV	GRB 150727793
OF	8 keV - 1 MeV	GRB 160804065
OF, SF	8 keV - 1 MeV	GRB 180205184
OF, SF	8 keV - 1 MeV	GRB 180314030
OF	< 66 keV	GRB 101213451
OF, SF	< 66 keV	GRB 120907017
OF	< 66 keV	GRB 140808038
OF, SF	< 66 keV	GRB 141118678
SF	< 66 keV	GRB 141221338
OF	< 66 keV	GRB 150403913
SF	< 66 keV	GRB 150727793
OF	< 66 keV	GRB 160804065
OF	< 66 keV	GRB 161129300
OF, SF	< 66 keV	GRB 180314030
SF	66 - 366 keV	GRB 101213451
OF, SF	66 - 366 keV	GRB 140423356
OF, SF	66 - 366 keV	GRB 141118678
SF	66 - 366 keV	GRB 141221338
OF	66 - 366 keV	GRB 150727793
OF	66 - 366 keV	GRB 160804065
SF	66 - 366 keV	GRB 170405777
OF, SF	66 - 366 keV	GRB 180314030
SF	66 - 366 keV	GRB 190719624
SF	> 366 keV	GRB 090516353
SF	> 366 keV	GRB 131202633
OF	> 366 keV	GRB 170214649
OF, SF	> 366 keV	GRB 180314030

GRB bn090516353, 8 keV < E < 1 MeV, SF

GRB bn101213451, 8 keV < E < 1 MeV, SF
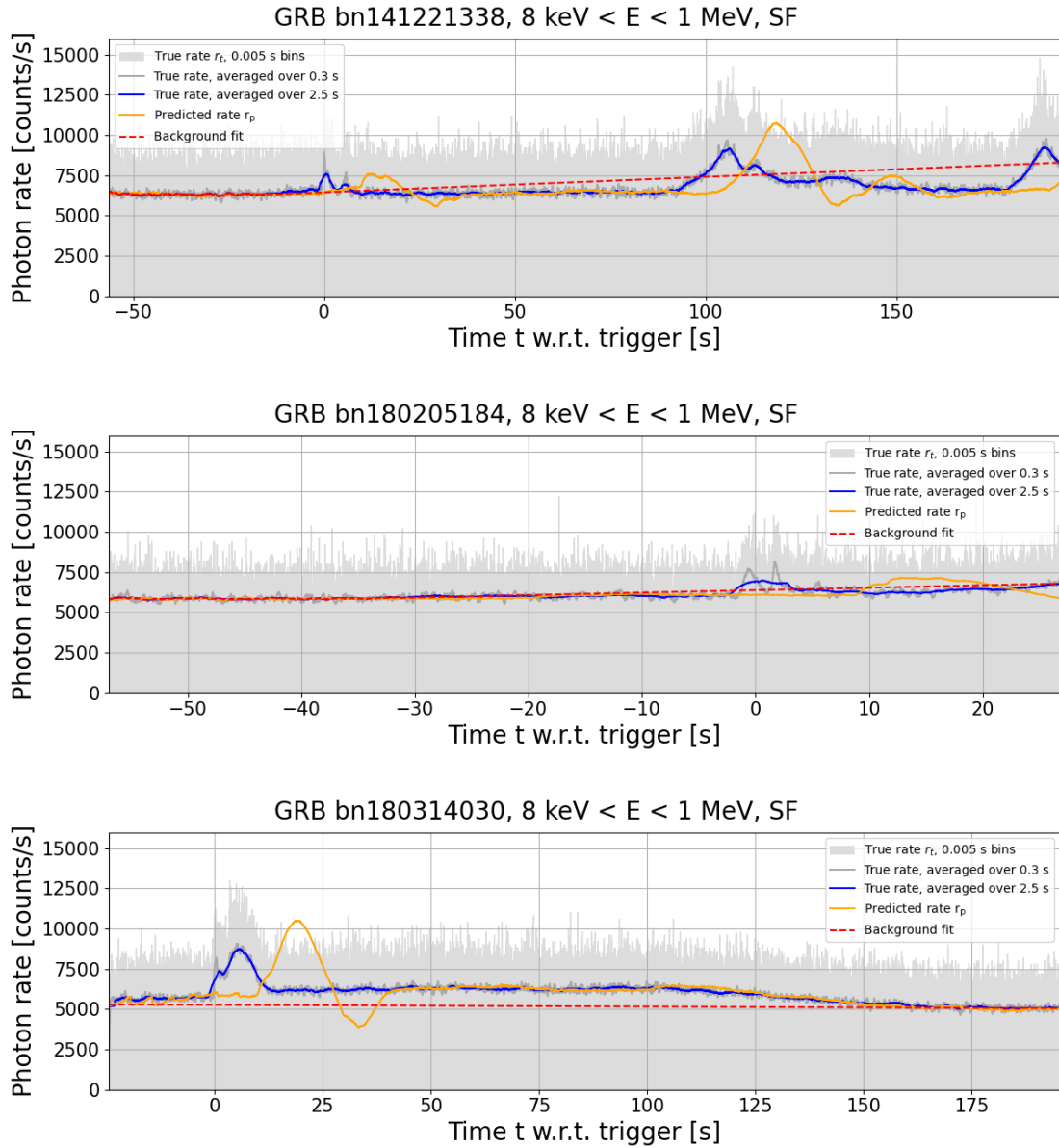

GRB bn141118678, 8 keV < E < 1 MeV, SF

Figure A.1: Figures of GRBs (in source frame and including photons with all energies) with bad background characterisations, performed by the process outlined in Section 4.2.3. The light grey histogram shows the redshift-corrected light curve and the dark grey is the photon rate, averaged over 0.3 s. The blue curve denotes the photon rate $r_{2.5\,s}$, averaged over 2.5 s, and is compared to the predicted rate r_p in yellow to estimate the background rate (red dotted curve).

Appendix B

Observer Frame Results

In Chapter 5, we briefly mentioned the results of the observer frame. As stated there, no large differences are expected between the observer and source frame, since the redshift correction does not affect the index of the power-law fit. To be complete, all figures and results are summarised in this chapter. The fitting parameters are listed in Table B.1, while the fits are grouped in the figures below. The same criteria and samples are used to arrive at those results. Note that we use the χ^2-method to find the optimal fit range, such that we can compare to the source frame results consistently. If we used the [0.05; 1.00] Hz interval to probe the power-law in source and reference frame, we would not probe the same features, since the interesting region shifts from lower frequencies to higher frequencies when redshift correcting.

Table B.1: Best fit parameters for the power-law fits, $r = a \cdot f^b$, to the average PDS of all samples, analysed in the observer frame. See text for more information. In the second and third column, σ_a and σ_b denote the statistical uncertainty on the parameters a and b respectively, and $\sigma_{a,r}$ and $\sigma_{b,r}$ the error due to the fitting range. In the last column, the fitting interval is indicated.

| Sample	$a \pm \sigma_a \pm \sigma_{a,r}$ [Hz]	$b \pm \sigma_b \pm \sigma_{b,r}$ [Hz]	χ^2/dof	$[f_{b,low}, f_{b,high}]$ Hz
$1.10 < \mathrm{SNR}$	$0.3069 \pm 0.0272 \pm 0.0838$	$-1.5902 \pm 0.0418 \pm 0.4077$	1.45	[0.06; 3.50] Hz
$1.10 < \mathrm{SNR} < 1.25$	$0.0130 \pm 0.0046 \pm 0.0236$	$-1.1800 \pm 0.1053 \pm 0.5613$	1.40	[0.01; 0.90] Hz
$1.25 < \mathrm{SNR} < 2.00$	$0.0529 \pm 0.0067 \pm 0.2397$	$-1.2879 \pm 0.0382 \pm 0.4332$	1.12	[0.01; 1.00] Hz
$2.00 < \mathrm{SNR} < 3.00$	$0.0166 \pm 0.0034 \pm 0.0069$	$-1.6981 \pm 0.0989 \pm 0.2724$	1.21	[0.07; 0.40] Hz
$3.00 < \mathrm{SNR}$	$0.0913 \pm 0.0097 \pm 0.0615$	$-1.9559 \pm 0.0895 \pm 1.1975$	1.22	[0.20; 0.80] Hz
$E < 66\,\mathrm{keV}$	$0.1326 \pm 0.0117 \pm 0.1226$	$-1.6834 \pm 0.0384 \pm 0.4601$	1.48	[0.05; 1.50] Hz
$66\,\mathrm{keV} < E < 366\,\mathrm{keV}$	$0.2689 \pm 0.0232 \pm 0.0518$	$-1.3195 \pm 0.0841 \pm 0.2780$	1.39	[0.20; 2.00] Hz
$366\,\mathrm{keV} < E$	$0.1266 \pm 0.0173 \pm 0.6489$	$-0.8807 \pm 0.0664 \pm 0.4814$	1.49	[0.04; 2.00] Hz
T90 > 2 s	$0.2996 \pm 0.0265 \pm 0.0826$	$-1.5998 \pm 0.0418 \pm 0.4124$	1.49	[0.06; 3.50] Hz
T90 $\leq$ 2 s	$0.0095 \pm 0.0041 \pm 0.0087$	$-0.8336 \pm 0.1401 \pm 0.5455$	1.49	[0.01; 0.40] Hz
Precursor	$0.2107 \pm 0.0475 \pm 0.0273$	$-1.1326 \pm 0.1494 \pm 0.3026$	1.49	[0.09; 1.00] Hz
Prompt emission	$0.1232 \pm 0.0232 \pm 0.0427$	$-1.2657 \pm 0.1749 \pm 0.4231$	1.44	[0.20; 0.80] Hz
Noise	$0.2650 \pm 0.1969 \pm 0.1172$	$-0.7816 \pm 0.4429 \pm 1.2708$	1.46	[0.03; 4.50] Hz
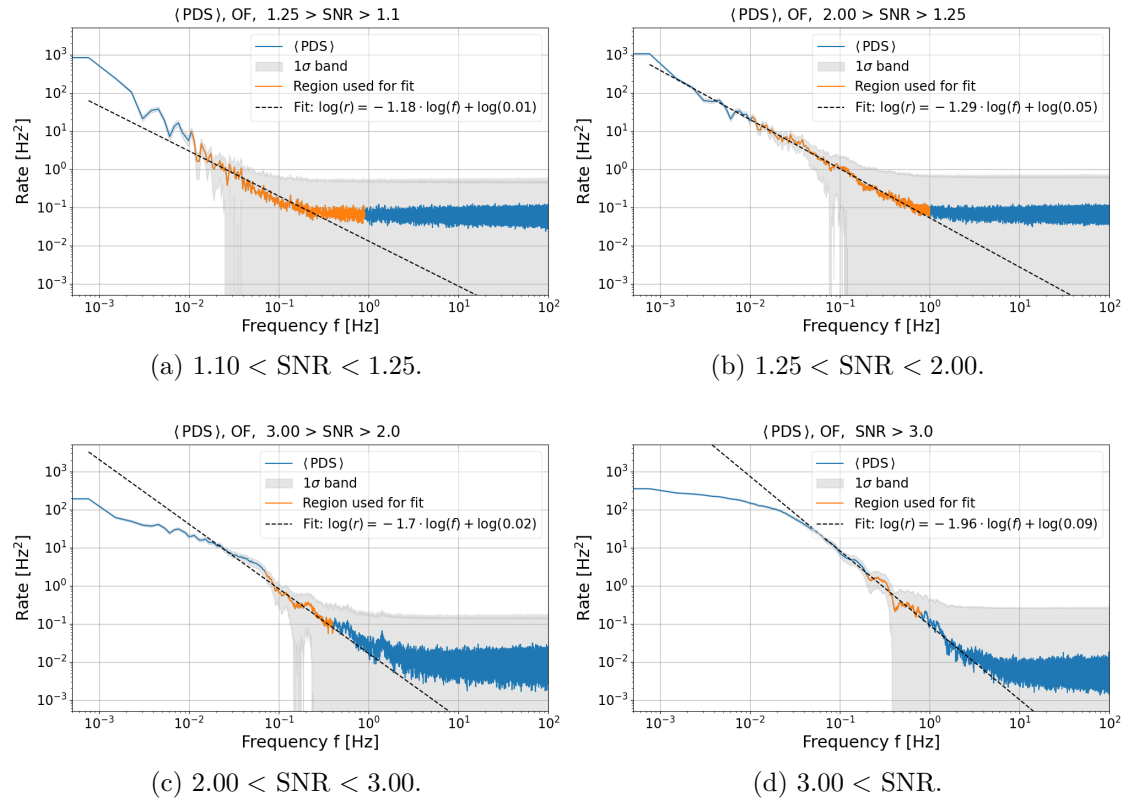
Figure B.1: Average PDS for GRBs with different peak rates: (a) $1.10 < \mathrm{SNR} < 1.25$ (29 bursts), (b) $1.25 < \mathrm{SNR} < 2.00$ (40 bursts), (c) $2.00 < \mathrm{SNR} < 3.00$ (10 bursts), (d) $3.00 < \mathrm{SNR}$ (19 bursts). The orange region illustrate the range for which the fit is computed (between $f_{b,low}$ and $f_{b,high}$). For the best fitting parameters, see Table B.1.
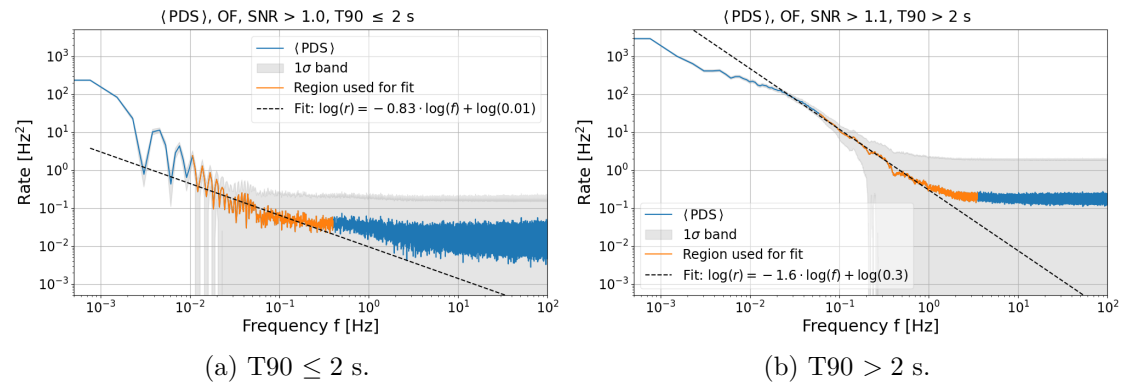

Figure B.2: Average PDS of (a) 11 short bursts with $\mathrm{SNR} > 1.00$ and $\mathrm{T90} \leq 2$ s and (b) 124 long bursts with $\mathrm{SNR} > 1.10$ and $\mathrm{T90} > 2$ s. See Table B.1 for the best fitting parameters.
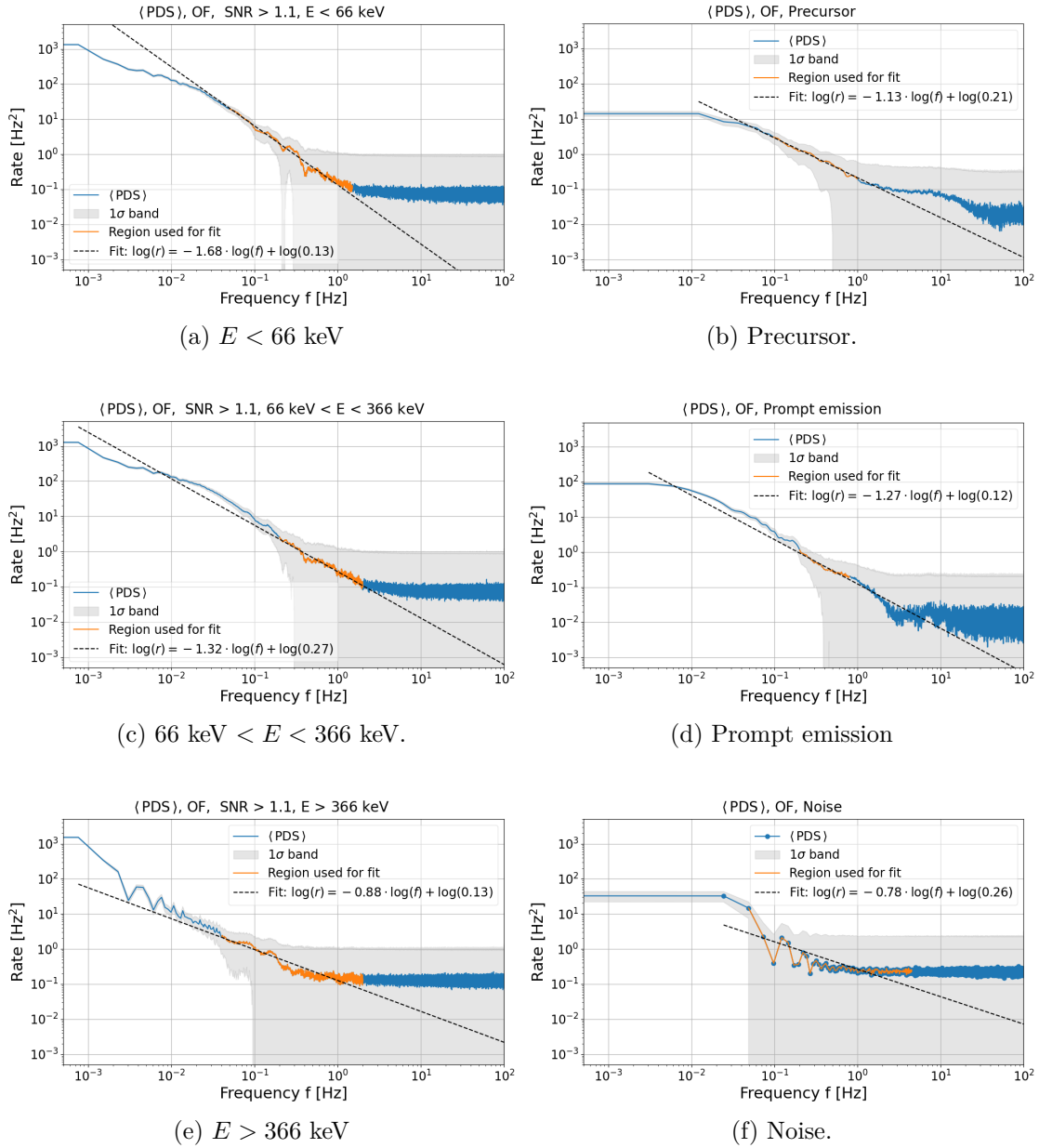
Figure B.3: *Left:* Average PDS of 60 GRBs for (a) $E < 66$ keV, (c) 66 keV $< E < 366$ keV and (e) $E > 366$ keV. *Right:* Average PDS of (b) 22 precursors and (d) 20 main bursts, identified by P. Coppin in [35], and (f) 148 noise profiles. See Table B.1 for the fit parameters.

Bibliography

[1] R. W. Klebesadel et al. Observations of Gamma-Ray Bursts of Cosmic Origin. *The Astrophysical Journal*, 182:L85, June 1973. `doi:10.1086/181225`.

[2] J. R. London. VELA: A space system success story. *Acta Astronautica*, 29(9):723–734, 1993. `doi:https://doi.org/10.1016/0094-5765(93)90091-A`.

[3] T. L. Cline et al. Energy Spectra of Cosmic Gamma-Ray Bursts. *The Astrophysical Journal*, 185:L1, October 1973. `doi:10.1086/181309`.

[4] Wm. A. Wheaton et al. The Direction and Spectral Variability of a Cosmic Gamma-Ray Burst. *The Astrophysical Journal*, 185:L57, October 1973. `doi:10.1086/181320`.

[5] C. Kouveliotou et al. *Gamma-ray Bursts*, volume 51 of *Cambridge Astrophysics*. Cambridge University Press, 2012. `doi:10.1017/CBO9780511980336`.

[6] A. Gomboc. Unveiling the Secrets of Gamma Ray Bursts. *Contemporary Phys.*, 53:339–355, July 2012. `doi:10.1080/00107514.2012.701453`.

[7] L. Weiss. Israel's 1979 Nuclear Test and the US Cover-Up. *Middle East Policy*, 18(4):83–95, 2011.

[8] B. Zhang. *The Physics of Gamma-Ray Bursts*. Cambridge University Press, 2018. `doi:10.1017/9781139226530`.

[9] R. J. Nemiroff. A Century of Gamma Ray Burst Models. *Comments on Astrophysics*, 17:189, January 1994. `doi:10.48550/arXiv.astro-ph/9402012`.

[10] M. Ruderman. Theories of gamma -ray bursts. In P. G. Bergman, E. J. Fenyves, and L. Motz, editors, *Seventh Texas Symposium on Relativistic Astrophysics*, volume 262, pages 164–180, October 1975. `doi:10.1111/j.1749-6632.1975.tb31430.x`.

[11] Y. Kaneko et al. The Complete Spectral Catalog of Bright BATSE Gamma-Ray Bursts. *The Astrophysical Journal Supplement Series*, 166(1):298, September 2006. `doi:10.1086/505911`.

[12] J. van Paradijs et al. Transient optical emission from the error box of the γ-ray burst of 28 February 1997. *Nature*, 386(6626):686–689, April 1997. `doi:10.1038/386686a0`.

[13] M. R. Metzger et al. Spectral constraints on the redshift of the optical counterpart to the γ-ray burst of 8 May 1997. *Nature*, 387(6636):878–880, June 1997. `doi:10.1038/43132`.

[14] K. C. Sahu et al. Observations of GRB 970228 and GRB 970508 and the Neutron Star Merger Model. *The Astrophysical Journal*, 489(2):L127, November 1997. `doi:10.1086/316786`.

[15] E. Berger et al. The afterglow and elliptical host galaxy of the short γ-ray burst GRB 050724. *Nature*, 438(7070):988–990, December 2005. `doi:10.1038/nature04238`.

[16] A. Lien et al. The Third Swift Burst Alert Telescope Gamma-Ray Burst Catalog. *The Astrophysical Journal*, 829(1):7, 2016. `doi:10.3847/0004-637X/829/1/7`.

[17] A. Cucchiara et al. A Photometric Redshift of z ~9.4 for GRB 090429B. *The Astrophysical Journal*, 736(1):7, July 2011. `doi:10.1088/0004-637X/736/1/7`.

[18] P. Coppin. *Investigation of the precursor phase of gamma-ray bursts through gamma-ray and high-energy neutrino observations*. PhD thesis, Vrije Universiteit Brussel, 2022.

[19] A. von Kienlin et al. The Fourth Fermi-GBM Gamma-Ray Burst Catalog: A Decade of Data. *The Astrophysical Journal*, 893:46, 2020. `doi:10.3847/1538-4357/ab7a18`.

[20] F. Ryde et al. IDENTIFICATION AND PROPERTIES OF THE PHOTO-SPHERIC EMISSION IN GRB090902B. *The Astrophysical Journal Letters*, 709(2):L172, January 2010. `doi:10.1088/2041-8205/709/2/L172`.

[21] National Aeronautics and Space Administration. About the Fermi Gamma-ray Space Telescope. [Accessed: May, 26, 2023]. URL: `https://www.nasa.gov/content/fermi/overview`.

[22] A. A. Abdo et al. Fermi Observations of High-Energy Gamma-Ray Emission from GRB 080916C. *Science*, 323(5922):1688, March 2009. `doi:10.1126/science.1169101`.

[23] J. P. Norris et al. Long-Lag, Wide-Pulse Gamma-Ray Bursts. *The Astrophysical Journal*, 627(1):324–345, July 2005. `doi:10.1086/430294`.

[24] C. Kouveliotou et al. Identification of Two Classes of Gamma-Ray Bursts. *The Astrophysical Journal*, 413:L101, August 1993. `doi:10.1086/186969`.

[25] J. J. Brainerd. Gamma-ray bursts in the galactic halo. *Nature*, 355(6360):522–524, February 1992. `doi:10.1038/355522a0`.

[26] W. S. Paciesas et al. The Fourth BATSE Gamma-Ray Burst Catalog (Revised). *The Astrophysical Journal Supplement Series*, 122(2):465–495, June 1999. `doi: 10.1086/313224`.

[27] G. J. Fishman and C. A. Meegan. Gamma-Ray Bursts. *Annual Review of Astronomy and Astrophysics*, 33(1):415–458, January 1995. `doi:10.1146/annurev.aa. 33.090195.002215`.

[28] T. Piran. The physics of gamma-ray bursts. *Reviews of Modern Physics*, 76:1143–1210, October 2004. `doi:10.1103/RevModPhys.76.1143`.

[29] G. Vedrenne and J.-L. Atteia. *Gamma-ray bursts: The brightest explosions in the universe.* Springer Science & Business Media, 2009.

[30] D. Band et al. BATSE Observations of Gamma-Ray Burst Spectra. I. Spectral Diversity. *The Astrophysical Journal*, 413:281, August 1993. `doi:10.1086/172995`.

[31] R. D. Preece et al. The BATSE Gamma-Ray Burst Spectral Catalog. I. High Time Resolution Spectroscopy of Bright Bursts Using High Energy Resolution Data. *The Astrophysical Journal Supplement Series*, 126(1):19, January 2000. `doi:10.1086/ 313289`.

[32] M. Planck. Ueber das Gesetz der Energieverteilung im Normalspectrum. *Annalen der Physik*, 309(3):553–563, 1901. `doi:https://doi.org/10.1002/andp. 19013090310`.

[33] M. Ajello et al. A Decade of Gamma-Ray Bursts Observed by Fermi-LAT: The Second GRB Catalog. *The Astrophysical Journal*, 878(1):52, June 2019. `doi: 10.3847/1538-4357/ab1d4e`.

[34] P. Kumar and B. Zhang. The physics of gamma-ray bursts & relativistic jets. *Physics Reports*, 561:1–109, 2015. The physics of gamma-ray bursts & relativistic jets. `doi:https://doi.org/10.1016/j.physrep.2014.09.008`.

[35] P. Coppin et al. Identification of gamma-ray burst precursors in Fermi-GBM bursts. *Physical Review D*, 102:103014, November 2020. `doi:10.1103/PhysRevD.102. 103014`.

[36] H. Gao et al. Compton scattering of self-absorbed synchrotron emission. *Monthly Notices of the Royal Astronomical Society*, 435(3):2520–2531, September 2013. `doi: 10.1093/mnras/stt1461`.

[37] E. Waxman and J. N. Bahcall. Neutrino Afterglow from Gamma-Ray Bursts: ~10^{18} EV. *The Astrophysical Journal*, 541(2):707–711, October 2000. `doi:10.1086/ 309462`.

[38] K. Murase. High energy neutrino early afterglows from gamma-ray bursts revisited. *Physical Review D*, 76(12):123001, December 2007. `doi:10.1103/PhysRevD.76. 123001`.

[39] N. Gehrels et al. The brightest explosions in the universe. *Scientific American*, 287N6:52–59, 2002.

[40] M. Ravasio. *New insights into the physics of Gamma-Ray Burst prompt emission*. PhD thesis, Milan Bicocca U., 2022.

[41] M. Lyutikov and R. D. Blandford. Gamma ray bursts as electromagnetic outflows. *arXiv e-prints*, pages astro–ph/0312347, December 2003. `doi:10.48550/arXiv.astro-ph/0312347`.

[42] X.-G. Wang et al. How bad or Good are the External Forward Shock Afterglow Models of Gamma-ray Bursts? *The Astrophysical Journal Supplement Series*, 219(1):9, 2015. `doi:10.1088/0067-0049/219/1/9`.

[43] E. Nakar. Short-hard gamma-ray bursts. *Physics Reports*, 442(1-6):166–236, April 2007. `doi:10.1016/j.physrep.2007.02.005`.

[44] A. Levan et al. Gamma-Ray Burst Progenitors. *Space Science Reviews*, 202(1-4):33–78, November 2016. `doi:10.1007/s11214-016-0312-x`.

[45] T. J. Galama et al. An unusual supernova in the error box of the γ-ray burst of 25 April 1998. *Nature*, 395(6703):670–672, October 1998. `doi:10.1038/27150`.

[46] K. Z. Stanek et al. Spectroscopic Discovery of the Supernova 2003dh Associated with GRB 030329. *The Astrophysical Journal*, 591(1):L17–L20, July 2003. `doi:10.1086/376976`.

[47] R. A. Hulse and J. H. Taylor. Discovery of a pulsar in a binary system. *The Astrophysical Journal*, 195:L51–L53, January 1975. `doi:10.1086/181708`.

[48] P. Mészáros. Gamma-ray bursts. *Reports on Progress in Physics*, 69(8):2259, July 2006. `doi:10.1088/0034-4885/69/8/R01`.

[49] B. P. Abbott et al. Gravitational Waves and Gamma-Rays from a Binary Neutron Star Merger: GW 170817 and GRB 170817A. *The Astrophysical Journal Letters*, 848(2):L13, October 2017. `doi:10.3847/2041-8213/aa920c`.

[50] B. P. Abbott et al. GW170817: Observation of Gravitational Waves from a Binary Neutron Star Inspiral. *Physical Review Letters*, 119:161101, October 2017. `doi:10.1103/PhysRevLett.119.161101`.

[51] V. Savchenko et al. INTEGRAL Detection of the First Prompt Gamma-Ray Signal Coincident with the Gravitational-wave Event GW170817. *The Astrophysical Journal Letters*, 848(2):L15, 2017. `doi:10.3847/2041-8213/aa8f94`.

[52] A. Goldstein et al. An Ordinary Short Gamma-Ray Burst with Extraordinary Implications: Fermi-GBM Detection of GRB 170817A. *The Astrophysical Journal Letters*, 848(2):L14, October 2017. `doi:10.3847/2041-8213/aa8f41`.

[53] V. Savchenko et al. INTEGRAL Observations of GW170104. *The Astrophysical Journal Letters*, 846(2):L23, September 2017. `doi:10.3847/2041-8213/aa87ae`.

[54] D. A. Coulter et al. Swope Supernova Survey 2017a (SSS17a), the optical counterpart to a gravitational wave source. *Science*, 358(6370):1556–1558, December 2017. `doi:10.1126/science.aap9811`.

[55] B. P. Abbott et al. Multi-messenger Observations of a Binary Neutron Star Merger*. *The Astrophysical Journal Letters*, 848(2):L12, October 2017. `doi:10.3847/2041-8213/aa91c9`.

[56] N. R. Tanvir et al. The Emergence of a Lanthanide-rich Kilonova Following the Merger of Two Neutron Stars. *The Astrophysical Journal Letters*, 848(2):L27, October 2017. `doi:10.3847/2041-8213/aa90b6`.

[57] I. Arcavi et al. Optical emission from a kilonova following a gravitational-wave-detected neutron-star merger. *Nature*, 551(7678):64–66, November 2017. `doi:10.1038/nature24291`.

[58] A. M. Beloborodov et al. Self-Similar Temporal Behavior of Gamma-Ray Bursts. *The Astrophysical Journal*, 508(1):L25–L27, November 1998. `doi:10.1086/311710`.

[59] A. M. Beloborodov. Power density spectra of gamma-ray bursts. In *AIP Conference Proceedings*. AIP, 2000. `doi:10.1063/1.1361535`.

[60] F. Ryde et al. Gamma-ray bursts observed by the INTEGRAL-SPI anticoincidence shield: A study of individual pulses and temporal variability. *Astronomy & Astrophysics*, 411:L331–L342, November 2003. `doi:10.1051/0004-6361:20031440`.

[61] S. Dichiara et al. Average power density spectrum of long GRBs detected with BeppoSAX/GRBM and with Fermi/GBM. *Monthly Notices of the Royal Astronomical Society*, 431(4):3608–3617, April 2013. `doi:10.1093/mnras/stt445`.

[62] C. Guidorzi et al. Average power density spectrum of Swift long gamma-ray bursts in the observer and in the source-rest frames. *Monthly Notices of the Royal Astronomical Society*, 422(2):1785–1803, April 2012. `doi:10.1111/j.1365-2966.2012.20758.x`.

[63] M. E. J. Newman. Power laws, Pareto distributions and Zipf's law. *Contemporary Physics*, 46(5):323–351, September 2005. `doi:10.1080/00107510500052444`.

[64] F. T. M. Nieuwstadt et al. *Turbulence: Introduction to Theory and Applications of Turbulent Flows*. Springer Science+Business Media, 2016. `doi:10.1007/978-3-319-31599-7`.

[65] L. D. Landau and E. M. Lifshitz. *Fluid Mechanics: Landau and Lifshitz: Course of Theoretical Physics, Volume 6*, volume 6. Elsevier, 2013.

[66] S. B. Pope. *Turbulent Flows*. Cambridge University Press, 2000. `doi:10.1017/ CBO9780511840531`.

[67] J. B. J. Fourier. *Théorie Analytique de la Chaleur*. Cambridge Library Collection - Mathematics. Cambridge University Press, 2009. `doi:10.1017/ CBO9780511693229`.

[68] J. W. Gibbs. Fourier's series. *Nature*, 59(1522):200–200, December 1898. `doi: https://doi.org/10.1038/059200b0`.

[69] H. Wilbraham. On a certain periodic function. *The Cambridge and Dublin Mathematical Journal*, 3:198–201, 1848.

[70] S. W Smith et al. *The scientist and engineer's guide to digital signal processing*. California Technical Pub. San Diego, 1997.

[71] J. M. Blackledget. *Digital Signal Processing: Mathematical and Computational Methods, Software Development and Applications*. Woodhead Publishing, 2006.

[72] P. Gregory. *Bayesian Logical Data Analysis for the Physical Sciences: A Comparative Approach with Mathematica® Support*. Cambridge University Press, 2005. `doi:10.1017/CBO9780511791277`.

[73] NobelPrize.org. Enrico Fermi – Biographical. [Accessed: April, 17, 2023]. URL: `https://www.nobelprize.org/prizes/physics/1938/fermi/biographical/`.

[74] C. Meegan et al. The Fermi Gamma-ray Burst Monitor. *The Astrophysical Journal*, 702(1):791–804, September 2009. `doi:10.1088/0004-637X/702/1/791`.

[75] W. B. Atwood et al. The Large Area Telescope on the Fermi Gamma-Ray Space Telescope Mission. *The Astrophysical Journal*, 697(2):1071–1102, June 2009. `doi: 10.1088/0004-637X/697/2/1071`.

[76] P. F. Michelson et al. Fermi Gamma-ray Space Telescope: high-energy results from the first year. *Reports on Progress in Physics*, 73(7):074901, July 2010. `doi: 10.1088/0034-4885/73/7/074901`.

[77] B. Biltzinger et al. A physical background model for the Fermi Gamma-ray Burst Monitor. *Astronomy & Astrophysics*, 640:A8, August 2020. `doi:10.1051/ 0004-6361/201937347`.

[78] D. Szécsi et al. Direction dependent background fitting for the Fermi GBM data. *Astronomy & Astrophysics*, 557:A8, September 2013. `doi:10.1051/0004-6361/ 201321068`.

[79] O. J. Roberts et al. The First Fermi-GBM Terrestrial Gamma Ray Flash Catalog. *Journal of Geophysical Research: Space Physics*, 123(5):4381–4401, 2018. `doi: https://doi.org/10.1029/2017JA024837`.

[80] W. Li and M. K. Hudson. Earth's Van Allen Radiation Belts: From Discovery to the Van Allen Probes Era. *Journal of Geophysical Research: Space Physics*, 124(11):8319–8351, 2019. `doi:https://doi.org/10.1029/2018JA025940`.

[81] M. Ackermann et al. Measurement of the high-energy gamma-ray emission from the Moon with the Fermi Large Area Telescope. *Physical Review D*, 93:082001, April 2016. `doi:10.1103/PhysRevD.93.082001`.

[82] M. Ajello et al. First Fermi-LAT Solar Flare Catalog. *The Astrophysical Journal Supplement Series*, 252(2):13, February 2021. `doi:10.3847/1538-4365/abd32e`.

[83] M. Ackermann et al. Fermi-LAT Observations of the Diffuse γ-Ray Emission: Implications for Cosmic Rays and the Interstellar Medium. *The Astrophysical Journal*, 750(1):3, May 2012. `doi:10.1088/0004-637X/750/1/3`.

[84] K. Hurley et al. An exceptionally bright flare from SGR 1806–20 and the origins of short-duration γ-ray bursts. *Nature*, 434(7037):1098–1103, 2005. `doi:10.1038/nature03519`.

[85] J. D. Scargle. Studies in Astronomical Time Series Analysis. V. Bayesian Blocks, a New Method to Analyze Structure in Photon Counting Data. *The Astrophysical Journal*, 504(1):405–418, September 1998. `doi:10.1086/306064`.

[86] D. A. Leahy et al. On searches for pulsed emission with application to four globular cluster X-ray sources : NGC 1851, 6441, 6624 and 6712. *The Astrophysical Journal*, 266:160–170, March 1983. `doi:10.1086/160766`.

[87] C. Guidorzi. Power-density spectrum of non-stationary short-lived light curves. *Monthly Notices of the Royal Astronomical Society*, 415(4):3561–3570, August 2011. `doi:10.1111/j.1365-2966.2011.18969.x`.

[88] S. Poolakkil et al. The Fermi-GBM Gamma-Ray Burst Spectral Catalog: 10 yr of Data. *The Astrophysical Journal*, 913(1):60, May 2021. `doi:10.3847/1538-4357/abf24d`.

[89] D. Guetta and T. Piran. The luminosity and redshift distributions of short-duration GRBs. *Astronomy & Astrophysics*, 435(2):421–426, May 2005. `doi:10.1051/0004-6361:20041702`.

[90] T. W. Giblin et al. Power spectra of BATSE GRB time profiles. In *Gamma-Ray Bursts, 4th Hunstville Symposium*, volume 428 of *American Institute of Physics Conference Series*, pages 241–245, May 1998. `doi:10.1063/1.55329`.

[91] B. M. Belli. Shot Noise in Gamma-Ray Bursts. *The Astrophysical Journal*, 393:266, July 1992. `doi:10.1086/171503`.

[92] P. Mészáros et al. X-Ray-rich Gamma-Ray Bursts, Photospheres, and Variability. *The Astrophysical Journal*, 578(2):812–817, October 2002. `doi:10.1086/342611`.

[93] Y.-D. Hu et al. Internal Energy Dissipation of Gamma-Ray Bursts Observed with Swift: Precursors, Prompt Gamma-Rays, Extended Emission, and Late X-Ray Flares. *The Astrophysical Journal*, 789(2):145, July 2014. `doi:10.1088/0004-637X/789/2/145`.